CHAPTER 15

Linear-Scaling Quantum Mechanical Methods for Nanoscopic Structures

ChiYung Yam, Xiao Zheng, GuanHua Chen
Department of Chemistry, The University of Hong Kong, Hong Kong

CONTENTS

1. INTRODUCTION

There is a growing interest in calculating the electronic structures of complex and large systems like protein, molecular aggregates, and nanomaterials. With recent development in nanotechnology, we are increasingly interested in simulating the electric and optical processes of nanomaterials. *Ab initio* molecular orbital and semiempirical calculations are usually limited to small or medium-size molecular systems. The obstacle lies in the rapid increasing of computational costs as the systems become larger and more complex. The computational time t_{CPU} is proportional to a certain power of the system size; That is, $t_{\mathrm{CPU}} \propto N^x$,

ISBN: 1-58883-044-6

Handbook of Theoretical and Computational Nanotechnology
Edited by Michael Rieth and Wolfram Schommers
Volume 2: Pages (685–740)

where N is the number of electronic orbitals and x is an exponent which is usually larger than 2. For instance, *ab initio* Hartree–Fock (HF) molecular orbital calculation is a $O(N^3)$ scaling method, (i.e., $x = 3$). Table 1 shows the scalings of computational time versus the molecular size [1], N, for several electronic structure methods such as HF, density-functional theory (DFT) [2], second-order Moller–Plesset many-body perturbation theory (MP2) [3], coupled-cluster single-double excitation (CCSD), CCSD(triple) excitation [CCSD(T)] [4], and full-configuration interaction (FCI). Obviously, computational time increases rapidly with N, especially for more sophisticated methods. To determine the electronic structures of very large systems, it is essential that the computational cost scales linearly with N. Several linear-scaling methods have been developed to calculate ground electronic state [5–41], such as the divide-and-conquer method (DAC) [5, 6], the density matrix minimization (DMM) [10], the orbital minimization (OM) [12, 13], and the Fermi operator expansion (FOE) [20]. Linear-scaling coupled cluster theory [42–44], MP2 [45–47], quantum Monte Carlo [48, 49], and geometry optimization methods [50–52] have also been reported. The physical basis of these methods is "the nearsightedness of equilibrium systems" [53]. Traditional chemistry is based precisely on the local concepts. Covalently bonded materials are described in terms of bonds and lone electron pairs. Even in metallic systems, locality still applies. For instance, the total charge density in a metal is given reasonably well by the superposition of the atomic charge densities. Another example is that the magnetic moment of an iron atom embedded in an iron–aluminum alloy differs little from the value for pure iron if the atom is locally surrounded by eight iron atoms. This locality is not reflected in the conventional electronic structure calculations, which leads to unnecessarily expensive computational times for large molecular systems. All the above methods make use of the locality of density matrix or atomic orbital, and consequently result in the linear scaling of computational times versus the system size. These methods deal with electronic ground state only. Recent developments in nanotechnology and functional nanomaterials call for the efficient linear-scaling quantum mechanical (QM) method for electronic excited states. The excited states of very large electronic systems are much more difficult to calculate. Several linear-scaling calculations based on noninteracting-electron models have been carried out for excited states [15, 54, 55] and for the static electronic response [56, 57]. Chen and coworkers have developed a linear-scaling QM method for excited states of interacting electronic systems, the localized-density-matrix (LDM) method [58–63]. Unlike other linear-scaling methods for the excited states of noninteracting model systems, the LDM method explicitly treats the electron–electron Coulomb interaction.

In this article we review the methodologies of these linear-scaling QM methods and present in detail several of their applications to nanoscopic complex systems. In Section 2, we discuss the physical basis of all linear-scaling QM methods, the locality of density matrix for ground and excited states. In Section 3, we discuss the linear-scaling methods for ground state; in particular, DAC, DMM, OM, and FOE methods. Application of DAC method to examine the field emission mechanism of a micrometer-long carbon nanotubes is given in details. In Section 4, we first present two linear-scaling methods for excited states of noninteracting-electrons and then review the LDM methodology and its numerical implementations. Finally, calculations on light-harvesting system 2 (LH2) and poly(*p*-phenylenevinylene) (PPV) aggregates are presented. Concluding remarks are given in Section 5.

Table 1. Current scalings of electronic structure theory methods with molecular size, N.

Quantum mechanical method	Current computational dependence on molecular size, N
FCI	Factorial
CCSD(T)	N^7
CCSD	N^6
MP2	N^5
HF, DFT	N^3

2. NEARSIGHTEDNESS OF DENSITY MATRIX

The physical basis of linear-scaling methods is the nearsightedness of density matrices [53]. They are based on the locality in QM, which means that the properties of a certain observation region comprising one or a few atoms is only weakly influenced by factors that are spatially far away from the observation region. Most linear-scaling or $O(N)$ algorithms are built around the reduced single-electron density matrix or its representation in terms of Wannier functions and take advantage of its decay properties. To obtain the linear scaling, one has to cut off the exponentially decay quantities when they are small enough. This introduces the concept of a localization region. Only inside this localization region is the quantity calculated; outside it is assumed to vanish. Kohn proposed "the principle of the nearsightedness of equilibrium systems" to justify the locality of ground-state density matrix. Chen and Mukamel realized that the locality of density matrices persists for many excited states as well, and they showed that the off-diagonal ground-state density matrix elements are negligible when the distance between the two orbitals is larger than critical lengths l_0 and l_1 for ground and excited states, respectively [64]. Figure 1 shows the ground state and three excited-state density matrices for a (5,5) carbon nanotube. The scale of darkness represents the magnitude of the density matrix elements. The diagonal elements are the electron occupation numbers at various atomic orbitals, and the off-diagonal elements are the bond orders or the electron coherence between pairs of atomic orbitals [65]. As they move from the diagonal line, the matrix elements decay toward zero.

Theoretical models of periodic solids indicate that the locality of the one-particle density matrix is related to the size of the HOMO-LUMO (HOMO = higher occupied molecular

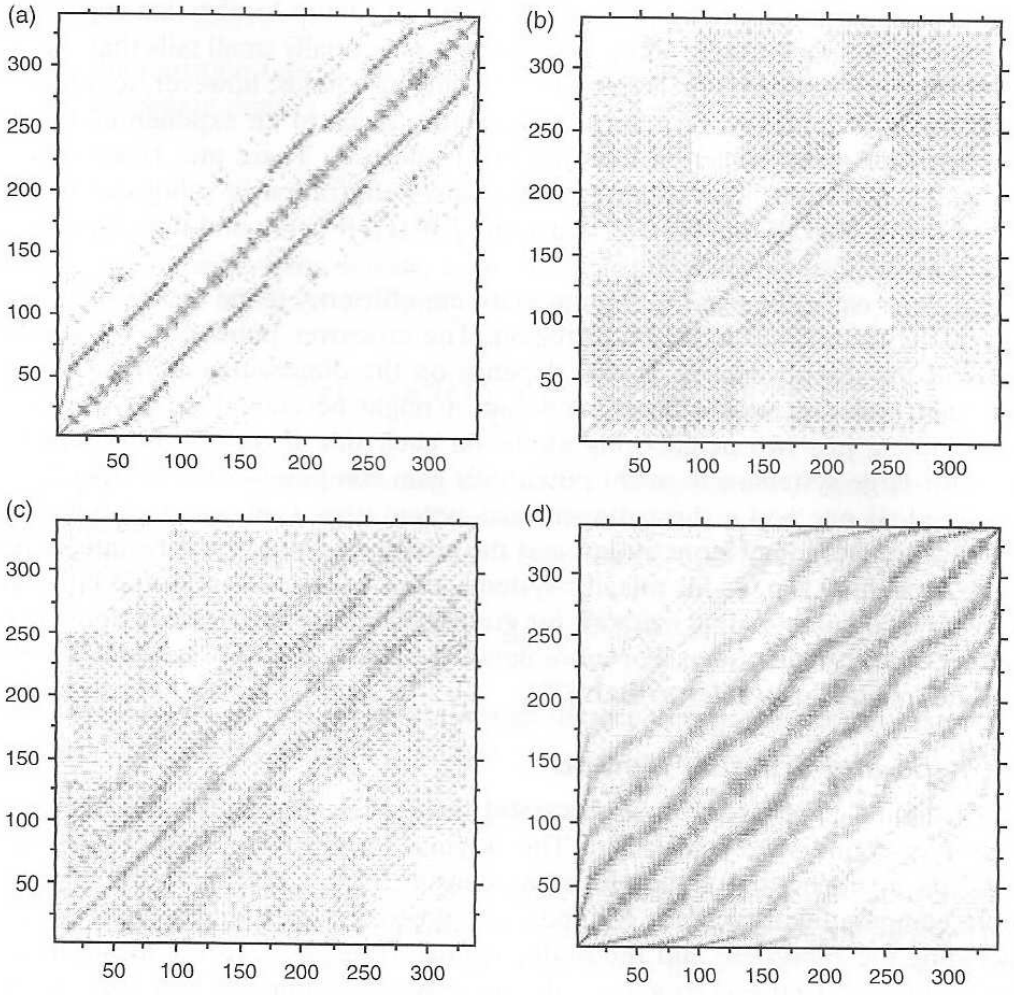

Figure 1. Density matrices of ground state (a) and three excited states (b, c, d) for a (5,5) $C_{80}H_{20}$ carbon nanotube. Reprinted with permission from [142], W. Z. Liang et al., *J. Am. Chem. Soc.* 122, 11129 (2000). © 2000, American Chemical Society.

orbital, LUMO = lowest unoccupied molecular orbital) gap, E_g (also known as the band gap). The density matrix ρ_{ij} decays asymptotically as [66–70]

$$\rho_{ij} \sim e^{-\sqrt{E_g} r_{ij}}, \quad E_g > 0 \tag{1}$$

and in metals, for which $E_g = 0$

$$\rho_{ij} \sim 1/|x_i - x_j||y_i - y_j||z_i - z_j| \tag{2}$$

However, the relationship between the HOMO-LUMO gap and decay of the density matrix has not been proven for arbitrary nonperiodic systems.

3. LINEAR-SCALING ELECTRONIC STRUCTURE METHODS FOR GROUND STATES

3.1. Methodology

In a numerical calculation, the density operator $\rho(r, r')$ is discretized with respect to a basis. The basis set has to be chosen such that the matrix elements reflect the decay properties of the operator. This is the case only if the basis set consists of localized functions, such as atom-centered Gaussian-type basis functions. Orthonormal basis functions usually facilitate the calculations. Unfortunately, most localized basis sets are nonorthogonal.

The size of the localization region depends on the decay properties of the density matrix as well as on the selected accuracy threshold. It also depends on the quantity that is to be studied. In general, the total energy as well as derived quantities such as the geometric equilibrium configurations are surprisingly insensitive to finite localization regions, because these quantities are not strongly influenced by the exponentially small tails that are cut off by the introduction of a localization region. This locality also holds, however, to a lesser extent, for metals. The introduction of a finite temperature leads to an exponential decay of the density matrix for metal, which in turn justifies truncation. There are, however, quantities that are very sensitive to finite localization regions. Polarization in solids can be expressed in terms of the centers of the Wannier functions $\int W(\mathbf{r})\mathbf{r}W(\mathbf{r})d\mathbf{r}$ and thus depends strongly on the tails of the Wannier functions.

Obviously one can gain significant computational efficiency if the extent of the system is larger than the size of the localization region. The crossover point depends on the decay properties of the density matrix. It also depends on the dimensionality of the system. For a linear-chain molecule with a large band gap, it might be enough to have a localization region containing just two neighboring atoms on each side if one is interested in ground state, and for large systems one might potentially gain computational efficiency by using an $O(N)$ method. If one had a three-dimensional system with a modest gap, the localization region would contain many more atoms, and the crossover point would be much larger. For a system with a small gap, or for metallic systems, the crossover point would be even larger. We review several linear-scaling methods for ground-state electronic calculations. The review is not intended to be exhaustive. For more detailed review on $O(N)$ methods for electronic ground state, readers may refer to Ref. [39].

3.1.1. Divide-and-Conquer Method

The DAC method [5, 6] is the first successful linear-scaling quantum mechanical method for electronic ground-state calculation. The original formulation of the DAC method [5] was based on a subdivision of the electronic density. This is done through the division of the whole computational volume. Around each subsystem, one puts a buffer region. The area including the subsystem and the buffer region corresponds to the localization region, as shown in Fig. 2. Electronic structure calculation is done within each localization region to obtain the density matrix. These calculations are only coupled by the requirement that the Fermi level be the same in all the localization regions. The density matrix is then truncated in the way that the regions in which both matrix indices belong to basis functions in the

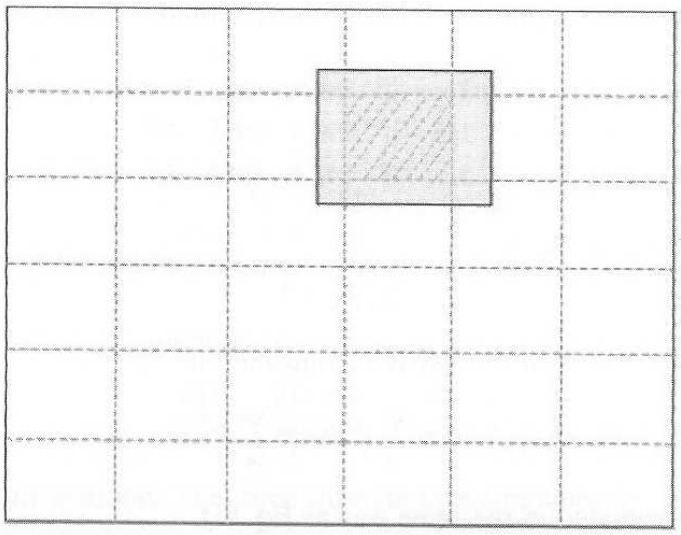

Figure 2. Subdivision of the whole computational volume. Highlighted area is the localization region.

buffer region are cut off. The final density matrix is obtained by adding up the different contributions with weights.

In the original DAC method [5], the electron density is the basic variable and is represented as the sum of contributions from subsystems. This is made possible through the normalized partition functions

$$\sum_{\alpha} p^{\alpha}(\mathbf{r}) = 1 \tag{3}$$

where p^{α} is the partition function for subsystem α. The total density $n(\mathbf{r})$ is then expressed as a sum of subsystem density $n^{\alpha}(\mathbf{r})$

$$n(\mathbf{r}) = \sum_{\alpha} p^{\alpha}(\mathbf{r}) n(\mathbf{r}) = \sum_{\alpha} n^{\alpha}(\mathbf{r}) \tag{4}$$

$n^{\alpha}(\mathbf{r})$, defined as a subsystem density, is localized in a small region of the physical space and therefore can be obtained efficiently with an approximation that depends on the local physical space

$$n^{\alpha}(\mathbf{r}) = 2p^{\alpha}(\mathbf{r}) \sum_{m} f_{\beta}(\epsilon_F - \epsilon_m^{\alpha}) |\psi_m^{\alpha}(\mathbf{r})|^2 \tag{5}$$

where $f_{\beta}(x)$, ϵ_F are the Fermi function with inverse temperature β and the Fermi energy, respectively. ψ_m^{α} and ϵ_m^{α} are local eigenfunctions and eigenvalues of the subsystem. $\psi^{\alpha}(\mathbf{r})$ is given by the linear combinations of the local basis functions $\phi^{\alpha}(\mathbf{r})$

$$\psi_m^{\alpha}(\mathbf{r}) = \sum_{i} c_{im}^{\alpha} \phi_i^{\alpha}(\mathbf{r}) \tag{6}$$

The linear coefficients c_{im}^{α} are obtained through the generalized eigenvalue equation derived from the Rayleigh–Ritz variational principle

$$(H^{\alpha} - \epsilon_m^{\alpha} S^{\alpha}) C_m^{\alpha} = 0 \tag{7}$$

where H and S are the Hamiltonian matrix and the overlap matrix, respectively.

The more recent formulation of this theory is based on density matrix ρ_{ij} [6]. The density matrix in the atomic orbital space $\{\phi_i(\mathbf{r})\}$ is given by the linear coefficients in the expansion of the molecular orbitals $\{\psi_i(\mathbf{r})\}$

$$\rho_{ij} = 2 \sum_{m}^{N/2} c_{im} c_{jm} \tag{8}$$

The corresponding partition matrix $\mathbf{p}_{ij}^{\alpha}$ in the atomic orbital space is defined as

$$\mathbf{p}_{ij}^{\alpha} = \begin{cases} 1 & \text{if } i \in \alpha \text{ and } j \in \alpha \\ 1/2 & \text{if } i \in \alpha \text{ and } j \notin \alpha \\ 0 & \text{if } i \notin \alpha \text{ and } j \notin \alpha \end{cases} \tag{9}$$

with the normalization condition

$$\sum \mathbf{p}_{ij}^{\alpha} = 1 \tag{10}$$

The density matrix is divided into subsystem contribution

$$\rho_{ij} = \sum_{\alpha} \mathbf{p}_{ij}^{\alpha} \rho_{ij} = \sum_{\alpha} \rho_{ij}^{\alpha} \tag{11}$$

and each ρ_{ij}^{α} is approximated in the same way as Eq. (5)

$$\rho_{ij}^{\alpha} = 2\mathbf{p}_{ij}^{\alpha} \sum_{m} f_{\beta}(\epsilon_F - \epsilon_m^{\alpha})\ c_{im}^{\alpha} c_{jm}^{\alpha} \tag{12}$$

The Fermi energy is determined by the normalization

$$N = \sum_{ij} \rho_{ij} S_{ij} = \sum_{ij} \left(2 \sum_{\alpha} \mathbf{p}_{ij}^{\alpha} \sum_{m} f_{\beta}(\epsilon_F - \epsilon_m^{\alpha})\ c_{im}^{\alpha} c_{jm}^{\alpha} \right) S_{ij} \tag{13}$$

and the sum of eigenvalues becomes

$$\epsilon = 2 \sum_{\alpha} \sum_{m} f_{\beta}(\epsilon_F - \epsilon_m^{\alpha}) \epsilon_m^{\alpha} \sum_{ij} \mathbf{p}_{ij}^{\alpha}\ c_{im}^{\alpha} c_{jm}^{\alpha} S_{ij} \tag{14}$$

$$= \sum_{ij} \left(2 \sum_{\alpha} \mathbf{p}_{ij}^{\alpha} \sum_{m} f_{\beta}(\epsilon_F - \epsilon_m^{\alpha})\ c_{im}^{\alpha} c_{jm}^{\alpha} \right) H_{ij} \tag{15}$$

Because the set of local eigenvectors for a subsystem is finite and independent of the size of the whole system, the computational time goes up linearly with the system size.

3.1.2. Density-Matrix Minimization Method

The DMM method [10] is another method by which the full-density matrix is constructed. The density matrix is obtained by minimizing the following functional for the grand potential Ω with respect to density matrix

$$\Omega = \mathrm{Tr}[(3\rho^2 - 2\rho^3)(H - \mu I)] \tag{16}$$

where μ is the chemical potential. There is no constraint imposed during the minimization, so all the density matrix elements are independent degrees of freedom. Nevertheless, the final density matrix obey the correct constraint of being a projector if no localization constraints are imposed. This is related to the fact that the matrix $3\rho^2 - 2\rho^3$ is a purified version of ρ [71].

The gradient of Ω, as given by Eq. (16) with respect to ρ, is itself a matrix and is given by

$$\frac{\partial \Omega}{\partial \rho} = 3(\rho H' + H'\rho) - 2(\rho^2 H' + \rho H' \rho + H' \rho^2) \tag{17}$$

where $H' = (H - \mu I)$. To verify that Eq. (16) defines a valid functional, one needs to show two things: first, that the grand potential expression Eq. (16) gives the correct result if the exact density matrix ρ is inserted, and second, the gradient Eq. (17) vanishes in this case. The density matrix is a projection operator; that is, $\rho^2 = \rho$. Therefore, $(3\rho^2 - 2\rho^3) = \rho$, and the grand potential expression agrees with the correct result

$$\Omega = \mathrm{Tr}[\rho(H - \mu I)] \tag{18}$$

The fact that H' and the exact ρ commute also ensure that the gradient in Eq. (17) vanishes. The gradient vanishes not only for the ground-state density matrix but also for the excited-state density matrix. To exclude the possibility of local minima, one has to verify that these stationary points are not minima. This can easily be done using the fact that the functional is a cubic polynomial with respect to all its degrees of freedom. Suppose that there are two minima, inspecting the functional along the line connecting these two minima, one would obviously find again these two minima, which is a contradiction because a cubic polynomial cannot have two minima. Thus, by contradiction, the DMM functional has only one single minimum.

The force acting on the nth atom at position R_n is given by

$$\frac{d\Omega}{dR_n} = \frac{\partial\Omega}{\partial\rho}\frac{\partial\rho}{\partial R_n} + \frac{\partial\Omega}{\partial H}\frac{\partial H}{\partial R_n} \tag{19}$$

and $\frac{\partial\Omega}{\partial\rho}$ vanishes at the solution. The force formula thus simplifies to

$$\frac{d\Omega}{dR_n} = \frac{\partial\Omega}{\partial H}\frac{\partial H}{\partial R_n} = \mathrm{Tr}\left[(3\rho^2 - 2\rho^3)\frac{\partial H}{\partial R_n}\right] \tag{20}$$

which can easily be evaluated.

All the arguments used to prove the absence of local minima remain valid in the truncated case as well. The force formula Eq. (20) remains equally valid. There is an alternative derivation of this algorithm [11] that considers a differential equation which describes the evolution of a density matrix when the electronic temperature is cooled down from infinity to zero. The change of the density matrix during process is equal to the gradient of Eq. (17).

3.1.3. Orbital Minimization Method

The OM method [12, 13] calculates the grand potential in the limit of zero temperature. In contrast to the previous methods, it does not calculate the density matrix directly but expresses it via the Wannier functions. These Wannier functions are obtained by minimizing the following unconstrained functional

$$\Omega = 2\sum_n\sum_{ij} c_i^n H'_{ij} c_j^n - \sum_{nm}\sum_{ij} c_i^n H'_{ij} c_j^m \sum_k c_k^n c_k^m \tag{21}$$

where c_i^n is the expansion coefficient of the nth Wannier orbital with respect to the ith basis function. The functional of Eq. (21) can be derived by considering the band-structure energy E_{BS} expression

$$E_{BS} = \sum_n\sum_{ij} c_i^n H'_{ij} c_j^n \tag{22}$$

and by incorporating the orthogonality constraint by a Taylor expansion of the inverse of the overlap matrix S between the occupied orbitals

$$S_{nm} = \sum_k c_k^n c_k^m \tag{23}$$

The gradient of the functional of Eq. (21) is given by

$$\frac{\partial\Omega}{\partial c_k^n} = 4\sum_i H'_{ki} c_i^n - 2\sum_m\sum_i H'_{ki} c_i^m \sum_k c_k^n c_k^m - 2\sum_m c_k^m \sum_{ij} c_i^n H'_{ij} c_j^m \tag{24}$$

Instead of Wannier orbitals, Ω and $\partial\Omega/\partial c$ are expressed in terms of eigenorbitals. Use the fact that $\sum_k c_k^n c_k^m = \delta_{nm}$ and $\sum_{ij} c_i^n H'_{ij} c_j^m = \delta_{nm}(\epsilon_n - \mu)$, and obtain

$$\Omega = 2\sum_n\sum_{ij} c_i^n H'_{ij} c_j^n - \sum_{nm}\sum_{ij} c_i^n H'_{ij} c_j^m \delta_{nm} \tag{25}$$

$$= \sum_n\sum_{ij} c_i^n H'_{ij} c_j^n = \sum_n \epsilon_n - \mu N \tag{26}$$

so the gradient equation can be simplified

$$\frac{\partial \Omega}{\partial c_k^n} = 4\sum_i H'_{ki} c_i^n - 2\sum_m \sum_i H'_{ki} c_i^m \delta_{nm} - 2c_k^n \sum_m \delta_{nm}(\epsilon_m - \mu) \tag{27}$$

$$= 2\sum_i H'_{ki} c_i^n - 2c_k^n(\epsilon_n - \mu) = 0 \tag{28}$$

So the functional has indeed a vanishing gradient at the ground state, and its gives the correct ground-state energy. As was the case for the DMM functional, the gradient vanishes not only for the ground-state orbitals but also for the excited-state orbitals. It is shown that these stationary points are not local minima [12, 13]. In analogy to the DMM functional, one can also show that the chemical potential μ determines the number of electrons by amplifying components below μ and annihilating components above it [72].

Whereas the DMM functional keeps all its good properties when one introduces a localization constraint, the OM functional loses most of them. The localization constraint is introduced in the OM functional by allowing each Wannier orbital to deviate from zero only within its own localization region. These localization regions are usually atom centered and contain a few shells of neighboring atoms. The basic idea of the OM functional, namely, of describing an electronic system by a set of Wannier functions with finite support, are mutually exclusive properties, and so the orbitals that one obtains in the minimization process are necessarily nonorthogonal.

3.1.4. Chebyshev Fermi Operator Expansion

The Fermi operator expansion (FOE) [20, 73] is the most straightforward approach for the calculation of the density matrix. The basic idea in this approach is to find a representation of the matrix function that can be evaluated on a computer. Several such representations are possible and we discuss the Chebyshev representation.

One of the most basic operations a computer can do is a matrix-times-vector multiplication. The simplest representation of the density matrix, requiring only this operation, would be a polynomial representation

$$\rho \approx p(H) = c_0 I + c_1 H + c_2 H^2 + \cdots + c_n H^n \tag{29}$$

where I is the identity matrix. Unfortunately, polynomials of high degree become numerically unstable. This instability can be avoided by introducing a Chebyshev polynomial representation, which is a widely used numerical method [74]

$$p(H) = \frac{c_0}{2} I + \sum_{i=1}^{n} c_i T_i(H) \tag{30}$$

Because the Chebyshev polynomials are defined only within interval [−1:1], we shall assume in the following that the eigenvalue spectrum of H falls within this interval. This can always be easily achieved by scaling and shifting of the original Hamiltonian. The Chebyshev matrix polynomials $T_i(H)$ satisfy the recursion relations

$$T_0(H) = I \tag{31}$$

$$T_1(H) = H \tag{32}$$

$$T_{i+1}(H) = 2HT_i(H) - T_{i-1}(H) \tag{33}$$

The expansion coefficients of the Chebyshev expansion can easily be determined. Evaluating the polynomial expansion in the same eigenfunction representation, we obtain

$$\langle \Psi_n | p(H) | \Psi_m \rangle = p(\epsilon_n)\delta_{nm} \tag{34}$$

where

$$p(\epsilon) = \frac{c_0}{2} + \sum_{i=1}^{n} c_i T_i(\epsilon) \tag{35}$$

The way to find the Chebyshev expansion coefficients for a scalar function is described in standard textbooks on numerical analysis [74].

The desired linear-scaling can be obtained by introducing a localization region for each column, outside of which the elements are negligibly small. For the kth column, this localization region is centered on the kth basis function.

3.1.5. Other O(N) Methods

Unlike the FOE method, the Fermi operator projection (FOP) method applied to zero temperature [75]. If one has a numerical representation of the zero-temperature density operator that deletes all components belonging to eigenvalues above the Fermi level, one can use it to generate a set of occupied molecular orbitals. The Fermi operator is projected onto a set of localized Wannier functions. The DMM method has a big disadvantage that it is very inefficient if very large basis set is required. The optimal basis density matrix minimization (OBDMM) method [76] was developed to overcome this obstacle. The basic idea is first to contract the fundamental basis functions into a small number of new basis functions and then to set up the Hamiltonian and overlap matrix in the new small basis set. The recursion method is principally a method to calculate the density of states $D(\epsilon)$ from which the band structure can be easily obtained [17, 77]. The drawback of its original formulation is that only diagonal elements of density matrix can be evaluated, which is a serious set back if one is interested in the forces that require the off-diagonal density matrix elements. Subsequent development was aimed to overcome this problem with limited success [18, 78, 79]. There are other linear-scaling methods that calculate the density of states [15, 80, 81]. Another linear-scaling method for ground state is the pseudo-diagonalization method [82]. It resembles the well-known Jacobi method for matrix diagonalization, which the rotation transformations are applied until all off-diagonal elements vanish. A precursor of the OM method was developed by Galli and Parrinello [8]. Instead of having the orthogonalization constraint in the modified functional, they minimized the conventional functional under explicit constraint of orthogonality. A multiple-scattering theory has been developed to calculate the electronic properties of large systems [83]. It is essentially a DAC method except that the scattering method is employed for each localization region. The polynomial FOE method is rather inefficient for large basis set, which causes the highest eigenvalue to grow drastically. This requires thus a Chebyshev polynomial of very high degree. An excellent resummation method has been developed by Liang and Head-Gordon to greatly reduce the computational time for evaluating Chebyshev expansion [84]. Linear-scaling methods for evaluating the self-consistent potential have been developed. This potential consists essentially of the electrostatic and the exchange-correlation (XC) potential. Considerable effort has been spent on achieving linear scaling of the Coulomb repulsion [25, 85–90]. Linear-scaling evaluation of the XC quadratures can be achieved by exploiting the localized nature of XC potential [91, 92]. Several $O(N)$ methods are also developed to deal with the HF exchange part [93–95]. These methods are essential for any linear-scaling self-consistent first-principles electronic structure calculations. Much effort has also been devoted to optimizing basis functions for linear-scaling electronic structure calculations [96–103].

3.2. Applications: Quantum Mechanical Investigation of Field Emission Mechanism of a Micrometer-Long Single-Walled Carbon Nanotube

Carbon nanotubes (CNTs) have been acknowledged as exceptionally efficient electron-field emitters. Their ultrahigh aspect ratios lead to extremely low turn-on fields and intense current densities [104, 105]. Under a strong applied external field, it was found that the classical Fowler-Nordheim (FN) law [106] is no longer valid [107, 108]. Therefore, a QM investigation becomes indispensable to understand the field emission mechanism. DFT has been employed to calculate the electrostatic fields, charge distributions, and electronic states near the tips [109]. However, limited by the computational efficiency and resources, only the CNT tips of a few nanometers in length were considered explicitly in these calculations. This was justified under the assumption that the external fields can be scaled by a factor of $(L_{\text{tube}}/L_{\text{tip}})$ for the shortened CNTs to retain the actual charge distributions or electrostatic fields around

the tips [110], where L_{tip} and L_{tube} are the lengths of the tip used in the calculation and the genuine tube used in the experiment, respectively. The scaled field E_{scal} is much stronger than the applied field E_{appl}, which leads to the localized electronic states at the very tip, where the electrons are expected to emit [111]. The validity of this assumption needs to be examined. Further, excessive electrons have significant effects on the potential at the tip region, and subsequently on the emission process [109]. The amount of extra electrons around the tip has not been determined and was varied to assess their effects in previous calculations [109]. Classically, a metallic field emitter has the same electrostatic potential as the cathode that it is connected to, and the electric field is completely shielded by the charges on the surface of the emitter. However, CNTs have very thin tube walls. In particular, a single-walled carbon nanotube (SWNT) consists of only one layer of carbon atoms. It is known that field penetration lengths for metals are a few angstroms or larger [112], so it would be interesting to examine whether the electric field penetrates the tube, which may result in a unconventional field emission mechanism. When there are excessive charges distributed along the tube, the entire tube and the substrate must be considered because the Coulomb interaction is long ranged. All these facts call for the explicit treatment of entire tube and boundary condition in the calculation. Unlike the isolated systems that most conventional quantum simulations deal with, the SWNT in this study is an open system that exchanges energy and matter with the surroundings.

It is an enormous computational challenge to simulate explicitly a 1-μm-long (5,5) SWNT that contains about 10^5 atoms. In addition, the boundary condition presents a complication. Figure 3a depicts a typical field-emission system. In the QM model, the SWNT ceases to be an equipotential entity with the metal cathode. Instead, it is connected to the cathode, which provides electrons to the tube on the following boundary condition (also see Fig. 3a):

$$V = \begin{cases} V_a > 0 & \text{Anode} \\ 0 & \text{Cathode} \end{cases} \tag{36}$$

To simulate the entire tube, Zheng et al. adopted a hybrid QM and molecular mechanics (QM/MM) approach [113] in which ~8000 atoms at or near the tip are simulated quantum mechanically while the rest along the tube are treated as point charges because their predominant influence on the emission is through their electrostatic potential at the tip [114]. Under the applied external field E_{appl}, the energies of local orbitals are lowered. Some of them are lowered below the Fermi energy, and the electrons are induced from the cathode to subsequently occupy these local orbitals. The number of these local orbitals is proportional to their energy change, provided that the density of states (DOS) is a constant. Numerical calculations [115, 116] and experiments [117] revealed that the DOS near the Fermi energy is approximately constant. The energy changes of the local orbitals at a position z are approximately the change of local electrostatic potential energy $\delta V(z)$. Therefore, the number of the local orbitals whose energies are lower than the Fermi energy is proportional

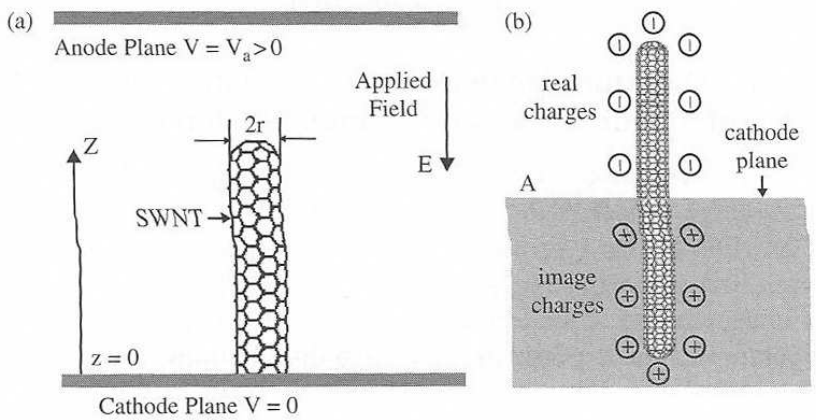

Figure 3. (a) Field emission setup for a SWNT. (b) Mirror images of the induced charges. Reprinted with permission from [114], X. Zheng et al., *Phys. Rev. Lett.* 92, 106803 (2004). © 2004, American Physical Society.

to $\delta V(z)$; that is, the induced charge density $n(z) \propto \delta V(z)$. This expression is consistent with the Thomas–Fermi theory and is a good approximation when $n(z)$ or $\delta V(z)$ is relatively small. According to Poisson's equation $\nabla^2 \delta V(z) \propto n(z)$, $\nabla^2 n(z) \propto n(z)$ is obtained, and subsequently the linear induced charge density (or charge per unit length) along the tube $\rho(z)$ can be expressed as

$$\rho(z) \sim \rho(L') \cdot \exp\left\{\frac{-(L'-z)}{\lambda}\right\} \tag{37}$$

In Eq. (37), λ represents the decay length, and $\rho(L')$ is the linear induced charge density at $z = L'$, where QM and MM regions in the simulations intersect. The term $\rho(L')$ can be determined from the QM region. Yang [5] has developed an efficient linear-scaling DAC method to calculate the ground-state electronic structures of large molecular systems. A system is divided into subsystems that are simulated quantum mechanically one at a time, and contributions from each subsystem are reassembled rationally to recover the physical properties of the whole system. The DAC method is adopted to calculate the charge distribution among the 8000 atoms in the tip region. Being connected to the cathode, the SWNT can be treated as in quasi-equilibrium with the cathode before the electrons emit or when the current is minute. This provides a perfect solution to determine the amount of electrons that the cathode provides to the tube, as the Fermi energy has to be a constant throughout the cathode and SWNT. The boundary condition is further satisfied by introducing the mirror images of the charges distributed along the tube, as illustrated in Fig. 3b. The combined electrostatic potential is thus constant at the middle plane A, the surface of the semi-infinite cathode.

The semiempirical modified neglect of diatomic overlap (MNDO) model [118] is adopted in the calculation. The Hamiltonian of the QM region involving 8000 atoms (denoted as system qm) in the presence of an external field is described as

$$H^{\mathrm{qm}} = \sum_{i,j\in \mathrm{qm}} t_{ij} a_i^+ a_j + \frac{1}{2} \sum_{m,n,i,j\in \mathrm{qm}} V_{mn,ij} a_n^+ a_i^+ a_j a_m - \mathbf{E}_{\mathrm{appl}} \cdot \sum_{i,j\in \mathrm{qm}} \mathbf{P}_{ij} a_i^+ a_j \tag{38}$$

where a_i^+ (a_j) is the creation (annihilation) operator for an electron at a local atomic spin orbital i (j), t_{ij} is the one-electron integral between i and j, $V_{mn,ij}$ is the two-electron integral, and $\mathbf{P}_{ij}$ is the dipole moment operator between i and j. The variable t_{ij} is expressed as

$$t_{ij} = \left\langle i \left| -\frac{1}{2}\nabla_{\mathrm{r}}^2 + U^{\mathrm{qm}}(\mathbf{r}) + U^{\mathrm{mm}}(\mathbf{r}) + U^{\mathrm{img}}(\mathbf{r}) \right| j \right\rangle \tag{39}$$

where $U^{\mathrm{qm}}(\mathbf{r})$, $U^{\mathrm{mm}}(\mathbf{r})$ and $U^{\mathrm{img}}(\mathbf{r})$ correspond to the one-electron electrostatic potentials from the nuclei and core electrons in QM, the rest of the tube or the MM region, and the image charges, respectively. Concerning the DAC procedures, buffer zones are introduced at the boundaries of each subsystem to account for the chemical bonds and near-field interactions between neighboring subsystems. Hydrogen atoms are further introduced to terminate the dangling bonds in the buffer zones. The sizes of buffer zones are flexible and are tuned to accommodate excessive electrons on the constraint that the Fermi energy remains constant everywhere in the joint system. The Fermi energy of the cathode is set to the work function of tungsten, −4.5 eV, and the Fermi energy of the neutral long SWNT(5,5) is set at −4.68 eV, according to the early findings [119]. Starting with an initial linear induced charge distribution, an iteration of DAC calculation is conducted for the 8000 atoms in the tip region, and its results are used to update the values of λ and $\rho(L')$. The above steps are then iterated until a convergence of the induced charge distribution $\rho(z)$ along the entire tube is achieved.

The applied external field in the simulation ranges between 10 and 14 $\mathrm{V}\mu\mathrm{m}^{-1}$. The number of atoms within individual combined subsystem/buffer-zones varies from 120 to 400. Initial λ is set between 0.10 and 0.25 μm, and initial $\rho(L')$ are between 0.30 and 0.90 electron/nm. Usually more than three iterations are required before the values of λ and $\rho(L')$ are converged, and a few more are performed supplementally to ensure the detailed convergence of global density matrix.

In Fig. 4, the induced charge distributions at the cap and along the tube are plotted for the external field 14 Vμm^{-1}. Figure 4a depicts the induced electron density in a plane that goes through the five atoms at the end of cap, and Fig. 4b is the induced charge distribution in a middle plane bisecting the tube. The induced charges are only a few percentages of the total number of electrons at the tip. Figure 4c shows the induced charges layer by layer along the z-axis. A standing wave is observed for the excessive charges. The inset of Fig. 4c depicts the excessive charges for the entire tube, which are found concentrating at the tip region (similar to the classical metallic tube). The term λ is 0.48 μm and $\rho(L')$ 0.66 electron/nm for $E_{\text{appl}} = 14$ Vμm^{-1}, whereas λ is 0.45 μm and $\rho(L')$ 0.50 electron/nm for $E_{\text{appl}} = 10$ Vμm^{-1}. The fact that the decay length λ is almost half micrometer confirms the necessity of considering explicitly the entire carbon nanotube.

Figure 5 exhibits the potential energy contours for an electron under the external field of 14 Vμm^{-1}. It is significant to note that the potential drop concentrates mostly at the tip region (see Fig. 5a). This indicates that the electric field penetrates strongly at the tip. Despite the strong field penetration at the tip, the variation of electrostatic potential along the bulk of the tube is only about 2 V, much less than the applied bias voltage. The contour plot around the cap is amplified in Fig. 5b, where the deep blue region represents the tube wall, and the dotted line is the energy contour for the Fermi energy (−4.5 eV). Obviously, the Fermi energy is below the potential barriers around the cap. The electric field is much stronger outside the tube compared to that inside. Potential barriers on the sidewall are much higher and thicker than that in front of the cap. Forward emission from the cap encounters the barrier with minimum height and thickness, and is thus expected. Similar potential contour plot is obtained for $E_{\text{appl}} = 10$ Vμm^{-1}, and the field penetration is found to be weaker.

Figure 6(a) shows the electrostatic potentials along the central axis near the end for three cases (i.e., $E_{\text{appl}} = 0, 10$ and 14 Vμm^{-1}). As E_{appl} increases, the barrier height is

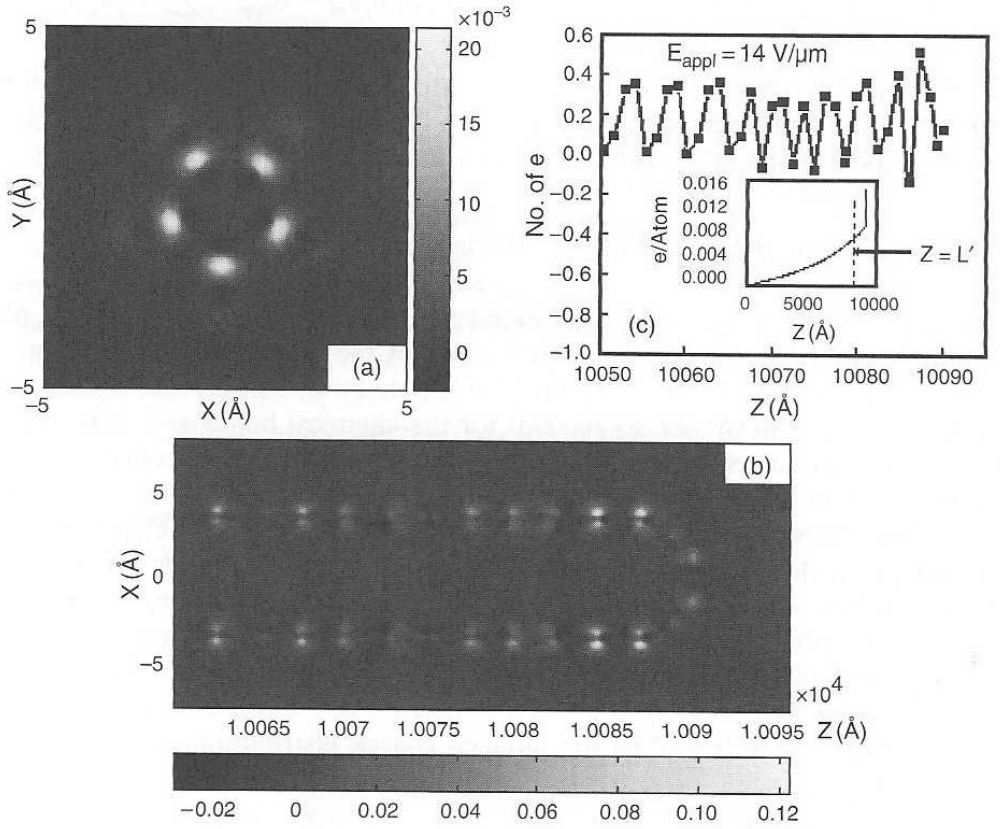

Figure 4. (a) Induced charge distribution at the top layer of the SWNT's cap. (b) Induced charge distribution in a middle plane bisecting the tube. (c) Number of induced electrons on each layer along the z-axis in the tip region. Excessive charges on the entire tube are depicted in the insert. All charge densities in (a) and (b) are in unit of electron Å^3. Reprinted with permission from [114], X. Zheng et al., *Phys. Rev. Lett.* 92, 106803 (2004). © 2004, American Physical Society.

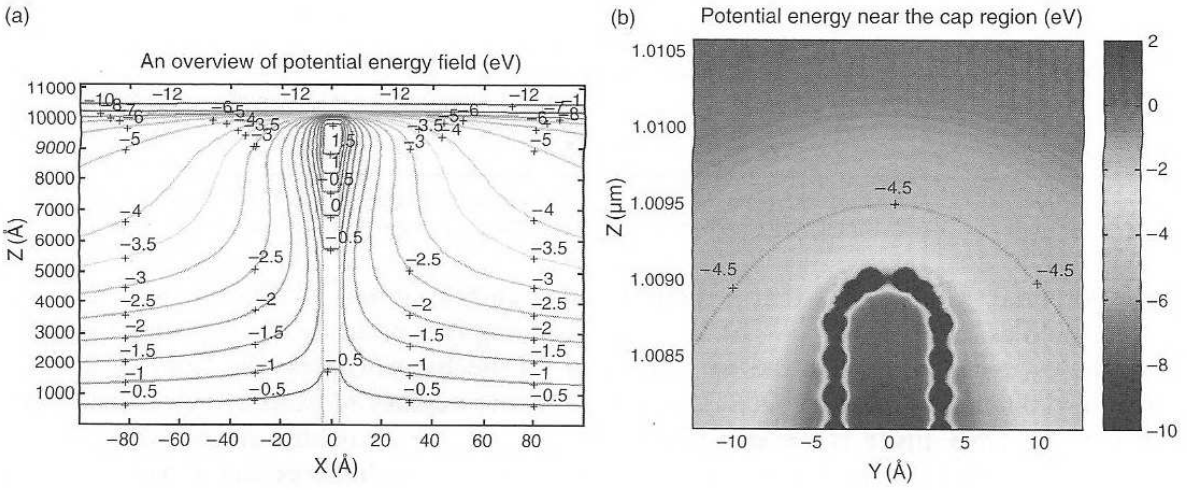

Figure 5. Potential energy contour plots (a) for the (5,5) SWNT and (b) in the vicinity of the cap under E_{appl} = 14 Vμm^{-1}. To keep the image clear, the core potential is cut at −10 eV. The dashed line in (b) is the equipotential line for the Fermi energy (−4.5 eV). Reprinted with permission from [114], X. Zheng et al., *Phys. Rev. Lett.* 92, 106803 (2004). © 2004, American Physical Society.

lowered. The values of barrier height are listed in Table 2. Obviously, the barrier height depends nonlinearly on the external field and is lowered by as much as 2.5 eV for E_{appl} = 14 Vμm^{-1}. Meanwhile, its thickness decreases rapidly and the emission current intensifies drastically. It is emphasized that the lowering of potential barrier is not caused by the image charges of the emitting electrons [120] but by the field penetration at the tip. The local fields in front of the tip averaged over the range from z = 10091.5 to 10095 Å are 3.1 Vnm^{-1} and 5.7 Vnm^{-1} for E_{appl} = 10 and 14 Vμm^{-1}, respectively. The corresponding ratios of the local field to the applied field are thus 310 and 410, respectively. The lowering of the barrier height increases further the effective field enhancement factor. Using the FN law [106], it is found that the effective enhancement factors are 500 and 1200 for E_{appl} = 10 and 14 Vμm^{-1}, respectively. Figure 6(b) is the electrostatic potential plotted along the A-B-C-D path. A steep potential well is observed between z = 10040 and 10090 Å, which is similar to the bending of conduction bands of semiconductors under the applied field. This phenomenon is distinctively different from that of the conventional model, which treats the emissive carbon nanotubes as ideal metals [121]. As a consequence, excessive electrons have high density in the tip region. The excessive charges in the first carbon layer of the tip are q_{exc} = 0.095 and 0.13 electron for E_{appl} = 10 and 14 Vμm^{-1}, respectively. The electrostatic potential along the entire tube is plotted for E_{appl} = 10 Vμm^{-1} in the inset of Fig. 6(a). Similar to that of E_{appl} = 14 Vμm^{-1} (cf. Fig. 5a), most of the tube is approximately of the

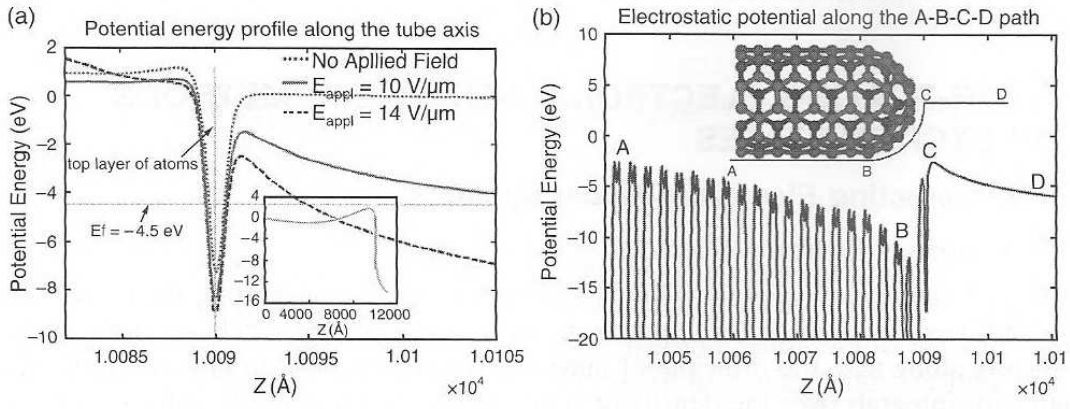

Figure 6. (a) Potential energy profiles in the vicinity of the cap under different applied fields. Data are extracted along the central axis of the carbon nanotube. The electrostatic potential along the entire tube for E_{appl} = 10 Vμm^{-1} is presented in the insert. (b) Electrostatic potential along the A-B-C-D path that is embedded in the tube wall as specified by the insert (E_{appl} = 14 Vμm^{-1}). Reprinted with permission from [114], X. Zheng et al., *Phys. Rev. Lett.* 92, 106803 (2004). © 2004, American Physical Society.

Table 2. The potential barrier height ϕ with respect to the Fermi level under the applied field $E_{\text{appl}} = 0$, 10 and 14 Vμm^{-1}.

E_{appl}	0	$E_{\text{appl}} = 10$ Vμm^{-1}	$E_{\text{appl}} = 14$ Vμm^{-1}
ϕ	4.5 eV	3.0 eV	2.0 eV

Reprinted with permission from [114], X. Zheng et al., *Phys. Rev. Lett.* 92, 106803 (2004) © 2004, American Physical Society.

same potential. This implies that a single layer of carbon atoms is sufficient to screen the electric field as strong as $E_{\text{appl}} \sim 10$ Vμm^{-1}. Assuming that emitting electrons mainly come from the excessive charges in the π^* states near to the Fermi energy, the emission current can be estimated by $J = ev q_{\text{exc}} D(E_f)$, where q_{exc} is the number of excessive electrons in the first layer of CNT tip, ν is the impinging frequency that is estimated from the π^* orbital energy $E(\pi^*)$, and $D(E)$ is the transmission probability through the potential barrier, which is estimated by the WKB approximation. The emission currents are found to be 0.44 pA and 8.41 μA for $E_{\text{appl}} = 10$ and 14 Vμm^{-1}, respectively, which amounts are comparable to the experimental findings [120].

Zettl and coworkers performed an electron holography measurement of the electric field distribution along a field-emitting multiwalled CNT [120]. They have found that the field emission current concentrates precisely at the tip and not at the tube defects, such as sidewall imperfections, and the measured holography is consistent with the scenario that there is no potential drop along the micrometer-long tube. Our results are consistent with their findings. This is because that π^* orbitals are empty before the application of electric field and can accommodate enough electrons to shield the applied field. The shielding of the electric field is a natural consequence of the equilibrium condition that the Fermi energy or chemical potential is constant throughout the system (the SWNT plus the cathode). Although the external field lowers the energies of local orbitals, the electrostatic interactions from the induced electrons bring up the HOMOs to the Fermi energy of cathode. As a result, the electric field is shielded for most of the tube while penetrating the tip.

By employing a linear-scaling DAC technique, a detailed QM simulation of a 1-μm-long SWNT(5,5) is carried out under realistic field emission experimental conditions. Induced charge distribution and electrostatic potential before the emission are determined. Except for the tip, a single layer of carbon atoms is sufficient to shield the most of strong electric field for the bulk of the SWNT. The field penetration at the tip lowers the potential barrier and leads to the deep potential well in the tip region, where large amounts of excessive electrons reside. In addition to the classical local field enhancement immediately outside the tip, the lowering of barrier height leads to further significant increase of emitting current. This reveals the unconventional nature of CNT field emission mechanism. The potential barrier height is a nonlinear function of the applied field and is system-dependent. It is thus likely that the modification of the tip may lead to drastic alternation of emission current or threshold voltage.

4. LINEAR-SCALING ELECTRONIC STRUCTURE METHODS FOR EXCITED STATES

4.1. Noninteracting Electronic Model Systems

4.1.1. Maximum Entropy Method

Drabold and Sankey [15] present a linear-scaling method for calculating the band-structure energy and density of states for large electronic systems. A statistical approach using random vectors along with the principle of maximum entropy is used to obtain highly accurate estimates for integrals over the density of states. It is noted that all the information carried by the density of states is contained in any one single vector ξ in the family of vectors of the form

$$\xi = \sum_{i=1}^{N} \frac{e^{i\phi_i}\psi_i}{\sqrt{N}} \tag{40}$$

where ϕ_i specifies an arbitrary phase. The expectation value of the DOS operator between any ξ gives the exact density of states, $\rho(E) = \langle\xi|\hat{\rho}(E)|\xi\rangle$. The Hamiltonian H has moments μ_n

$$\mu_n = \int_{-\infty}^{\infty} dE E^n \rho(E) = \frac{1}{N}\mathrm{Tr}H^n \tag{41}$$

and the vector ξ also gives exact moments through its expectation value

$$\mu_n = \langle\xi|H^n|\xi\rangle \tag{42}$$

and this is an $O(N)$ operation, while taking the trace in Eq. (41) is not.

The first step is to approximate ξ. An appropriate random vector x is selected and a penalty function method is used to find an improved vector x^*. The second step involves transforming the information contained in ξ into $\rho(E)$ in an $O(N)$ way. This is accomplished by viewing $\rho(E)$ as a probability distribution and using the maximum entropy principle to determine the best estimate from partial information.

The key feature in this work is the use of important sampling in the process of accumulating moment data from H. This dramatically improves the method for practical use. To implement this, a penalty function of a vector x is constructed, subjecting it to three constraints (μ_0, μ_1, μ_2)

$$P(x) = (\langle x|x\rangle - \mu_0)^2 + (\langle x|H|x\rangle - \mu_1)^2 + (\langle x|HH|x\rangle - \mu_2)^2 \tag{43}$$

The exact moments μ_1 and μ_2 are $O(N)$ calculable. The function in Eq. (43) is minimized with a conjugate gradient method [74]. The other key step is to transform the information contained in x^* into $\rho(E)$ through moment data.

4.1.2. Time-Dependent Schrödinger Equation

This method applies only to noninteracting electronic model systems [54]. The linear response function $\chi_{BA}(\omega + i\eta)$ of an observable B caused by a monochromatic perturbation $H^{ex} = e^{-i(\omega+i\eta)t}A$ is calculated by the time-dependent perturbation theory

$$\chi_{BA}(\omega + i\eta) = (-i)\int_0^{\infty} dt\ e^{+i(\omega+i\eta)t}\{\langle E_g|e^{+iHt}Be^{-iHt}A|E_g\rangle - \text{c.c.}\} \tag{44}$$

$$\approx 2\int_0^{T} dt\ e^{+i(\omega+i\eta)t}\mathrm{Im}\{\langle E_g|Be^{-iHt}A|E_g\rangle e^{+iE_g t}\} \tag{45}$$

where $|E_g\rangle$ and E_g are the ground state of the many electron system and its energy, respectively; ω and η are the frequency and its resolution, respectively; c.c. indicates the complex conjugate; and atomic units are used. In the numerical calculation of Eq. (45), we have to discretize it in time

$$\chi_{BA}(\omega + i\eta) = 2\sum_{m=0}^{M}\Delta t\ e^{+i(\omega+i\eta)m\Delta t}\mathrm{Im}\{\langle E_g|Be^{-iHm\Delta t}A|E_g\rangle e^{+iE_g m\Delta t}\} \tag{46}$$

where $M = T/\Delta t$ is the number of time steps, T is the integration time, and Δt is the width of the time step.

Next, the estimated computational efforts is shown. The diagonalization method for the $N \times N$ Hamiltonian matrix requires the memory space of $O(N^2)$ and the computational effort of $O(N^3)$. In contrast, the time-dependent method requires the memory space of $O(N^2)$ and the computational effort of $O(MN^2)$, where M is the number of time steps that is determined by the required energy resolution. By choosing an appropriate basis set, the Hamiltonian matrix will have only $O(N)$ nonzero matrix elements. This results in $O(MN)$ computational effort and $O(N)$ memory space requirement of the time-dependent method. Thus, the time-dependent method can be more efficient than diagonalization method in the large N limit.

4.2. Localized-Density-Matrix Method

Instead of solving for the many-body wave function, the equation of motion (EOM) of the reduced single-electron density matrix is followed. A reduced single-electron density matrix ρ contains important information of an electronic system. The diagonal element ρ_{ii} is the electron density at a local orbital i, and the off-diagonal element $\rho_{ij}(i \neq j)$ measures the electronic coherence between two local orbitals i and j, where $\rho_{ij} = \langle \hat{a}_j^{\not\in} \hat{a}_i \rangle$, and $\hat{a}_j^{\not\in}$ and $\hat{a}_i$ are the creation and annihilation operators at j and i, respectively. The EOM is based on the time-dependent HF (TDHF) approximation [122], and the time for its solution scales as $O(N^6)$. The TDHF includes the complete single-electron excitations and some partial double-, triple-, and other multielectron excitations. It has been applied successfully to investigate the optical properties of conjugated polymers [123]. It has been shown that off-diagonal elements ρ_{ij} are negligible when the distance r_{ij} between i and j is larger than a critical length l_0 [64]. This is a consequence of "nearsightedness" of reduced single-electron density matrix [53]. When the system is subjected to an external field $\mathscr{E}(t)$, the field induces a change $\delta\rho$ in the reduced density matrix. The induced density matrix $\delta\rho$ has a similar "nearsightedness" [64]. Different orders of responses in $\mathscr{E}(t)$ have different critical lengths. Usually the higher the order of response n is, the longer the critical length l_n is (i.e., $l_0 < l_1 < l_2 < l_3 < \ldots$). The nth-order induced density matrix response $\delta\rho^{(n)}$ is truncated by setting its elements $\rho_{ij}^{(n)}$ to zero for $r_{ij} > l_n$. This truncation may lead to a drastic reduction of the computational time.

4.2.1. Frequency Domain Localized-Density-Matrix Method

When an external electromagnetic field is applied to a polyacetylene oligomer, its π electrons response to the field, and the optical signals may be observed. The π electrons may be characterized by the PPP Hamiltonian [123, 124]

$$H = H_{\text{SSH}} + H_{\text{C}} + H_{\text{ext}} \tag{47}$$

where H_{SSH} is the Su–Schrieffer–Heeger (SSH) Hamiltonian, which consists of the Hückel Hamiltonian with electron-phonon coupling. The term H_{C} represents the Coulomb interaction among π electron or nuclei, which is described by the Ohno formula [125]; H_{ext} is the interaction between π electrons and the external electric field $\mathscr{E}(t)$; and the reduced single-electron density matrix element $\rho_{ij}(t)$ obeys the Heisenberg equation of motion, where $i(j)$ represents π orbital at carbon atom $i(j)$. With the TDHF approximation, a closed, nonlinear self-consistent EOM is yielded for the reduced single-electron density matrix $\rho(t)$

$$i\hbar\dot{\rho}(t) = [h(t) + f(t), \rho(t)] \tag{48}$$

Here $h(t)$ is the Fock matrix

$$h_{nm}(t) = t_{nm} + 2\delta_{n,m} \sum_l v_{nl}\rho_{ll}(t) - v_{nm}\rho_{nm}(t) \tag{49}$$

with t_{nm} being the hopping matrix element between n and m, and v_{nm} the Coulomb repulsion between two electrons at n and m, respectively; $f(t)$ represents the interaction between an electron and the external field $\mathscr{E}(t)$

$$f_{nm}(t) = \delta_{n,m} ez(n) \mathscr{E}(t) \tag{50}$$

The density matrix $\rho(t)$ is partitioned into two parts

$$\rho(t) = \rho^{(0)} + \delta\rho(t) \tag{51}$$

where $\rho^{(0)}$ is the single-electron density matrix representing the HF ground state in the absence of the external field, and $\delta\rho(t)$ is the difference between $\rho(t)$ and $\rho^{(0)}$. Similarly, the Fock matrix $h(t)$ is decomposed in the form

$$h(t) = h^{(0)} + \delta h(t) \tag{52}$$

where $h^{(0)}$ is the Fock matrix when $\mathscr{E}(t) = 0$. Equation (49) thus becomes

$$i\hbar\delta\dot{\rho} - \mathscr{L}\delta\rho = [f, \rho^{(0)}] + [f, \delta\rho] + [\delta h, \delta\rho] \tag{53}$$

where $\mathscr{L}$ is so-called Liouville matrix and is defined as

$$\mathscr{L}_{ij,mn} \equiv \delta_{j,n} h^{(0)}_{im} - \delta_{i,m} h^{(0)}_{jn} + 2\delta_{m,n}(v_{in} - v_{jn})\rho^{(0)}_{ij} - \delta_{i,m} v_{in}\rho^{(0)}_{jn} + \delta_{j,n} v_{jm}\rho^{(0)}_{im} \tag{54}$$

For the first-order induced density matrix $\delta\rho^{(1)}$, its dynamics may be described by the following equation

$$i\hbar\delta\dot{\rho}^{(1)} - \mathscr{L}\delta\rho^{(1)} = [f, \rho^{(0)}] \tag{55}$$

The key for the $O(N)$ scaling lies in the reduction of the sizes of $\delta\rho^{(1)}$ and $\mathscr{L}$. This reduction is a result of three approximations. First, $\delta\rho^{(1)}_{ij}$ is approximately zero when $r_{ij} > l_1$. This approximation leads to a band diagonal form of $\delta\rho^{(1)}$ which may be expressed as follows

$$\begin{pmatrix}
\delta\rho^{(1)}_{1,1} & \delta\rho^{(1)}_{1,2} & \cdots & \delta\rho^{(1)}_{1,\alpha_1+1} & 0 & 0 & \cdots & & 0 \\
\delta\rho^{(1)}_{2,1} & & & & \delta\rho^{(1)}_{2,\alpha_1+2} & 0 & \cdots & & 0 \\
\vdots & & \ddots & & & \ddots & \ddots & & \\
\delta\rho^{(1)}_{\alpha_1+1,1} & & & & & & & & \vdots \\
0 & \delta\rho^{(1)}_{\alpha_1+2,2} & & & & & & & \\
0 & 0 & \ddots & & & & & \ddots & \\
 & & \ddots & & & & & \ddots & 0 \\
\vdots & \vdots & & & & & & & \delta\rho^{(1)}_{N-\alpha_1,N} \\
 & & & & & \ddots & \ddots & & \vdots \\
0 & 0 & & \cdots & & & 0 & \delta\rho^{(1)}_{N,N-\alpha_1} \cdots & \delta\rho^{(1)}_{N,N}
\end{pmatrix} \tag{56}$$

where α_1 is the number of bonds within the critical length l_1. Only those elements $\delta\rho^{(1)}_{ij}$ within the diagonal band of $\delta\rho^{(1)}$ need to be considered explicitly. This leads to a reduction of the dimension of $\delta\rho^{(1)}$ or $\mathscr{L}$ from N^2 to $D_L \equiv (2\alpha_1 + 1)N - \alpha_1(\alpha_1 + 1)$. The resulting reduced first-order density matrix is denoted as $\delta\tilde{\rho}^{(1)}$, and its elements are arranged in the following increasing order : $\delta\rho^{(1)}_{1,1}, \delta\rho^{(1)}_{1,2}, \ldots, \delta\rho^{(1)}_{1,\alpha_1+1}, \delta\rho^{(1)}_{2,1}, \delta\rho^{(1)}_{2,2}, \ldots, \delta\rho^{(1)}_{2,\alpha_1+2}, \delta\rho^{(1)}_{3,1}, \ldots, \delta\rho^{(1)}_{N,N}$.

Second, $\rho^{(0)}_{ij}$ is set to zero for $r_{ij} > l_0$. (The resulting ground-state density matrix is denoted as $\tilde{\rho}^{(0)}$.) Consequently, $h^{(0)}_{ij}$ becomes zero for the same r_{ij}. Moreover, this leads to vanishing values of most first, second, fourth, and fifth terms on the right-hand side of Eq. (54).

The third term on the right-hand side of Eq. (54) contributes to $\delta\dot{\rho}_{ij}$ in Eq. (55) by

$$\sum_n 2(v_{in} - v_{jn})\rho^{(0)}_{ij}\delta\rho^{(1)}_{nn} \tag{57}$$

Because of the cancellations between v_{in} and v_{jn} (caused by the "nearsightedness" of $\rho^{(0)}$), and among different $\delta\rho^{(1)}_{nn}$, it is observed that the summation over n in Eq. (57) may be limited approximately between k_0 and k_1, where $k_0 = \max[1, \min(i - \alpha_c, j - \alpha_c)]$, $k_1 = \min[\max(i + \alpha_c, j + \alpha_c), N]$. Here α_c is a cutoff length for the summation in Eq. (57) and $\alpha_c \sim \alpha_1$ for the system. Therefore, only those third terms on the right-hand side of Eq. (54) whose m or n is between k_0 and k_1 are kept.

The combination of the second and third approximations result in zero values of most $\mathscr{L}_{ij,mn}$. With the particular ordering of $\delta\tilde{\rho}^{(1)}$, the resulting Liouville matrix, denoted as $\tilde{\mathscr{L}}$, has a band diagonal form as follows,

$$\begin{pmatrix}
L_{1,1} & L_{1,2} & \cdots & L_{1,\beta+1} & 0 & 0 & & \cdots & & 0 \\
L_{2,1} & & & & L_{2,\beta+2} & 0 & & \cdots & & 0 \\
\vdots & & \ddots & & & \ddots & \ddots & & & \\
L_{\beta+1,1} & & & & & & & & & \vdots \\
0 & L_{\beta_1+2,2} & & & & & & & & \\
0 & 0 & \ddots & & & & & & \ddots & \\
 & & \ddots & & & & & & \ddots & 0 \\
\vdots & \vdots & & & & & & & & L_{D_L-\beta,D_L} \\
 & & & & & \ddots & \ddots & & & \vdots \\
0 & 0 & & \cdots & & & 0 & L_{D_L,D_L-\beta} & \cdots & L_{D_L,D_L}
\end{pmatrix} \tag{58}$$

There are $(2\beta+1)D_L - \beta(\beta+1)$ elements within the diagonal band of $\tilde{\mathscr{L}}$, where $\beta = 2\alpha_1\alpha_c + \alpha_c$. Equation (55) thus becomes

$$i\hbar\delta\dot{\tilde{\rho}} - \tilde{\mathscr{L}}\delta\tilde{\rho}^{(1)} = [f, \tilde{\rho}^{(0)}] \tag{59}$$

Although it is not essential for the $O(N)$ scaling, the band diagonal form of $\tilde{\mathscr{L}}$ enables us to solve Eq. (59) in the frequency domain via a simple $O(N)$ scaling algorithm. A Gaussian elimination procedure is adopted with back substitution. The procedure consists of two processes: the forward process, which eliminates the lower half of $\tilde{\mathscr{L}}$, and the backward process, which evaluates each variable. Detailed analysis shows that the total number of algebraic operations is approximately

$$2(\beta+1)^2 D_L \tag{60}$$

In the calculation, α_1 is fixed. Because $D_L \sim O(N)$, the total computational time thus scales linearly with N. Further analysis demonstrates that the total memory needed for $\tilde{\mathscr{L}}$ is $(2\beta+1)D_L - \beta(\beta+1)$, and also scales as $O(N)$.

The accuracy of calculation is determined by the values of α_0, α_1, and α_c. For simplicity, $\alpha_0 = \alpha_1 = \alpha_c = \alpha$ is chosen in the calculation. Figure 7 shows the absorption spectra of polyacetylene, $C_{40}H_{42}$, and $C_{500}H_{502}$. The solid line represents the calculation of $C_{40}H_{42}$ with $\alpha = 20$, and the full TDHF calculation is represented by diamonds. The energy and intensity differences of the first peak between $\alpha = 20$ and the full TDHF are 0.33% and 0.08%, respectively. These calculations show that $\alpha_0 = \alpha_1 = \alpha_c = 20$ gives accurate results. The reduced density matrix corresponding to a particular excitation has its nearsightedness and critical length. The critical length does not alter with increasing N when N is much larger than the critical length. Thus, the same value of α_0, α_1, and α_c may be used for different N, provided that N is large enough. In the rest of the calculation, the same value of α_0, α_1, and α_c are adopted. The absorption spectrum for $C_{500}H_{502}$ (dashed line) is also determined. Its first peak red shifts and appears at $\omega = 2.03$ eV. This is consistent with the previous calculations [123].

In Fig. 8 the $O(N)$ scaling of computational time is examined and the CPU time versus N is plotted. The computational time spent in solving the HF ground state is negligible. The total CPU time is approximately the time needed for obtaining the excited state properties. Clearly, the CPU time scales linearly with N for N between 30 and 500. The linear scaling of computational time for the excited-state properties has been convincingly achieved.

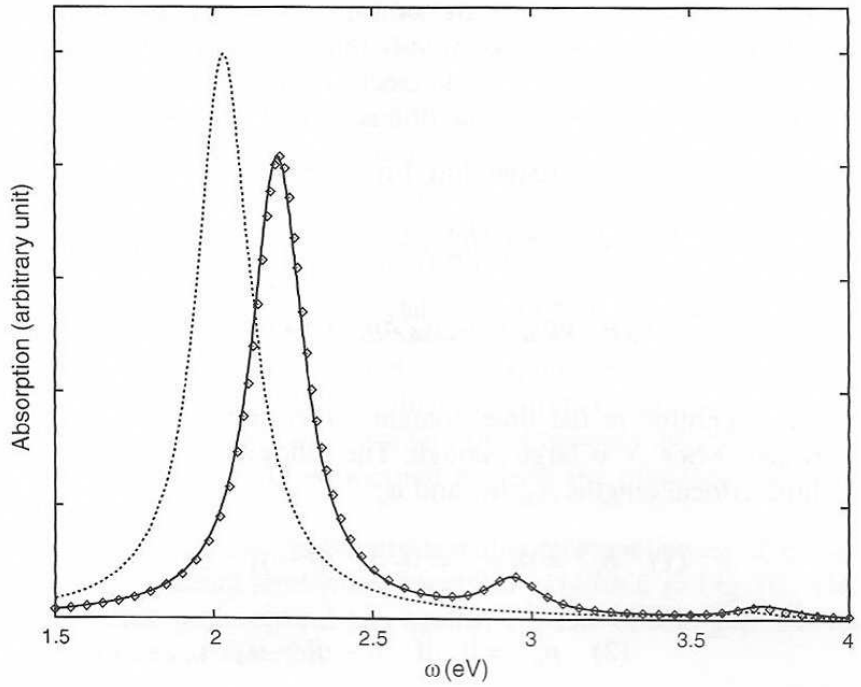

Figure 7. Absorption spectra of polyacetylene oligomers for $N = 40$ and 500. The solid line is for $N = 40$ and $\alpha = 20$, and the dashed line for $N = 500$ and $\alpha = 20$. The results of the full TDHF calculation for $N = 40$ are given by diamonds. The phenomenological dephasing constant $\Gamma = 0.1$ eV. For comparison, all data for $N = 40$ are multiplied by 12.5. Reprinted with permission from [59], S. Yokojima et al., *Phys. Rev. B* 59, 7259 (1999). © 1999, American Physical Society.

4.2.2. Time Domain Localized-Density-Matrix Method

In the previous section, the equation of motion for density matrix in the LDM method solved in the frequency domain is demonstrated. However, for the frequency domain LDM method, the linear scaling of computational time cannot be obtained for two- and three-dimensional systems. This obstacle can be removed if the equation of motion for the density matrix is solved in the time domain [58]. This leads to a great reduction of memory requirement and

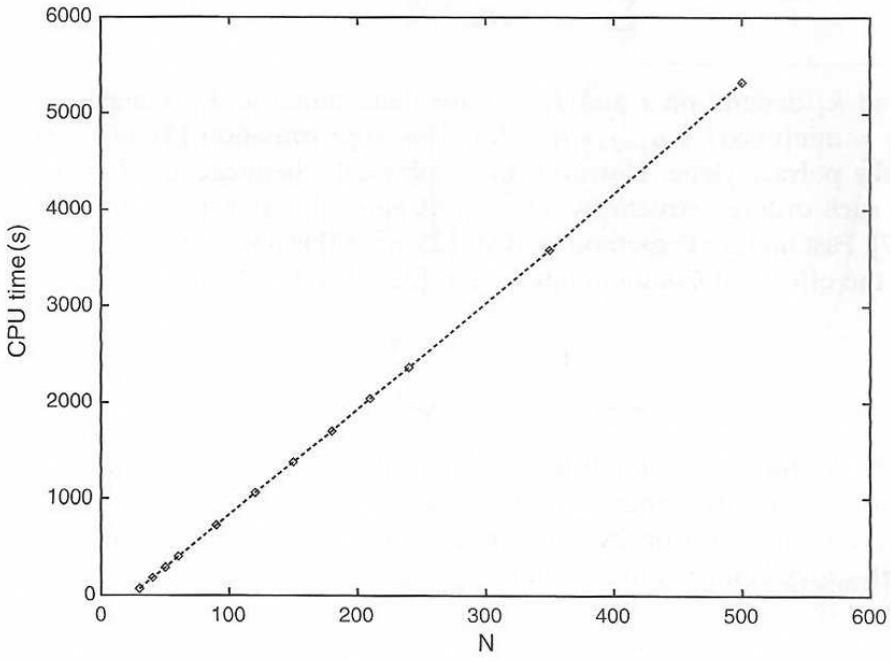

Figure 8. CPU time on an SGI Indigo2 R10000 workstation for $N = 30, 40, 50, 60, 90, 120, 150, 180, 210, 240, 350,$ and 500. Each calculation is performed at a frequency $\omega = 2.175$ eV with $\Gamma = 0.1$ eV; $\alpha = 20$ is used. Reprinted with permission from [59], S. Yokojima et al., *Phys. Rev. B* 59, 7259 (1999). © 1999, American Physical Society.

enables us to solve the excited-state properties of larger two- and three-dimensional systems. To solve the EOM in the time domain, we modify the frequency domain LDM method and follow the propagation of the reduced single-electron density matrix in the time domain. The modified method is referred as the time domain LDM method.

4.2.2.1. Semiempirical Method. Expanding Eq. (55), we have

$$i\hbar\delta\dot{\rho}_{ij}^{(1)} = \sum_k (h_{ik}^{(0)}\delta\rho_{kj}^{(1)} - \delta\rho_{ik}^{(1)}h_{kj}^{(0)}) + 2\sum_k (v_{ik} - v_{jk})\rho_{ij}^{(0)}\delta\rho_{kk}^{(1)} - \sum_k (v_{ik}\rho_{jk}^{(0)}\delta\rho_{ik}^{(1)} - v_{jk}\rho_{ik}^{(0)}\delta\rho_{kj}^{(1)}) + e(z(i) - z(j))\mathscr{E}(t)\rho_{ij}^{(0)} \tag{61}$$

Equation (61) is integrated in the time domain. Most matrix elements of $h^{(0)}$, $\rho^{(0)}$, and $\delta\rho^{(1)}$ are virtually zero when N is large enough. The following approximations is employed by introducing three critical lengths α_0, α_1, and α_c

$$(1) \quad h_{ij}^{(0)} = 0, \rho_{ij}^{(0)} = 0 \quad \text{if} \quad |i-j| > \alpha_0 \tag{62}$$

$$(2) \quad \rho_{ij}^{(1)} = 0 \quad \text{if} \quad |i-j| > \alpha_0 \tag{63}$$

and for the second term on the right-hand side of Eq. (61)

$$(3) v_{ij} = 0 \quad \text{if} \quad |i-j| > \alpha_c \tag{64}$$

The approximation (3) makes use of the cancellations among the second term of the right-hand side of Eq. (61). The cancellations ensure that $\delta\dot{\rho}_{ij}^{(1)}(t) \approx 0$ for $|i-j| > \alpha_1 (\alpha_1 \geq \alpha_c)$. Thus

$$i\hbar\delta\dot{\rho}_{ij}^{(1)} = \sum_k^{|i-k|\leq\alpha_0, |k-j|\leq\alpha_1} h_{ik}^{(0)}\delta\rho_{kj}^{(1)} - \sum_k^{|i-k|\leq\alpha_1, |k-j|\leq\alpha_0} \delta\rho_{ik}^{(1)}h_{kj}^{(0)} + 2\sum_k^{k_0\leq k\leq k_1} (v_{ik} - v_{jk})\rho_{ij}^{(0)}\delta\rho_{kk}^{(1)} - \sum_k^{|i-k|\leq\alpha_1, |k-j|\leq\alpha_0} v_{ik}\rho_{jk}^{(0)}\delta\rho_{ik}^{(1)} - \sum_k^{|i-k|\leq\alpha_0, |k-j|\leq\alpha_1} v_{jk}\rho_{ik}^{(0)}\delta\rho_{jk}^{(1)} + e(z(i) - z(j))\mathscr{E}(t)\rho_{ij}^{(0)} \tag{65}$$

where k_0 and k_1 depend on i and j, and are determined as $k_0 = \max[1, \min(i - \alpha_c, j - \alpha_c)]$ and $k_1 = \min[\max(i + \alpha_c, j + \alpha_c), N]$. This approximation (3) works well in ordered molecules like polyacetylene. However, many physical, chemical, and biological systems do not possess such ordered structures. The cutoff approximation may thus lead to numerical error [86, 87]. Fast multipole method (FMM) [25, 85–88] is implemented in the LDM method to evaluate the effects of Coulomb interaction [62]. The Coulomb energy is represented by

$$V = \frac{1}{2}\sum_{i\neq j} \frac{q_i q_j}{\sqrt{a_0^2 + r_{ij}^2}} \tag{66}$$

The FMM divides the system into boxes of different sizes and replaces the pairwise Coulomb interaction with multipolar expansions. This leads to the $O(N)$ scaling of the computational time and, thus, reduces drastically the computational time for large systems.

The fourth-order Runge-Kutta method [74] is used to integrate Eq. (65). The external field employed is

$$\mathscr{E}(t) = \frac{1}{\sqrt{\pi}\bar{t}} e^{-(t/\bar{t})^2} \tag{67}$$

where $\bar{t} = 0.1$ fs. The phenomenological dephasing constant is set to 0.1 eV.

The LDM ground-state method [126] has been used for the ground-state calculation of polyacetylene oligomers. Figure 9a shows the computational time for the ground-state calculation. To verify that the computational time of excited-state calculation scales linearly with the system size N, Eq. (61) is propagated between a time interval [−0.5 fs, −0.3 fs] with a time step of 0.01 fs. The resulting computational time versus N is plotted in Fig. 9b. Clearly, the CPU time is proportional to the system size N. The resulting $\delta\rho^{(1)}(t)$ may be used to obtain the absorption spectrum for each N by Fourier transform.

The full TDHF, the FMM-LDM, and the cutoff-LDM methods for $N = 200$ are compared, and $l_0 = l_1 = 50$ Å is employed in both LDM calculations. A four level hierarchy is used in the FMM calculation. The results are shown in Fig. 9c. Clearly, three sets of results are consistent for $\omega > 0.8$ eV. When $\omega < 0.8$ eV, as shown in the inset of Fig. 9c, the FMM-LDM method yields much better results than the cutoff-LDM method with $l_c = 25$ Å. This is because the FMM-LDM method considers the Coulomb interaction in all the space of the system, whereas the cutoff-LDM method neglects the influences of the charges outside the cutoff region.

The absorption spectrum of a polyacetylene oligomer containing 10,000 carbon atoms is also calculated. The resulting absorption spectrum is plotted in Fig. 9d. The optical gap is 2.08 eV. The inset shows the optical gap against N. The optical gap reduces drastically as N increases. It saturates at $N \approx 200$.

4.2.2.2. Time-Dependent Density-Functional Theory. Yam et al. combine the LDM method and TDDFT (TDDFT-LDM) [127, 128]. For linear scaling in Gaussian-based DFT calculations, there are three important bottlenecks. These are the calculation of two-electron

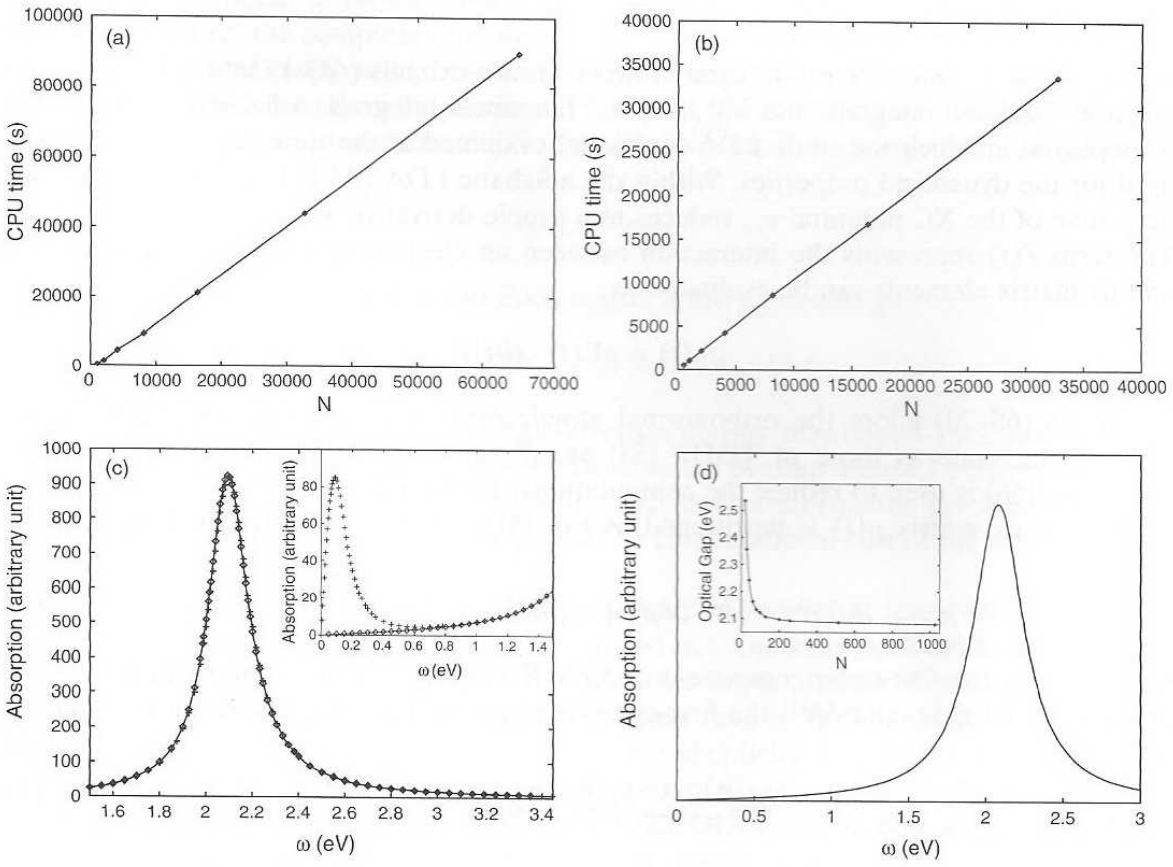

Figure 9. (a) The CPU time versus N for the calculation of ground states reduced density matrices ($l_1 = 50$ Å and 16 atoms in the smallest box). (b) The CPU time for the calculation of excited state ($l_1 = l_0 = 37$ Å and 16 atoms in the smallest box). Each calculation is performed during a time interval [−0.5 fs ,−0.3 fs] with a time step 0.01 fs. (c) The absorption spectrum for $N = 200$. The crosses are the cutoff-LDM results with $l_1 = l_0 = 50$ Å and $l_c = 25$ Å. The diamonds are the FMM-LDM results with $l_1 = l_0 = 50$ Å and 25 atoms in smallest box. The solid lines are the full TDHF results. Each calculation is performed during the time interval between −0.5 fs and 70.0 fs with a time step 0.01 fs; $\gamma = 0.1$ eV. (d) The absorption spectra for $N = 10{,}000$ by using the FMM-LDM method with $l_1 = l_0 = 50$ Å. Eight-level FMM is employed. The dephasing parameter $\gamma = 0.2$ eV. Reprinted with permission from [62], W. Z. Liang et al., *J. Phys. Chem. A* 104, 2445 (2000). © 2000, American Chemical Society.

Coulomb integrals and XC quadratures, and the Hamiltonian diagonalization. The FMM [25, 85–88], which was originally developed to evaluate the Coulomb interactions of point charges, led to the linear-scaling computation of the two-electron Coulomb integrals. Linear-scaling evaluation of the XC quadratures was also achieved by exploiting the localized nature of XC potential and by employing the integral prescreening technique [91, 92]. The Hamiltonian diagonalization is intrinsically $O(N^3)$, and most $O(N)$ algorithms make use of the locality or "nearsightedness" of reduced single-electron density matrix ρ [5, 6, 10, 129].

The remaining obstacle for linear-scaling TDDFT method lies in solving the TDDFT equation. The TDDFT equation is very similar to the TDHF equation. The LDM method was developed to solve the TDHF equation, and its computational time scales linearly with the system size [58, 59]. Instead of the many-body wave function, the LDM method solves for ρ of a molecular system from which its electronic excited-state properties are evaluated. The EOM of ρ is integrated in the time domain. The linear scaling of computational time versus the system size is ensured by the introduction of density matrix ρ cutoffs [58, 59, 64]. Because TDDFT and TDHF have similar EOMs for ρ, the TDDFT and LDM methods are combined just as TDHF-LDM method [58, 59]. The resulting TDDFT-LDM method shall thus be a linear-scaling method for electronic excited states.

Within the TDDFT, the EOM of reduced single-electron density matrix $\rho(t)$ is

$$i\hbar\dot{\rho}(t) = [h(t) + f(t), \rho(t)] \tag{68}$$

Here $h(t)$ is the Fock matrix

$$h_{ij}(t) = t_{ij} + \sum_{mn} \rho_{mn}(t)(V_{ijmn} + V^{xc}_{ijmn}) \tag{69}$$

with t_{ij} being the one-electron integral between atomic orbitals (AOs) i and j, V_{ijmn} the two-electron Coulomb integrals, and V^{xc}_{ijmn} the XC functional integrals. Adiabatic approximation is employed in which the static LDA functional evaluated at the time-dependent density is used for the dynamical properties. Within the adiabatic LDA (ALDA) [130], the functional derivative of the XC potential v_{xc} reduces to a simple derivative with respect to the density. The term $f(t)$ represents the interaction between an electron and the external field $\mathbf{E}(t)$, and its matrix elements can be evaluated as

$$f_{ij}(t) = e\mathbf{E}(t) \cdot \langle i|\hat{\mathbf{r}}|j\rangle \tag{70}$$

Equations (68–70) adopt the orthonormal atomic orbitals as the basis functions and are virtually the same as those of TDHF [58] except the V^{xc}_{ijmn} term. Thus, the same LDM procedure [58] is used to reduce the computational time for Eqs. (68–70).

The density matrix $\rho(t)$ is partitioned as Eq. (51). To the first order in $\mathbf{E}(t)$, Eq. (68) becomes

$$i\hbar\delta\dot{\rho}^{(1)} = [h^{(0)}, \delta\rho^{(1)}] + [\delta h^{(1)}, \rho^{(0)}] + [f, \rho^{(0)}] \tag{71}$$

where $\delta\rho^{(1)}$ is the first-order component of $\delta\rho$ in $\mathbf{E}(t)$, $h^{(0)}$ is the Fock matrix in the absence of the external field, and $\delta h^{(1)}$ the first-order induced Fock matrix, which can be evaluated as

$$\delta h^{(1)}_{ij} = \sum_{mn} \delta\rho^{(1)}_{mn}(V_{ijmn} + V^{xc}_{ijmn}) \tag{72}$$

Equation (71) is integrated numerically in the time domain and is solved for the time evolution of the polarization vector $\mathbf{P}(t)$. Specifically, Eq. (71) can be rewritten as

$$i\hbar\delta\dot{\rho}^{(1)}_{ij} = \sum_k (h^{(0)}_{ik}\delta\rho^{(1)}_{kj} - \delta\rho^{(1)}_{ik}h^{(0)}_{kj}) + \sum_k (\delta h^{(1)}_{ik}\rho^{(0)}_{kj} - \rho^{(0)}_{ik}\delta h^{(1)}_{kj}) + \sum_k (f_{ik}\rho^{(0)}_{kj} - \rho^{(0)}_{ik}f_{kj}) \tag{73}$$

Solving Eq. (73) alone does not lead to the linear scaling of computational time, because the matrix multiplication involved is intrinsically $O(N^3)$. The key for the $O(N)$ scaling lies in the reduction of reduced single-electron density matrix elements by introduction of ρ

cutoffs. The cutoffs are based on the locality or nearsightedness of ρ [64]. Specifically, $\rho_{ij}^{(0)}$ is set to zero for $r_{ij} > l_0$ (consequently, $h^{(0)}$ becomes zero for $r_{ij} > l_0$); and $\delta\rho_{ij}^{(1)}$ is set to zero when $r_{ij} > l_1$, which leads to a reduction of the dimension of $\delta\rho^{(1)}$ from $O(N^2)$ to $O(N)$.

For a fixed pair of i and j, the summations over k in Eq. (73) is finite and independent of N. However, the second term on the right-hand side of Eq. (73) can be expanded as

$$\sum_k \sum_m \sum_n (\delta\rho_{mn}^{(1)} V_{ikmn} \rho_{kj}^{(0)} - \rho_{ik}^{(0)} \delta\rho_{mn}^{(1)} V_{kjmn}) + \sum_k \sum_m \sum_n (\delta\rho_{mn}^{(1)} V_{ikmn}^{xc} \rho_{kj}^{(0)} - \rho_{ik}^{(0)} \delta\rho_{mn}^{(1)} V_{kjmn}^{xc}) \quad (74)$$

The first term in Eq. (74) is from long-range Coulomb interaction between the induced charge distribution and the ground-state charge distribution. The summation over m and n is of $O(N)$, which leads to overall $O(N^2)$ scaling for the direct computation of the second term on the right-hand side of Eq. (73). To achieve $O(N)$ computation, the FMM is employed to evaluate $\sum_m \sum_n \delta\rho_{mn}^{(1)} V_{ikmn}$ and $\sum_m \sum_n \delta\rho_{mn}^{(1)} V_{kjmn}$. The FMM leads to overall finite number of floating point calculations for the first term in Eq. (74). For the second term in Eq. (74), we resort to numerical quadrature [91, 131] to calculate it because an analytical solution cannot be obtained. To achieve linear scaling, the localized nature of the XC potential is exploited and confines its contributions at a given grid point to a relatively small region around it, with negligible loss of accuracy. Taking advantage of the fast-decaying nature of Gaussian basis functions, integrals are discarded when the absolute differential overlap between any two orbitals is less than 10^{-8}.

With the above techniques, the number of summations over m and n in Eq. (73) is restricted to finite range, which does not depend on the value of N. Because the number of $\delta\rho_{ij}^{(1)}$ is proportional to N, the total number of floating-point calculations scales linearly with N. Therefore, the computational time is expected to be proportional to N.

Because the LDM employs an orthonormal atomic basis set, the Gaussian basis set 6-31G that is employed needs to be orthogonalized. Yam et al. use the Cholesky decomposition [74] of the overlap matrix S to transform the Gaussian basis set to the corresponding orthonormal basis set

$$S = U^T U \quad (75)$$

The transformed density matrix ρ and Fock matrix h are expressed as

$$\rho = U \rho_{\mathrm{AO}} U^T; \qquad h = U^{-T} h_{\mathrm{AO}} U^{-1} \quad (76)$$

where ρ_{AO} and h_{AO} are the reduced single-electron density matrix and Fock matrix in the original atomic orbital basis set, respectively. Because the overlap matrix S between Gaussian AOs becomes sparser with increasing molecular size, the transformation involves only multiplication of sparse matrices, which ensures that the computational cost of the transformation goes up linearly with the system size [129].

To demonstrate that the TDLDA-LDM method is indeed a linear-scaling method, calculations on a series of linear alkanes are carried out. Gaussian basis set 6-31G has been used. The electric field $\mathscr{E}(t)$ is applied parallel to the linear alkanes. The time step of the simulation is set to 0.005 fs, and the total simulation time is 70 fs. The accuracy of calculation is determined by the values of l_0 and l_1. For simplicity, $l_0 = l_1 = l$ is chosen in the calculation. Figure 10 shows the absorption spectrum of $C_{40}H_{82}$, using $l = 25$ Å. To examine the accuracy of the calculation, we perform a full TDDFT calculation with no cutoff for the same molecule. The dashed line represents the results of the full TDLDA calculation. The agreement between the results of two TDLDA calculations are excellent. This value $l = 25$ Å will be employed in the calculation of larger alkanes. In Fig. 11, the absorption spectrum of $C_{60}H_{122}$ is plotted. In Figs. 10 and 11, absorptions start at about 8 eV for both molecules. This is consistent with the observed σ to σ^* transition at about a 150-nm wavelength in alkanes [132]. The absorption spectrum of $C_{40}H_{82}$ and $C_{60}H_{122}$ are similar overall, except for the slight difference between 11 and 13 eV.

To examine whether the TDLDA-LDM method is indeed a linear-scaling method, Yam et al. performed the TDLDA-LDM calculates on a series of linear alkanes, with the number

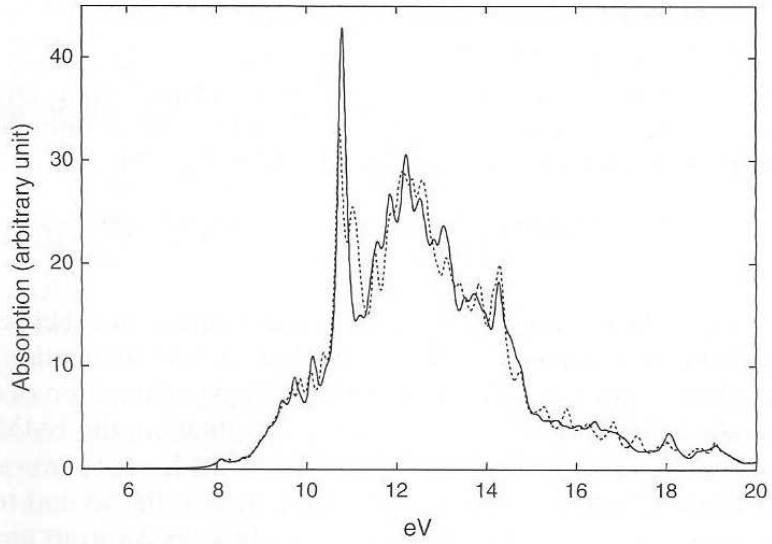

Figure 10. Absorption spectra for $C_{40}H_{82}$. The solid line is for $C_{40}H_{82}$ and $l = 25$ Å, and the dashed line for the full TDDFT calculation where no cutoffs are introduced. The phenomenological dephasing constant $\Gamma = 0.1$ eV. Reprinted with permission from [127], C. Y. Yam et al., *Phys. Rev. B* 68, 153105 (2003). © 2003, American Physical Society.

of atoms ranging from 62 to 602. To save computational time, the simulation was limited to 1 fs interval. The CPU time of each calculation was recorded. The computational time spent in solving the DFT ground state was negligible. In Fig. 12, the CPU time versus number of atoms N_A is plotted. Clearly the CPU time scales linearly with N_A for N_A between 62 and 602. The linear scaling of computational time versus the system size has been convincingly achieved. The CPU time of Cholesky transformation versus the system size is examined. Figure 13 shows that the computational time of Cholesky transformation scales linearly with the molecular size.

4.3. Further Development of LDM Method

4.3.1. Combined Dynamics of Electrons and Nuclei

Traditionally the dynamics of electrons and nuclei in molecular systems is treated within the Born–Oppenheimer (BO) or the adiabatic approximation in which the timescale of nuclear motion is assumed to be much longer than that of the electron motion. The nuclear motion is

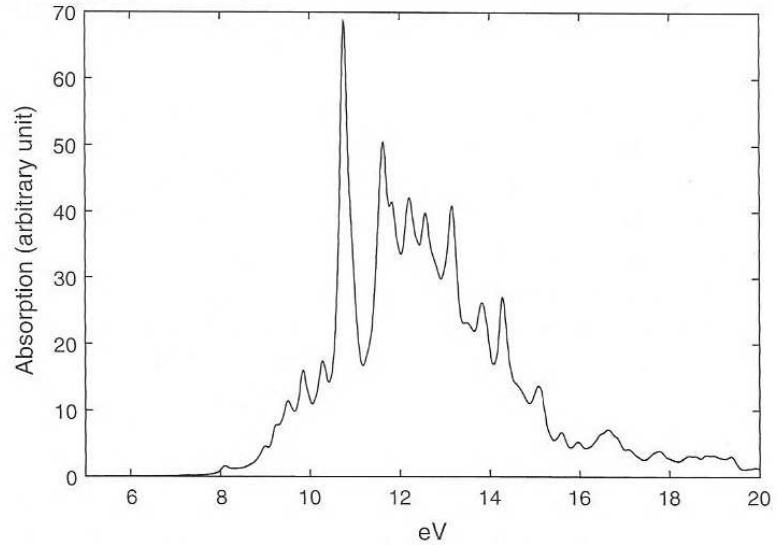

Figure 11. Absorption spectra for $C_{60}H_{122}$ using $l_0 = l_1 = 25$ Å. The phenomenological dephasing constant $\Gamma = 0.1$ eV. Reprinted with permission from [127], C. Y. Yam et al., *Phys. Rev. B* 68, 153105 (2003). © 2003, American Physical Society.

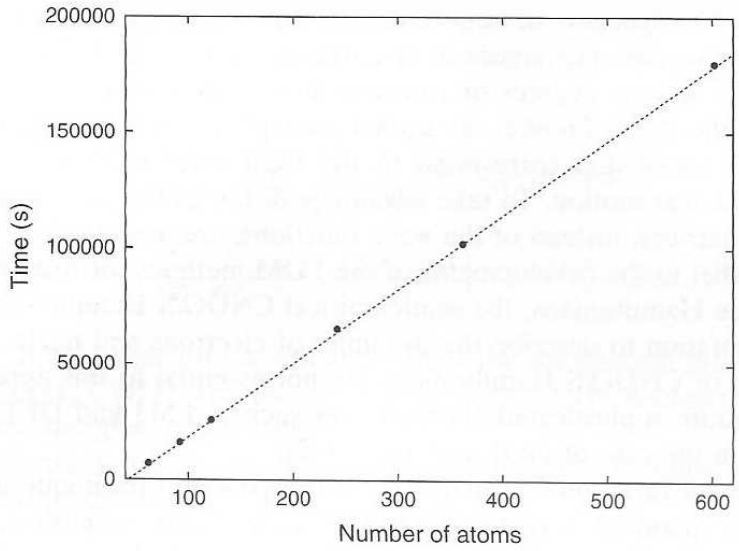

Figure 12. CPU time for alkanes with N_A=62, 92, 122, 242, 362, and 602. Each calculation is performed during the time interval between −0.5 fs and 0.5 fs with time step 0.005 fs. The term l = 25 Å is used. Reprinted with permission from [127], C. Y. Yam et al., *Phys. Rev. B* 68, 153105 (2003). © 2003, American Physical Society.

often computed with potential energy surfaces (PES) or force fields that are often obtained from *ab initio* calculations. Numerical simulations beyond the BO approximation are limited to small systems because of the requirement of expensive computational resources for the electronic degrees of freedom. The electron–nuclear dynamics (END) method has been applied to diatomic or triatomic molecules [133–136]. The electronic and nuclear wave functions are approximated by the single Slater determinants and fixed-width Gaussian wave functions, respectively. Other important contributions to the nonadiabatic dynamics include the surface-hopping approaches by Tully et al. [137], which serve as an alternative to methods of a single average nuclear path. Also proposed were semiclassical treatments of curve crossings in reaction dynamics by Miller et al. [138] and applications of similar nature to the spin-boson problem and internal conversion processes by Stock [139].

Chen and coworkers developed a method for treating the electrons and nuclei simultaneously without assuming different timescales for electrons and nuclei or the BO approximation, and thus do not have to resort to the PES or force field in the calculation of nuclear dynamics. Because the electronic degrees of freedom may be handled efficiently with the LDM method, it is expected that the new method may ultimately be used to simulate the

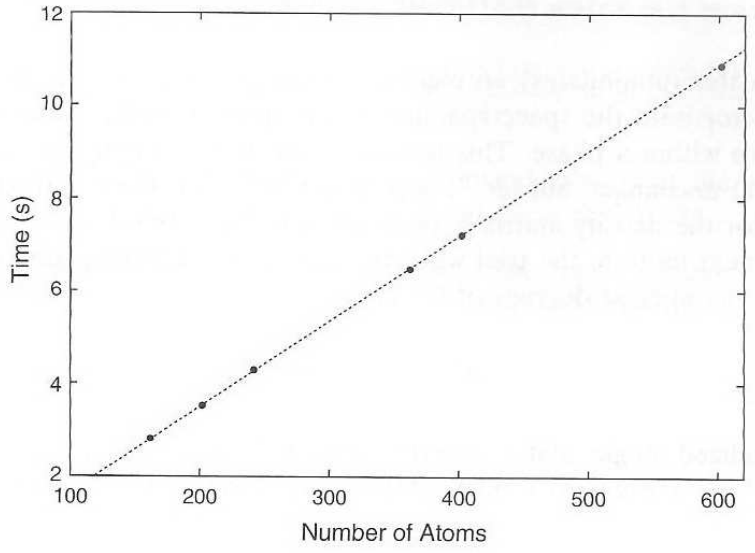

Figure 13. CPU time for Cholesky transformation. Reprinted with permission from [128], C. Y. Yam et al., *J. Chem. Phys.* 119, 8794 (2003). © 2003, American Institute of Physics.

electronic and nuclear dynamics of large, complex molecular systems. A variational approach is adopted for the combined dynamics of electrons and nuclei. The equations of motion for the electronic and nuclear degrees of freedom may be derived rigorously from the exact Lagrangian using the Dirac–Frenkel variational principle [140]. Similar to the END method, Glauber coherent states that correspond to the fixed-width Gaussians in real space are adopted for the nuclear motion. To take advantage of the LDM treatment of electrons, the reduced-density matrices, instead of the wave functions, are used to describe the electronic dynamics. In parallel to the developments of the LDM methods for fixed nuclei that started from rather simple Hamiltonians, the semiempirical CNDO/S Hamiltonian [141] is used as the first implementation to describe the dynamics of electrons and nuclei. It is emphasized that the adoption of CNDO/S Hamiltonians are not essential to this approach, and extensions to include more sophisticated Hamiltonians such as PM3 and DFT [2] can easily be implemented, as in the case of fixed nuclei [60, 142].

The Dirac–Frenkel variational principle [140] is a powerful technique to obtain approximate dynamics for quantum systems for which exact solutions are elusive. The formulation starts with the exact Lagrangian

$$L = \left\langle \phi^T(t) \middle| \frac{i\hbar}{2} \frac{\overleftrightarrow{\partial}}{\partial t} - \widehat{H} \middle| \phi^T(t) \right\rangle \tag{77}$$

where $\phi^T(t)$ is an ansatz for the full normalized wave function of a quantum system, which hinges on parameters η_m $(m = 1, 2, 3, ...)$. Here η_m can be complex c-numbers or trial wave functions of subsystems. In general, the Dirac–Frenkel variational principle [140] leads to

$$\frac{d}{dt}\left(\frac{\partial L}{\partial \dot{\eta}_m^\dagger}\right) - \frac{\partial L}{\partial \eta_m^\dagger} = 0 \tag{78}$$

where $\eta_m^\dagger$ stands for the complex conjugate of η_m.

Following, we show how to apply the Dirac–Frenkel variational principle to obtain a single-determinant ansatz and its multiconfiguration generalization.

4.3.1.1. Single-Configuration Ansatz. The TDHF equation for fixed nuclei can be derived from the Dirac–Frenkel variational principle [140]. The trial wave function $|\phi^{HF}\rangle$ for an electronic system is a single Slater determinant composed of N single-particle orbitals. One associates a single-particle density matrix $\rho_{ij}(t)$ with $|\phi^{HF}\rangle$

$$\rho_{ij}(t) = \langle \phi^{HF} | a_j^\dagger a_i | \phi^{HF} \rangle \tag{79}$$

where $a_j^\dagger$ (a_i) creates (annihilates) an electron at the jth $(i$th) orbital. The density matrix $\rho_{ij}(t)$, as a projector onto the space spanned by occupied orbitals, characterizes the Slater determinant up to within a phase. This is easily seen by exchanging two orbitals in $|\phi^{HF}\rangle$, which leaves $\rho_{ij}(t)$ unchanged but $|\phi^{HF}\rangle$ with a negative sign. Brief derivation of the equations of motion for the density matrix $\rho_{ij}(t)$ is given in Ref. [143].

To include nuclear motion, the trial wave function in the TDHF approximation is generalized to include the nuclear degrees of freedom

$$|\phi^T\rangle = |\phi^{HF}\rangle |\phi^N\rangle \tag{80}$$

where the normalized single Slater determinant $|\phi^{HF}\rangle$ is composed of N single-particle orbitals ϕ_i, and $|\phi^N\rangle$ represents a normalized nuclear wave function. The Lagrangian has the form

$$L = \frac{i\hbar}{2} \sum_i (\langle \phi_i | \dot{\phi}_i \rangle - \langle \dot{\phi}_i | \phi_i \rangle) + \frac{i\hbar}{2} (\langle \phi^N | \dot{\phi^N} \rangle - \langle \dot{\phi^N} | \phi^N \rangle) - \langle \phi^T | \widehat{H} | \phi^T \rangle \tag{81}$$

Consider a system with M nuclei and N electrons. The nuclear and electronic coordinates are labeled as $\mathbf{r}_n$ $(n = 1, \ldots, M)$ and $\mathbf{r}_i^e$ $(i = 1, \ldots, N)$, respectively. The energy expression takes the form

$$E \equiv \langle \phi^T | \widehat{H} | \phi^T \rangle = \left\langle \phi^N \right| - \sum_n \frac{\hbar^2}{2M_n} \frac{\partial^2}{\partial \mathbf{r_n}^2} + V_{NN}(\{\mathbf{r}_n\}) | \phi^N \Big\rangle$$
$$+ \left\langle \phi^T \right| - \sum_i \frac{\hbar^2}{2m_i} \frac{\partial^2}{\partial \mathbf{r}_i^{e2}} + V_{ee}(\{\mathbf{r}_i^e\}) | \phi^T \Big\rangle + \langle \phi^T | V_{eN}(\{\mathbf{r}_n\}, \{\mathbf{r}_i^e\}) | \phi^T \rangle \tag{82}$$

where M_n are the atomic mass for the nth atom, m_i is the ith electron mass, and $V_{NN}(\{\mathbf{r}_n\})$, $V_{ee}(\{\mathbf{r}_i^e\})$, and $V_{eN}(\{\mathbf{r}_n\}, \{\mathbf{r}_i^e\})$ are the nucleus–nucleus, electron–electron, and nucleus–electron interaction energies, respectively.

Following, we discuss separately the electronic and nuclear equations of motion derived from the variational procedure.

4.3.1.2. Electronic Equations of Motion. Applying the time-dependent variational approach

$$\frac{d}{dt}\left(\frac{\partial L}{\partial \langle \dot{\phi}_i |}\right) - \frac{\partial L}{\partial \langle \phi_i |} = 0 \tag{83}$$

we obtain the equations for the electronic degrees of freedom

$$i\hbar \dot{\rho} = [h', \rho] \tag{84}$$

where the Fock matrix h' is given by

$$h' | \phi_i \rangle = \frac{\partial E}{\partial \langle \phi_i |} \tag{85}$$

The difference between h' and the usual Fock matrix h (cf. Ref. [143]) lies only in that h', being dependent on

$$\langle \phi^{HF} | V_{ee}(\{\mathbf{r}_i^e\}) + V_{eN}(\{\mathbf{r}_n\}, \{\mathbf{r}_i^e\}) | \phi^{HF} \rangle \tag{86}$$

changes with time as the nuclei move. In other words, quantities such as v_{ij} in Eq. (85) are now time dependent in h', as compared with h. So far, basis orbitals have not been specified. Orbitals fixed in space are not suitable to describe dynamical chemical systems, which may require a large number of basis functions. One needs to consider basis orbitals $\{\phi_i(t)\}$ that move with the nuclei. Equations of motion for the density matrix in a moving basis are

$$\dot{\rho}_{ij} = (i\hbar)^{-1} \langle \phi_i(t) | [h', \rho] | \phi_j(t) \rangle - \rho_{ij} \left\langle \phi_i(t) \right| \frac{\partial | \phi_i(t) \rangle}{\partial \mathbf{r}_i} \mathbf{V}_i - \rho_{ij} \frac{\partial \langle \phi_j(t) |}{\partial \mathbf{r}_j} \mathbf{V}_j | \phi_j(t) \Big\rangle \tag{87}$$

where $\mathbf{r}_i$ and $\mathbf{V}_i$ are, respectively, the position vector and velocity of the nucleus on which the ith orbital resides. The details of derivation are given in Ref. [143].

4.3.1.3. Nuclear Dynamics as Coherent States. The nuclear degrees of the freedom are treated within the same variational framework. For example, the formal equation of motion for $|\phi^N\rangle$ is derived from

$$\frac{d}{dt}\left(\frac{\partial L}{\partial \langle \dot{\phi^N} |}\right) - \frac{\partial L}{\partial \langle \phi^N |} = 0 \tag{88}$$

From the energy expression of Eq. (82), one readily arrives at

$$i\hbar | \dot{\phi}^N \rangle = \left[- \sum_n \frac{\hbar^2}{2M_n} \frac{\partial^2}{\partial \mathbf{r}_n^2} + V_{NN}(\{\mathbf{r}_n\}) + \langle \phi^{HF} | V_{ee}(\{\mathbf{r}_i^e\}) + V_{eN}(\{\mathbf{r}_n\}, \{\mathbf{r}_i^e\}) | \phi^{HF} \rangle \right] | \phi^N \Big\rangle \tag{89}$$

$\langle\phi^{HF}|V_{ee}(\{\mathbf{r}_i^e\})|\phi^{HF}\rangle$ is dependent on $\{\mathbf{r}_n\}$ in many approximation schemes, and it thus can not be neglected in Eq. (89). To capture fully the time evolution of nuclear motion, some detailed form of $|\phi^N\rangle$ has to be specified and corresponding equations of motion derived.

For the nuclear wave function, a convenient ansatz to use is the Glauber coherent state [144]. The coherent states are equivalent to the so-called frozen Gaussian wave packets [145] in the real-space representation. Frozen Gaussian wave packets are robust in time evolution. In contrast, Gaussian wave packets with variant widths are often found to be problematic [146, 147]. The coherent state is regarded as a quantum mechanical state that approaches a classical state when the width goes to zero [144, 148–150]. In fact, in a harmonic potential, the coherent state undergoes the same dynamics using classical mechanics as when using QM. As $\hbar$ tends to zero, the width of the coherent state vanishes and the nuclei are reduced to classical particles localized in the phase space. This makes the coherent states especially suitable for modeling quasi-classical systems.

Chen and coworkers approximate the nuclear wave function $|\phi^N\rangle$ with a coherent state

$$|\phi^N\rangle = |\alpha(t)\rangle = \prod_{i=1}^{3N} |\alpha_i(t)\rangle \tag{90}$$

where α_i $(i = 1, ..., 3N)$ are complex parameters that characterize the motion of N nuclei along x, y, and z directions and the coherent state $|\alpha_i(t)\rangle$ may be expressed in the site representation as

$$\langle x|\alpha_i(t)\rangle = \pi^{-1/4} \exp\left\{ -\frac{1}{2}\left[\sqrt{\frac{M_i\omega_i}{\hbar}}x - \sqrt{2}\Re(\alpha_i(t))\right]^2 + i\Im(\alpha_i(t))\left[\sqrt{\frac{2M_i\omega_i}{\hbar}}x - \Re(\alpha_i(t))\right]\right\} \tag{91}$$

where ω_i is the characteristic frequency for ith degree of freedom, which determines the width of the Gaussian wave packet.

The Lagrangian takes the form

$$L = \frac{i\hbar}{2}(\langle\phi^N|\dot{\phi}^N\rangle - \langle\dot{\phi}^N|\phi^N\rangle) - E' = \frac{i\hbar}{2}\sum_{i=1}^{3N}(\dot{\alpha}_i\alpha_i^* - \dot{\alpha}_i^*\alpha_i) - E' \tag{92}$$

with

$$E' = \left\langle\alpha\right| - \sum_n \frac{\hbar^2}{2M_n}\frac{\partial}{\partial\mathbf{r}_n^2} + V_{NN}\left|\alpha\right\rangle + \langle\alpha|\langle\phi^{HF}|V_{ee} + V_{eN}|\phi^{HF}\rangle|\alpha\rangle \tag{93}$$

This follows from

$$\langle\alpha_i|\dot{\alpha}_i\rangle = -\frac{1}{2}\frac{d}{dt}(\alpha_i\alpha_i^*) + \langle\alpha_i|e^{-1/2|\alpha_i|^2}\dot{\alpha}_i b_i^\dagger e^{\alpha_i b_i^\dagger}|0\rangle = -\frac{1}{2}\frac{d}{dt}|\alpha_i|^2 + \dot{\alpha}_i\alpha_i^* \tag{94}$$

where $b_i^\dagger$ (b_i) is the creation (annihilation) operator for ith degree of freedom and is defined as

$$b_i^\dagger = \sqrt{\frac{M_i\omega}{2\hbar}}q_i + \sqrt{\frac{\hbar}{2M_i\omega}}\frac{\partial}{\partial q_i} \tag{95}$$

$$b_i = \sqrt{\frac{M_i\omega}{2\hbar}}q_i - \sqrt{\frac{\hbar}{2M_i\omega}}\frac{\partial}{\partial q_i} \tag{96}$$

Equations of motion for the complex displacement α_i then assume the simple form

$$i\hbar\dot{\alpha}_i = \frac{\partial E'}{\partial\alpha_i^*} \tag{97}$$

Here α_i is related to the average nuclear position $\langle q_i \rangle_t$ and momentum $\langle p_i \rangle_t$ for the ith nuclear degree of freedom by

$$\alpha_i = \sqrt{\frac{M_i \omega_i}{2\hbar}} \langle q_i \rangle_t + i \sqrt{\frac{1}{2\hbar M_i \omega_i}} \langle p_i \rangle_t \tag{98}$$

with M_i being the corresponding mass.

There can be many generalizations for the ansatz of a single coherent state for the nuclear dynamics. One generalization is a superposition of many coherent states, which better captures the quantum nature of the nuclear motion [151]. When the corresponding electronic state is multiconfigurational, such a generalization becomes absolutely necessary.

The force acting on the nucleus of the nth atom can be calculated from

$$\mathbf{F}_n = -\nabla_n (E^{\text{tot}} + V_{NN}) \tag{99}$$

To simplify the simulation

$$\frac{\partial \rho}{\partial \mathbf{r}_n} \approx 0 \tag{100}$$

is set. Thus

$$\mathbf{F}_n = -\nabla_n \sum_{m}^{m \neq n} E_{nm} - \nabla_n V_{NN} \tag{101}$$

where ∇_n stands for the derivative with respect to the position vector $\mathbf{r}_n$ of nth nucleus. The reader is referred to Ref. [143] for details of the nuclear-force evaluation.

4.3.2. Dynamic Mean Field Theory for Dissipative Interacting Many-Electron Systems

Quantum dissipation is a subject of widespread interest in many fields of physics, chemistry, and materials science. Various quantum dissipation theories (QDTs) have been developed to investigate the dynamic properties of open systems. They include the Bloch–Redfield theory [152–158], Fokker–Planck equations [158–165], and semigroup formalism [166–169]. Most recently, a complete second-order QDT (CS-QDT) was constructed [170] in which the system-bath interaction was treated rigorously at the second-order cumulant level for both the initial canonical thermal equilibrium and the reduced dynamics. The key physical quantity in these QDTs is the reduced-density operator ρ, whose dynamics is described by the Liouville–von Neumann equation of motion, where dissipation is treated with different forms for different QDTs [152–178]. Because the system reduced-density matrix needs to be solved, the computational costs of the above methods are expensive, and the calculations have thus been limited to low-dimensional systems. Building on the initial work by Yan, Chen, Yokojima, and coworkers [179], Yokojima, Chen, Xu, and Yan [180, 181] developed a QDT based on the EOM for the reduced single-electron density matrix. The resulting EOM was employed to simulate the excitation and nonradiative relaxation of a butadiene molecule. This reduced single-electron density matrix–based QDT opens the possibility for quantum chemistry calculations of large quantum open systems. The new formalism is based on the EOM for the reduced single-electron density matrix. The theoretical development starts with the second quantization of the CS-QDT proposed by Xu and Yan [170], followed by a random phase approximation (RPA) or TDHF treatment on electron–electron correlations. The thermal bath can be the nuclei of system or the environment. The traditional linear dissipation superoperator in conventional QDTs is now replaced by nonlinear quantum nonradiative dissipation terms. These terms include the electron–nuclei couplings and energy or material exchanges with the environment. Because only the reduced single-electron density matrix is considered, realistic open many-electron systems can be studied efficiently.

Consider an electronic system embedded in a thermal bath. The total system-plus-bath Hamiltonian $\widehat{H}_{\rm T}$ can be expressed as

$$\widehat{H}_{\rm T}(t) = \widehat{H}_{\rm S}(t) + \widehat{H}_{\rm B} + \widehat{H}_{\rm SB} \tag{102}$$

$\widehat{H}_S(t)$ is the many-electron system Hamiltonian in the presence of external classical field, assuming the following form

$$\widehat{H}_{\rm S}(t) = \sum_{ij} t_{ij} c_i^\dagger c_j + \frac{1}{2}\sum_{jkk'j'} v_{jj',kk'} c_j^\dagger c_k^\dagger c_{k'} c_{j'} - \vec{E}(t)\cdot\sum_{ij}\vec{\mu}_{ij} c_i^\dagger c_j \tag{103}$$

Here, $c_i^\dagger$ (c_i) is a creation (annihilation) operator of an electron on spin-orbital i. The first and the second terms in Eq. (103) are for the hopping terms t_{ij} and the electron–electron Coulomb integrals $v_{jj',kk'}$, respectively, and can be evaluated via the ground-state geometry. The third term in Eq. (103) is for the interaction between the system and the external electric field $\vec{E}(t)$, and $\vec{\mu}_{ij}$ is the dipole matrix element and $f_{ij}(t) \equiv -\vec{E}(t)\cdot\vec{\mu}_{ij}$. The Hermitian property of $\widehat{H}_S$ implies that $t_{jk} = t_{kj}^*$, $f_{jk} = f_{kj}^*$, and $v_{jj',kk'} = v_{kk',jj'} = v_{j'j,k'k}^*$. In Eq. (102), $\widehat{H}_B$ is the bath Hamiltonian. The system–bath interaction $\widehat{H}_{\rm SB}$ can be generally decomposed in terms of

$$\widehat{H}_{\rm SB} = -\sum_a \widehat{W}_a \widehat{F}_a \tag{104}$$

Here, $\widehat{W}_a$ is Hermitian operator of the system, and up to two-electron terms, it assumes

$$\widehat{W}_a = \sum_{jk} s_{jk}^a c_j^\dagger c_k + \frac{1}{2}\sum_{jkk'j'} w_{jj',kk'}^a c_j^\dagger c_k^\dagger c_{k'} c_{j'} \tag{105}$$

where $s_{jk}^a = (s_{kj}^a)^*$, $w_{jj',kk'}^a = w_{kk',jj'}^a = w_{j'j,k'k}^{a*}$. The forces $\widehat{F}_a$ in Eq. (104) are Hermitian operators in bath space and can thus be considered as the generalized Langevin forces. Denote $\widehat{F}_a(t) \equiv e^{iH_Bt/\hbar}\widehat{F}_a e^{-iH_Bt/\hbar}$, which are stationary stochastical variables in the canonical bath ensembles $\rho_{\rm B}^{\rm eq} = e^{-\beta H_B/\hbar}/{\rm Tr}e^{-\beta H_B/\hbar}$. Their statistical means are set to be zeros ${\rm Tr}_{\rm B}[\widehat{F}_a(t)\rho_{\rm B}^{\rm eq}] = 0$, and the correlation functions are defined as

$$\widetilde{C}_{ab}(t-\tau) \equiv {\rm Tr}_{\rm B}[\widehat{F}_a(t)\widehat{F}_b(\tau)\rho_{\rm B}^{\rm eq}] \tag{106}$$

A conventional QDT for the reduced density operator $\rho(t)$ for the many-electron system reads as [170]

$$i\hbar\frac{d}{dt}\rho(t) = [\widehat{H}_S(t), \rho(t)] - \frac{i}{\hbar}\sum_a [\widehat{W}_a, \widetilde{W}_a(t)\rho(t) - \rho(t)\widetilde{W}_a^\dagger(t)] \tag{107}$$

$$\widetilde{W}_a(t) = \sum_b \int_{-\infty}^{t} d\tau\, \widetilde{C}_{ab}(t-\tau) G(t,\tau)\widehat{W}_b G^\dagger(t,\tau) \tag{108}$$

Here, $G(t,\tau)$ is the Hilbert-space Green's function, satisfying the Schrödinger equation: $i\hbar\partial_t G(t,\tau) = \widehat{H}_S(t)G(t,\tau)$. Equations (107) and (108) are a CS-QDT formulation, constructed via a rigorous second-order cumulant expansion for both the initial canonical thermal equilibrium and the reduced dynamics [170]. However, the implementation of Eqs. (107) and (108) or other conventional forms of QDT should be made with the many-electron eigenstate (or similar) representation. Unfortunately, solving the eigenstates of a many-electron system is itself extremely difficult or intractable. Thus, it is almost impossible to solve Eqs. (107) and (108) numerically for real molecular systems. In practice, the dynamical properties of interacting systems are rather studied by using various indirect techniques [182].

Recast Eqs. (107) and (108) in terms of the EOM for the expectation value of an arbitrary (system) operator $\widehat{O}$, $O \equiv {\rm Tr}[\widehat{O}\rho(t)] \equiv \langle\widehat{O}\rangle$. Its EOM can be obtained as

$$i\hbar\frac{dO}{dt} = \langle[\widehat{O}, \widehat{H}_S(t)]\rangle - \frac{i}{\hbar}\sum_a\{\langle[\widehat{O}, \widehat{W}_a]\widetilde{W}_a(t)\rangle - \langle\widetilde{W}_a^\dagger(t)[\widehat{O}, \widehat{W}_a]\rangle\} \tag{109}$$

The above equations which are equivalent to the CS-QDT [Eqs. (107) and (108)] will be used as the starting point to construct a TDHF-QDT for the open many-electron system under arbitrary coherent driving.

The key quantity here is the reduced single-electron density matrix σ, whose element is defined as the expectation value of the single-electron operator $\hat{\sigma}_{jk} \equiv c_k^\dagger c_j$; i.e., $\sigma_{jk} \equiv \langle \hat{\sigma}_{jk} \rangle = \langle c_k^\dagger c_j \rangle$. The EOM is derived for the reduced single-electron density matrix σ according to Eq. (109). Let us first consider the contribution of the first term in Eq. (109). By using the anticommutation relation for fermions, we have

$$[\hat{\sigma}_{jk}, \widehat{H}_S(t)] = \sum_n \{[t_{jn} + f_{jn}(t)]c_k^\dagger c_n - [t_{nk} + f_{nk}(t)]c_n^\dagger c_j\} + \sum_{mnn'} (v_{jm,nn'} c_k^\dagger c_n^\dagger c_{n'} c_m - v_{mk,nn'} c_m^\dagger c_n^\dagger c_{n'} c_j) \tag{110}$$

The HF approximation to the expectation value of the two-particle operator involves the following Wick's factorization

$$\langle c_m^\dagger c_n^\dagger c_{n'} c_{m'} \rangle \approx \langle c_m^\dagger c_{m'} \rangle \langle c_n^\dagger c_{n'} \rangle - \langle c_m^\dagger c_{n'} \rangle \langle c_n^\dagger c_{m'} \rangle \tag{111}$$

The above two equations lead to $\langle [\hat{\sigma}_{jk}, \widehat{H}_S(t)] \rangle = [h(t), \sigma]_{jk}$, with the Fock matrix

$$h_{jk}(t) = t_{jk} + f_{jk}(t) + \sum_{mn} (v_{jk,nm} - v_{jm,nk}) \sigma_{mn}(t) \tag{112}$$

Obviously, the above HF approximation amounts formally to the following replacement:

$$\widehat{H}_S(t) \Longrightarrow \sum_{jk} h_{jk}(t) c_j^\dagger c_k \tag{113}$$

The contribution of the second term in Eq. (109) is more complicated. In general, $\widetilde{W}_a$ contains any order of many-body operators. Should it be retained up to two-body terms, the evaluation for the second term in Eq. (109) would require treating four-body interactions. In this work, we adopt the following ansatz (i.e., HF approximation) in which [cf. Eqs. (103), (113), and (105)]

$$\widehat{W}_a \Longrightarrow \sum_{jk} \eta_{a,jk}(t) c_j^\dagger c_k \tag{114}$$

$$\eta_{a,jk}(t) = s_{jk}^a + \sum_{mn} (w_{jk,nm}^a - w_{jm,nk}^a) \sigma_{mn}(t) \tag{115}$$

The above ansatz, together with Eq. (113), leads Eq. (108) to

$$\widetilde{W}_a \Longrightarrow \sum_{jk} \tilde{\eta}_{a,jk}(t) c_j^\dagger c_k \tag{116}$$

$$\tilde{\eta}_a(t) = \sum_b \int_{-\infty}^{t} d\tau \widetilde{C}_{ab}(t-\tau) \overline{G}(t,\tau) \eta_b(\tau) \overline{G}^\dagger(t,\tau) \tag{117}$$

Here, $\overline{G}(t,\tau)$ is the Green's function in the HF space; that is, $i\hbar \partial_t \overline{G}(t,\tau) = h(t)\overline{G}(t,\tau)$. By using Eqs. (114) and (116) for Eq. (109), whose second term is now only treating with two-electron operators, the expectation value is then evaluated via again the Wick's factorization as Eq. (111).

The final TDHF-QDT formulation for the single-electron density matrix $\sigma(t)$ can now be summarized as

$$i\hbar\dot{\sigma} = [h, \sigma] - \frac{i}{\hbar} \sum_a [\eta_a, \sigma] \operatorname{tr}\{(\tilde{\eta}_a - \tilde{\eta}_a^\dagger)\sigma\} - \frac{i}{\hbar} \sum_a [\eta_a, (1-\sigma)\tilde{\eta}_a \sigma - \sigma \tilde{\eta}_a^\dagger (1-\sigma)] \tag{118}$$

This equation constitutes the main formal result (TDHF-QDT) of this work. It is derived rigorously via a CS-QDT plus a dynamic mean field approach. It takes account for the effect of second-order system–bath coupling on both dynamics and the stationary (equilibrium) state [170]. The similar formalism can be derived for bosonic systems. The EOM of a bosonic system corresponding to Eq. (118) can be obtained via replacing $1-\sigma$ by $1+\sigma$ in Eq. (118) and replacing the minus sign in Eqs. (112) and (115) by a plus sign.

For a noninteracting system in which $v_{jj',kk'} = w^a_{jj',kk'} = 0$, the matrices h and η are time independent, provided there is no external driving field. In this case, the HF Green's function $\overline{G}(t,\tau) = e^{-ih(t-\tau)}$, and Eq. (117) becomes

$$\tilde{\eta}_a = \sum_b \int_0^\infty d\tau\, \widetilde{C}_{ab}(\tau) e^{-i\overline{\mathscr{L}}\tau} \eta_b \tag{119}$$

which is also time independent. In Eq. (119), $\overline{\mathscr{L}} \equiv [h, \bullet]$, being the HF Liouvillian. As pointed out by Yan et al., Eq. (119) contains the contributions from both the interaction bath spectral and dispersion functions [164, 170]. The latter accounts mainly for the system renormalization energy [170]. Adopt the standard Redfield approximation

$$\tilde{\eta}_a \approx \frac{1}{2}\sum_b \int_{-\infty}^\infty d\tau\, \widetilde{C}_{ab}(\tau) e^{-i\overline{\mathscr{L}}\tau} \eta_b \equiv \frac{1}{2}\sum_b C_{ab}(-\overline{\mathscr{L}})\eta_b \tag{120}$$

which amounts to the neglect of the bath dispersion dynamics effects. Here, $C_{ab}(-\overline{\mathscr{L}})$ is the function of $\overline{\mathscr{L}}$ defined by the bath interaction spectrum

$$C_{ab}(\omega) \equiv \int_{-\infty}^\infty dt\, e^{i\omega t} \widetilde{C}_{ab}(t) = e^{\beta\omega} C_{ba}(-\omega) \tag{121}$$

The second identity in the above equation stands for the detailed balance required by the canonical bath statistics. It is well known that auto-correlation spectrum $C_{aa}(\omega)$ is non-negative, and cross-correlation spectrum $C_{ab}(\omega) = C^*_{ba}(\omega)$ [the spectrum matrix $\{C_{ab}(\omega)\}$, denoted as $\mathscr{C}$, is Hermitian] can be complex. It is shown that the spectrum matrix $\mathscr{C}$ is of complete positivity [181]. Let us now prove that the well-known Fermi–Dirac statistic

$$\sigma^0_{\text{eq}} = \frac{\lambda e^{-\beta h}}{1+\lambda e^{-\beta h}} \tag{122}$$

is the stationary solution to Eq. (118). By the symmetric and detailed-balance relation of bath spectra, we can have that [cf. Eq. (120) and note that η are Hermitian]

$$\tilde{\eta}^\dagger_a = \frac{1}{2}\sum_b C^*_{ab}(\overline{\mathscr{L}})\eta_b = \frac{1}{2}\sum_b C_{ba}(\overline{\mathscr{L}})\eta_b = e^{\beta\overline{\mathscr{L}}}\tilde{\eta}_a \equiv e^{\beta h}\tilde{\eta}_a e^{-\beta h} \tag{123}$$

The above relation leads directly to (cf. $[h, \sigma^0_{\text{eq}}] = 0$)

$$\text{tr}(\tilde{\eta}^\dagger_a \sigma^0_{\text{eq}}) = \text{tr}(\tilde{\eta}_a \sigma^0_{\text{eq}}), \quad \text{and} \quad \sigma^0_{\text{eq}}\tilde{\eta}^\dagger_a(1-\sigma^0_{\text{eq}}) = (1-\sigma^0_{\text{eq}})\tilde{\eta}_a\sigma^0_{\text{eq}} \tag{124}$$

It is thus proved that the well-established quantum statistic, σ^0_{eq} [Eq. (122)], does constitute the stationary solution of TDHF-QDT [Eq. (118)] under the Redfield approximation.

Equation (118) has close resemblance to the conventional TDHF EOM [123], except that the pure dephasing terms in the conventional EOM are replaced by the dissipative terms. The dissipative terms lead to the energy dissipation, whereas the pure dephase terms in the conventional TDHF conserve the system energy. In other words, the conventional TDHF cannot describe the nonradiative decay. In the TDHF-QDT, the dissipative terms are derived from the first principles and the nonradiative decay is accounted for naturally. Although the radiative decay has not been included presently, it can be accounted for within the TDHF-QDT. The energy dissipation causes the energy exchange between the electrons and nuclei and leads to the deterioration of the HF approximation. This may cause the breakdown of Eq. (111). Unlike the TDHF, where the first order of the optical response only induces the

electron–hole part of the density matrix, dissipation terms in Eq. (118) mix the electron–hole, electron–electron, and hole–hole parts. This is the direct consequence of the energy loss resulting from dissipation. The formalism, therefore, is limited to the weak system–bath interaction.

In the formalism, the interactions among electrons are explicitly considered. It would be interesting to quantify the effects of the electronic interaction on the relaxation processes. Switching off the electronic interaction leads to a drastically different electronic structure. This makes the direct comparison between the interacting and noninteracting electronic systems difficult. A possible solution is to start from the noninteracting electronic system and then turn on gradually the electronic interaction, while measuring the related effects.

The TDHF-QDT leads ultimately to the Fermi–Dirac distribution within a mean field formalism. Moreover, the above conclusion can be generalized to the bosons. For a bosonic system, the dynamic mean field QDT leads the system to its Bose–Einstein distribution. Beyond the Redfield approximation [cf. Eq. (120)], the TDHF-QDT [Eq. (118)] actually describes the bath-correlated reduced quantum statistical equilibrium state.

Equation (118) is the main result of the work. It is emphasized that the quantum dissipative terms in Eq. (118) are derived rigorously by starting from the total Hamiltonian and integrating subsequently the bath degrees of freedom. Unlike many other QDTs, these quantum dissipative terms are not phenomenological and can be determined from the first principles. The most important feature of Eq. (118) is that it is the EOM for the reduced single-electron density matrix σ instead of the reduced system density matrix ρ. This leads to the drastic reduction of the degrees of freedom in numerical simulation. The TDHF-QDT developed in this work can thus be used to simulate the realistic and complex open molecular systems.

4.3.3. Markovian Formalism and Its Implementation

The CS-QDT-based TDHF formulation, which is valid for arbitrary non-Markovian excitation-dissipation many-electron systems, is an integro-differential equation. The integral equation Eq. (117) for $\tilde{\eta}_a(t)$ may be solved in a variety of ways, such as the spectral density parameterization [170, 183]. When the Markovian approximation is employed, the numerical implementation of the TDHF-QDT can be greatly facilitated. The Markovian theory can be obtained via the white-noise ansatz under the standard Redfield approximation; that is,

$$\tilde{\eta}_a(t) \approx \frac{1}{2}\sum_b C_{ab}(0)\eta_b(t) \tag{125}$$

where $C_{ab}(0)$ is the interaction spectrum $C_{ab}(\omega)$ taken at $\omega = 0$. From the detailed-balance relation, $C^*_{ab}(\omega) = e^{\beta\omega}C_{ab}(-\omega)$, we conclude immediately that $C_{ab}(0)$ is real; thus $\tilde{\eta}_a$ under the Markovian approximation [Eq. (125)] is Hermitian. As a result, Eq. (118) reduces to

$$i\hbar\dot{\sigma} = [h, \sigma] - \frac{i}{2\hbar}\sum_{a,b} C_{ab}(0)[\eta_a, [\eta_b, \sigma]] \tag{126}$$

Equation (126) has a similar form as the Lindblad equation [166]. To calculate $C_{ab}(0)$, it is assumed that $\tilde{C}_{ab}(t)$ decays exponentially

$$\tilde{C}_{ab}(t) \approx \tilde{C}_{ab}(0)e^{-|t|/\delta\tau} \tag{127}$$

where $\delta\tau \ll 1$ is a timescale parameter that needs to be determined. Equation (127) leads to

$$C_{ab}(0) \approx 2\delta\tau\tilde{C}_{ab}(0) = 2\delta\tau\mathrm{Tr}_B[\hat{F}_a(0)\hat{F}_b(0)\rho_B^{eq}] \tag{128}$$

To compare Eq. (126) with the Lindblad dynamical semigroup QDT [166], we shall use the property of spectral functions that the matrix $\{C_{ab}(\omega)\}$ is positively defined. A Fock-space Hermitian matrix is defined, K^ν, via its elements as

$$K^\nu_{jk} = \sum_a \eta_{a,jk}\sqrt{\Omega_\nu}D^\nu_a \tag{129}$$

where $\{D_a^\nu\}$ and $2\Omega_\nu \geq 0$ being the νth eigenvector and eigenvalue of the matrix $\{C_{ab}(0)\}$. Equation (126) is then recast in the following Lindblad-like form

$$i\hbar\dot{\sigma} = [h, \sigma] - \frac{i}{\hbar}\sum_\nu [K^\nu, [K^\nu, \sigma]] \tag{130}$$

The above equation differs from the conventional Lindblad's semigroup QDT, as both h and K^ν here are Fock-space matrices that depend on σ at local time. The dynamical semigroup property of the Lindblad-like TDHF-QDT [Eq. (126) or Eq. (130)] is yet to be confirmed in general. In the case in which the two-electron components of the bath interaction can be neglected, K^ν becomes independent of σ, and therefore the second term in Eq. (130) does assume the Lindblad dissipation form. Note that although the dissipative term in Eq. (130) is of Lindblad-like form, it has very different physical meanings. Equation (130) is the EOM for the reduced single-electron density matrix σ, not the system density matrix ρ. The positivity form of the nonlinear EOM for single-electron reduced density matrix is yet to be explored. However Eq. (130) can be linearized by decomposing $\sigma(t)$ as

$$\sigma(t) = \sigma^{(0)} + \delta\sigma(t) \tag{131}$$

where $\sigma^{(0)}$ is the equilibrium reduced single-electron density matrix that is approximated by the ground-state reduced single-electron density matrix in this work, and $\delta\sigma$ is the deviation or fluctuation, which is much less than $\sigma^{(0)}$. To the first order in $\delta\sigma$, Eq. (130) becomes

$$i\hbar\frac{d}{dt}\delta\sigma = [h^{(0)}, \delta\sigma] + [\delta h, \sigma^{(0)}] - \frac{i}{\hbar}\sum_\nu [K^\nu, [K^\nu, \delta\sigma]] \tag{132}$$

where $h^{(0)}$ is the ground-state Fock matrix; that is,

$$h_{jk}^{(0)} = t_{jk} + \sum_{mn}(v_{jk,nm} - v_{jm,nk})\sigma_{mn}^{(0)} \tag{133}$$

and

$$\delta h_{jk}(t) = f_{jk}(t) + \sum_{mn}(v_{jk,nm} - v_{jm,nk})\delta\sigma_{mn}(t) \tag{134}$$

It is important that the integration of Eq. (132) in the time domain is stable, as integrating first-order differential equations is often numerically unstable. It is shown that $\delta\sigma(t) \to 0$ in Eq. (132) as $t \to \infty$ when K^νs are Hermitian. This ensures that integrating Eq. (132) is numerically stable. Equation (130) is a special case of the TDHF-QDT when the Markovian bath is taken, and Eq. (132) is the linear response version of Eq. (130). Note that Eq. (130) does not lead to the Fermi–Dirac distribution as $t \to +\infty$ because the Markovian bath is adopted.

To demonstrate of the feasibility of applying the TDHF-QDT formalism to realistic complex molecular systems, we employ Eq. (132) to simulate the photoexcitation and subsequent nonradiative relaxation of an embedded butadiene molecule in a liquid or solid matrix. The PM3 Hamiltonian [184] is used for $\widehat{H}_S$. The position of the atom is denoted by q_{ms}, where the subscript s is for the direction. Then q_{ms} can be expanded as

$$q_{ms} = q_{ms}^{(0)} + \delta q_{ms} \tag{135}$$

where $q_{ms}^{(0)}$ is q_{ms} in equilibrium and δq_{ms} is the deviation. The nuclei are taken as a part of the bath and couple directly to the valence electrons. The liquid or solid surrounding serves as an energy sink that ensures the nuclei in thermal equilibrium at a temperature T. The bath Hamiltonian $\widehat{H}_B$ describes the vibration of these nuclei,

$$\widehat{H}_B = \sum_{m,s}\frac{p_{ms}^2}{2M_m} + \frac{1}{2}\sum_{m,n,s,t} V_{ms,nt}\delta q_{ms}\delta q_{nt} \tag{136}$$

where p_{ms} is the momentum component of the mth atom along s-direction, $V_{ms,nt}$ is the effective interaction between two atoms m and n, and M_m is the mass of the mth atom. The term $\widehat{H}_B$ can be determined directly from the vibrational modes and vibrational frequencies of these nuclei, and it can thus be evaluated from the first-principles or semiempirical calculations.

The system-bath coupling term H_{SB} describes the energetics when the nuclei deviate from their equilibrium positions. Yokojima et al. consider only the weak system–bath coupling case; that is, $\widehat{H}_{\mathrm{SB}}$ is given by

$$\widehat{H}_{\mathrm{SB}} = \sum_{m,s} \frac{\partial \widehat{H}_S}{\partial q_{ms}} \delta q_{ms} \tag{137}$$

$\partial \widehat{H}_{\mathrm{S}}/\partial q_{ms}$ and δq_{ms} correspond to $\widehat{W}_a$ and $\widehat{F}_a$, respectively. The term δq_{ms} is relatively small, and $\widehat{H}_{\mathrm{SB}}$ is thus weak as compared to $\widehat{H}_{\mathrm{S}}$ and $\widehat{H}_{\mathrm{B}}$. It is observed that the derivatives of t_{ij} with respect to q_{ms} are much larger than those of $v_{ij,kl}$, and thus keep only $\partial t_{ij}/\partial q$ in the evaluation of $\partial h/\partial q$ in the calculations. In other words, the two-electron terms in $\partial \widehat{H}_S/\partial q_{ms}$ are neglected. It is thus found that $\eta_{a,ms} = s^a_{ms} = \partial t_{ij}/\partial q_{ms}$ and $\widehat{F} = \vec{q}$. According to Eq. (128),

$$\widetilde{C}_{ab}(0) = \mathrm{Tr}_{\mathrm{B}}[q_a q_b \rho_{\mathrm{B}}^{\mathrm{eq}}] \tag{138}$$

Using the fact that the nuclei are in thermal equilibrium at T

$$K^{\nu}_{ij} \equiv \sum_{m,s} \frac{\partial t_{ij}}{\partial q_{ms}} \sqrt{\frac{\hbar}{2M_m\omega_\nu} \coth\left(\frac{\beta\hbar\omega_\nu}{2}\right)} Q^{\nu}_{ms} \tag{139}$$

where ω_ν and Q^{ν}_{ms} are the frequency and the mth atom's displacement along the s-direction for the νth nuclear vibrational mode, respectively. In the derivation, the nuclear–nuclear correlation $\langle \delta q_{m_1 s_1} \delta q_{m_2 s_2} \rangle$ is calculated by assuming that nuclear vibrational modes are in thermal equilibrium with the surrounding at a temperature T. In the calculations, the energy is exchanged among the excitations, whereas the total number of electrons is conserved. The timescale parameter $\delta\tau$ can be determined from the molecular mechanics simulation, and in this work it is taken as a phenomenological parameter that is used to fit the experiments.

The geometry optimization, the nuclear vibrational modes, and their frequencies are obtained in the similar way as Ref. [185] by a BLYP [186] calculation with 6-311G(d,p) basis set. It is found that the BLYP calculation yields much better optimized geometry and vibrational frequencies than the PM3 method. Therefore, in this work, Yokojima et al. adopt the optimized geometry, vibrational modes, and vibrational frequencies calculated by the BLYP method [186] with 6-311G(d,p) basis set. In other words, $\widehat{H}_{\mathrm{B}}$ is determined by the BLYP calculation adopting 6-311G(d,p) basis set. The dipole matrix element $\vec{\mu}_{ij}$ is evaluated with the neglect of diatomic differential overlap (NDDO). The resulting 1,3-butadiene is placed in x-y plane, as depicted in Fig. 14. The electric pulse is expressed as $E(t) = E_0 \exp(-t/\bar{t})^2$ with $\bar{t} = 0.1$ fs, and its polarization is along the x-direction. Equation (132) is solved in the time domain. Temperature T is taken as 30, 100, 300, and 600 K, and $\delta\tau = 0.125$ fs is used. The absorption spectrum can be obtained by Fourier transforming the induced polarization $\vec{P}(t) = \mathrm{tr}[\vec{\mu}\delta\sigma(t)]$ and is plotted in Fig. 14a for $T = 300$ K. The first peak appears at 4.6 eV, and its full-width-half-maximum (FWHM) is found to be 0.51 eV. The new formalism presented in this work includes the interactions between the valence electrons and all vibrational modes. This means that the calculated ΔE_{FWHM} correspond to homogeneous broadenings. The 0.51 eV FWHM of the first peak agrees approximately with the experimental measure of ~ 0.5 eV [187]. This is the reason why the value 0.125 fs of $\delta\tau$ is adopted in the calculations. Another major absorption peak is found at 8.7 eV with a lower FWHM of 0.40 eV. The different peak widths indicate the different decay rates of the two excitations at 4.6 and 8.7 eV. Figure 14b shows the amplitudes of the two excitation modes versus time. The amplitudes are calculated by projecting the density matrix onto each modes of $\mathscr{M}^{\mu}$ [i.e.,

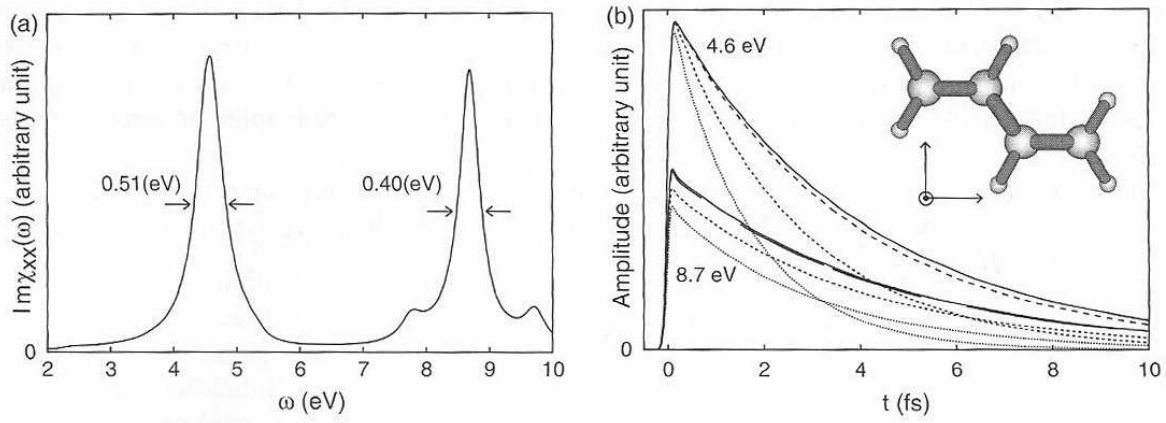

Figure 14. (a) Absorption spectrum at $T = 300$ K. (b) shows the relaxations of the two excitations (4.6 and 8.7 eV): amplitude of the mode versus t. 1,3-butadiene is placed as shown in the inset. Solid, long dashed, short dashed, and dotted line are for the 4.6 and 8.7 eV excitations at $T = 30$ K, $T = 100$ K, $T = 300$ K, and $T = 600$ K, respectively. Reprinted with permission from [181], S. Yokojima et al., *J. Comp. Chem.* 24, 2083 (2003). © 2003, Wiley Periodicals, Inc.

the eigenvector of Eq. (132) in the absence of external field] as

$$\mathcal{S}^{\mu}(t) = \left| \sum_{i,j} ((\mathcal{M}^{\mu})^{-1})_{ij} \delta\sigma_{ij}(t) \right| \tag{140}$$

with

$$\sum_{i,j} |\mathcal{M}^{\mu}_{ij}|^2 = 1 \tag{141}$$

The decay half-time $_{\Delta}\tau_{1/2}$ for 4.6 and 8.7 eV at temperature $T = 300$ K is 1.8 fs and 2.6 fs, respectively. It is verified that $_{\Delta}E_{\mathrm{FWHM}}{}_{\Delta}\tau_{1/2} \sim \hbar$ for the two excitations. Note that the 4.6-eV excitation decays always faster than the 8.7-eV excitation, especially at the high temperatures. The decay half time of individual electronic excitation is found to be dependent on temperature T. This is because the nuclear motion varies with changing temperature. In general, the increasing temperature leads the faster decays. The 4.6-eV excitation is more sensitive on T, and its decay rate increases much faster than the 8.7-eV excitation as T is raised. This is because the 4.6-eV excitation couples more strongly to the nuclear motion, which is examined more closely below.

Table 3 shows the coupling strength between electronic excitations and nuclear vibrational modes. Vibrational modes are arranged from top to bottom with increasing order of energy. Electronic modes $\mathcal{M}_0^{122}$ and $\mathcal{M}_0^{144}$ correspond to the peaks at 4.6 and 8.7 eV in Fig. 14, respectively. The diagonal terms $\bar{\Gamma}_{\alpha,\alpha}$ are the pure dephasing for mode α and are much larger than the off-diagonal terms. The large pure dephasing is likely a result of all the couplings between the electronic excitation and different phonons that destroy the electronic phase coherence. The term $\overline{\Gamma}^{\nu}_{122,122}$ is large for lower vibrational frequency modes and generally very small for higher vibrational modes, while in contrast, $\overline{\Gamma}^{\nu}_{144,144}$ shows a less-vibrational frequency dependence. This leads to the different decay behaviors for the two excitations, as shown in Fig. 14b. For very lower temperature ($\beta \to \infty$), $\coth(\beta\hbar\omega_{\nu}/2) \sim 1$ irrespective of ν. Because the ratio $\sum_{\nu} \overline{\Gamma}^{\nu}_{122,122} / \sum_{\nu} \overline{\Gamma}^{\nu}_{144,144}$ is about 1.2, the decay rates of the 4.6- and 8.7-eV excitations are thus similar. For high temperatures, that is, $\beta\hbar\omega_{\nu} \ll 1$, $\coth(\beta\hbar\omega_{\nu}/2) \sim 1/\beta\hbar\omega_{\nu} = k_B T/\hbar\omega_{\nu}$. Thus, the low-frequency vibrational modes dominate the contribution to the dissipation. Further, $\overline{\Gamma}^{\nu_{13}}_{122,122}/\overline{\Gamma}^{\nu_{13}}_{144,144} \sim 2.8$; the 4.6-eV excitation thus decays much faster than the 8.7-eV one at high temperatures.

It has been shown that the new formalism can be employed to simulate the nonradiative relaxations of realistic many-electron molecular systems that are in contact with thermal baths. Various excitations may couple differently to the thermal bath, and this is taken into account naturally by the new formalism. The Markovian TDHF-QDT developed here is essentially the same as the formula presented in Ref. [180], although the derivations are seemingly different. Inclusion of the radiative decay process into the EOM should be

Table 3. Coupling strength between electronic excitations and nuclear vibrational modes. Vibrational modes are arranged from top to bottom with increasing order of energy.

	ν	$\omega_\nu(\text{cm}^{-1})$	$\overline{\Gamma}^{\nu}_{122,122}$	$\overline{\Gamma}^{\nu}_{122,144}$	$\overline{\Gamma}^{\nu}_{144,144}$
1	ν_{13} Au	173.1	0.429	−0.050	0.153
2	ν_{24} Bu	294.3	0.003	0.012	0.067
3	ν_{9} Ag	508.0	0.003	0.007	0.034
4	ν_{12} Au	520.9	0.228	0.019	0.114
5	ν_{16} Bg	755.7	0.173	0.020	0.071
6	ν_{8} Ag	876.9	0.009	0.005	0.059
7	ν_{11} Au	888.8	0.179	−0.008	0.039
8	ν_{15} Bg	892.4	0.177	−0.006	0.041
9	ν_{14} Bg	963.3	0.111	−0.001	0.050
10	ν_{23} Bu	981.6	0.003	0.011	0.058
11	ν_{10} Au	1025.1	0.096	0.005	0.039
12	ν_{7} Ag	1194.3	0.018	0.008	0.046
13	ν_{6} Ag	1280.8	0.014	0.005	0.036
14	ν_{22} Bu	1288.6	0.006	0.009	0.040
15	ν_{21} Bu	1379.3	0.009	0.001	0.037
16	ν_{5} Ag	1439.7	0.008	0.008	0.049
17	ν_{20} Bu	1593.6	0.040	−0.012	0.053
18	ν_{4} Ag	1633.5	0.098	0.006	0.059
19	ν_{3} Ag	3037.6	0.003	0.010	0.034
20	ν_{19} Bu	3048.9	0.003	0.010	0.030
21	ν_{2} Bu	3053.9	0.002	0.005	0.043
22	ν_{18} Ag	3055.0	0.002	0.006	0.043
23	ν_{1} Ag	3137.0	0.002	0.011	0.070
24	ν_{17} Bu	3137.3	0.002	0.011	0.070

$\overline{\Gamma}^{\nu}_{\alpha\alpha'}$ is given in eV/fs. Electronic excitation modes $\mathscr{M}_0^{122}$ and $\mathscr{M}_0^{144}$ correspond to the peaks at 4.6 and 8.7 eV in Fig. 14, respectively. Reprinted with permission from [181], S. Yokojima et al., *J. Comp. Chem.* 24, 2083 (2003). © 2003, Wiley Periodicals, Inc.

straightforward. The different timescales are required for radiative and nonradiative decays. Explicit inclusion of the nuclear vibrational modes or multiconfigurational effects to the current scheme is challenging but feasible.

Yokojima et al. set out to achieve two objectives. The first objective was to demonstrate the applicability of TDHF-QDT to real molecular systems. Our simulation has clearly captured the essential physics of the nonradiative decay of a butadiene molecule, for instance, the rate dependence on temperature and different decay rates for different excited states that were not built into the theory phenomenologically but are, rather, the nature consequences of the dissipation terms derived directly from the Hamiltonian. The first objective is thus achieved with success. The second objective is to examine the decaying processes of the embedded butadiene molecule on photoexcitation. This is carried out under the Markovian approximation. Our simulation predicts that the excitation at 4.6 eV decays rapidly at room temperature and that its decay rate is sensitive to the temperature because it couples strongly with low-frequency vibrational modes. The validity of this prediction rests on the Markovian approximation and should be tested experimentally. The Markovian version of the TDHF-QDT was used in the simulation instead of the non-Markovian TDHF-QDT because the former is computationally less expensive. It is assumed the system–bath factorization ansatz and use the HF ground state for the system ground state. The energy dissipation causes the energy exchange between the electrons and nuclei and leads to the deterioration of the HF approximation. An improved approach is to find the equilibrium state under the system–bath couplings and thermal fluctuations [181]. Our equation does not consider the large-amplitude motion and photoisomerization. Those effects are beyond the scope of this work, which is intended to develop and illustrate the applicability of the TDHF-QDT formalism for realistic open systems. Franck–Condo calculation of absorption spectrum requires the explicit determination of excited states and their energy surfaces. In this implementation, the vibronic structure cannot be evaluated because the vibrational modes are not included in the system. This can be achieved by including the nuclei as a part of the system.

It is emphasized that this formalism is based on the EOM of a reduced single-electron density matrix and is very different from the conventional QDTs that follow the dynamics of the reduced-density matrix of the system. Therefore, this formalism can be applied to much larger and realistic systems. In the calculation, all valence electrons (a total of 22 electrons) are included explicitly and take into account the couplings between all valence electrons and all vibrational modes. For most conventional QDTs, one solves the electronic structures first and then adds T_1 and T_2 relaxation terms phenomenologically [152, 177]. In principle, the T_1 and T_2 relaxation terms can be evaluated explicitly [177]. However, because extremely large computational resources are required, this has not been done for realistic many-electron systems [177]. Utilizing the locality of $\langle \widehat{F}_a \widehat{F}_b \rangle$, Eq. (126) can be combined with the LDM method [58, 59, 62]. This leads to the dramatic reduction of computational times, and thus the possibility of simulating very large, complex, open molecular systems.

4.4. Applications of the Localized-Density-Matrix Method

4.4.1. Photo-Induced Excitations in Poly(p-phenylenevinylene) Aggregates

Important progress has been made toward the commercialization of polymer light emitting diode (LED) [188–190]. PPV and its derivatives are among the most studied light-emitting polymers. Pristine PPV films have distinctive vibronic features in their absorption spectra that indicate the corresponding excitations in pristine PPV films are intrachain in nature [191]. This has been explained by the fact that the interchain couplings in PPV aggregates are relatively weak. Subjected to high pressures, the absorption and emission spectra of PPV films red shift alike [192]. This was interpreted that the excitations for the absorption and luminescence acquire interchain components as the interchain distances decrease [192]. The absorption spectra of poly(2-methoxy,5-(2′ethyl-hexyloxy)-*p*-phenylenevinylene) (MEH-PPV) and cyano-substituted PPV (CN-PPV) thin films shift little in energy compared to their counterparts in dilute solutions, whereas the corresponding emission spectra of thin films have large red shifts [193–195]. One view is that the excitations responsible for the absorptions in MEH-PPV and CN-PPV must be intrachain because their absorption spectra in dilute solutions and films differ little [193, 194]. Because the emission spectra of thin films and dilute solutions are quite different, the luminescences in the films are likely caused by the interchain excitations [193, 194]. This was seemingly supported by the appearance of distinctively different excitations in CN- and MEH-PPV films observed in transient photoluminescence [193, 194] and transient photo-induced absorption studies [193]. Another view is that the excitations responsible for the luminescence are intrachain, and the red shifts of emission spectra are caused by the excitations that migrate to the longer conjugated chains in films or aggregates [196].

We review here Chen and coworkers' numerical study of the photo-induced excitations in PPV aggregates [197]. Two types of PPV aggregates are investigated. One type is arranged according to the PPV crystal structure [61, 198], which is denoted as type I. The structure of a four-chain type I aggregate is depicted in Fig. 15(a). The C–C bond lengths along the benzene ring are set to 1.39 Å, and all the angles on the benzene are set to 120 degrees. The C–H bond lengths are 1.09 Å. The single and double bond lengths in the vinylene group are 1.44 and 1.33 Å, respectively. Each chain is aligned along the x-axis, and there are 3.28- and 1.64-Å displacements along x-direction from C to A and from B to A, respectively. Two chains are either parallel (as A and C) or tilted to each other with an angle of 76 degrees (as A and B). The axes of C and B are displaced by (4.00 Å, 3.12 Å) and (−0.31 Å, 4.53 Å) in the y–z plane from that of A. Chain D is added with the same corresponding displacement vectors and angles with respect to B and C (see Fig. 15a). Each PPV chain is made of multiple repeating units. To model CN-PPV and MEH-PPV films, which are expected to have larger interchain hoppings [195], or the PPV solid under high pressure [192], Chen et al. reduced the interchain distances of type I by 10% to enhance the interchain couplings, and the resulting structures are denoted as type II. The photo-induced excitations in I and II are calculated with the LDM method [58, 59, 61]. Semiempirical complete neglect of differential overlap in spectroscopy (CNDO/S) Hamiltonian [141] is used in the calculation. On the application of an external field, the reduced single-electron density matrix ρ may

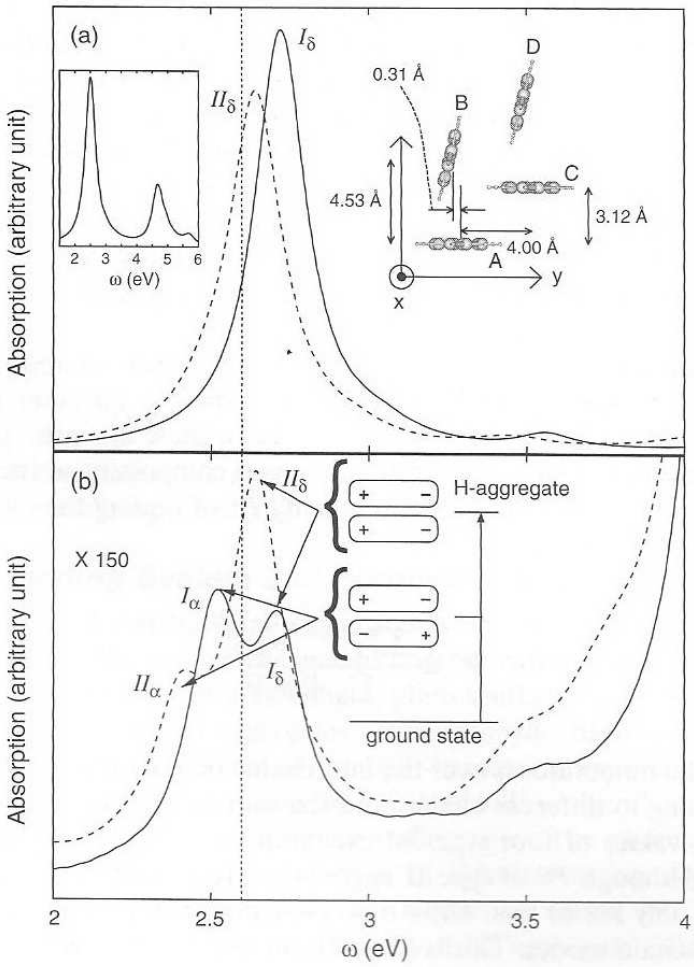

Figure 15. Absorption spectra for 4-4 PPV aggregates. The solid lines are of type I, and the dashed lines for type II. The electric field is polarized (a) along the chain axis and (b) perpendicular to the plane of A; $\gamma = 0.1$ eV. The inset in (a) is the absorption spectrum of an 8-4 aggregate with the crystal structure. The inset in (b) depicts two typical types of excitations in an H-aggregate. The arrows indicate the types of excitations for the absorption peaks. Reprinted with permission from [197], S. Yokojima et al., *Chem. Phys. Lett.* 333, 397 (2001). © 2001, Elsevier Science B. V.

be expressed as $\rho = \rho^{(0)} + \delta\rho$, where $\rho^{(0)}$ is the ground-state reduced single-electron density matrix and $\delta\rho$ is the induced density matrix by the external field. The term $\delta\rho$ contains the excited state information, for instance, the optical properties, and can be determined by solving its Heisenberg equation of motion within the TDHF or random phase approximation [122]. The reduced-density matrix $\delta\rho^\nu$ for individual photo-induced excited state ν with energy Ω_ν can be projected from $\delta\rho$.

The absorption spectra of two four-chain aggregates of types I and II are shown in Fig. 15, and each chain has four repeating units (denoted as 4-4). The solid lines are of type I, and the dash lines are type II. Two polarized electric fields are applied. Figure 15a depicts the absorption spectra for the electric field polarized along the x-axis. The absorption spectrum of type II red shifts as compared to that of type I, which is consistent with the experimental observation that the pressure on PPV films induces the red shift of absorption spectra [192]. The dashed line at $\omega \approx 2.6$ eV represents the optical gap of a single four-unit PPV chain. This indicates that the absorption spectra of PPV films actually blue-shift compared to that of single chain or the dilute solution. Aggregate I has a large blue-shift for the absorption (I_δ) and II has a much smaller one (II_δ). This is consistent with the experimental observations that MEH-PPV and CN-PPV films have little shifts of their absorption spectra compared to the dilute solutions [193, 194, 199]. When the electric field polarizes along the z-axis, the absorption spectra change dramatically, as plotted in Fig. 15b. A new peak (I_α or II_α) appears for each aggregate. This is the so-called Davydov splitting [200]. Each aggregate I or II has a total of four such excitations, and the other two are denoted as β and γ. Note that

the signals in Fig. 15b are amplified by 150 times, as compared to those in Fig. 15a, which implies that the oscillator strengths of I_α and II_α are very small. Similarly, β and γ have very small oscillator strengths as well. This is the reason why the excitations I_α and II_α cannot be detected in the absorption spectra. Among these four excitations, for each aggregate δ mode has the highest energy, and γ the second highest. The energies of α and β are very close. For instance, the energy difference between I_α and I_β is 0.02 eV. For aggregate I, I_β has the lowest energy, and for II, II_α the lowest. After the photo-excitation, I_δ (II_δ), decays nonradiatively into the low-lying modes I_α or I_β (II_α or II_β) from which the emission occurs. The inset in Fig. 15a is the absorption spectrum of a type I aggregate made of four eight-unit chains (denoted as 8-4).

Chen and coworkers' calculated results agree with the observed absorption and emission spectra of PPV and its derivatives [192–194, 199]. Now the question is what exactly the characteristics of these photo-induced excitations are in these systems. The interchain composition of each excitation is examined. The interchain component of the density matrix $\delta\rho^\nu$ for excitation ν may be measured by the probability P^ν of finding the electron-hole residing separately at two different chains

$$P^\nu \equiv \frac{\sum_{i,j}^{\text{interchain}} |\delta\rho_{ij}^\nu|^2}{\sum_{i,j} |\delta\rho_{ij}^\nu|^2} \tag{142}$$

where the sum on the numerator is over the interchain components of $\delta\rho^\nu$, that is, the atomic orbitals i and j belong to different chains, and the sum on the denominator is over all pairs of i and j. The P^ν values of four types of excitations are shown for 4-4 PPV aggregates I and II in Table 4. Although P^ν of type II aggregates are an order of magnitude larger than those of I, they are only 5% or less. Thus, it is concluded that the excitations in both I and II aggregates are intrachain modes. This is a significant result that calls for the reinterpretation of many experiments [193–195, 199, 201].

Chen et al. examined the nature of photo-induced excitations by calculating their induced charge distributions [197]. For I_α and II_α, the net charges of individual units along the x-direction alternate from minus to plus in A and C and from plus to minus in B and D. This implies that the intrachain transition dipole moments for A and B (or C and D) are of opposite phases. In contrast, the charge distribution is from plus to minus for I_δ and II_δ in all the chains, which implies that the transition dipole moments of all chains are of the same phase. This results in I_α (II_α) having a lower energy than I_δ (II_δ). Similarly, I_β and I_γ (II_β and II_γ) have smaller overall transition dipole moments and thus lower energies than I_δ (II_δ). This is analogous to the excitations in H-aggregates [202] and explains the reason why the absorption spectra in Fig. 15a blue-shift compared to that of a single chain.

A closer look reveals the difference in the induced charge distributions between the crystal and reduced structures. Chen et al. calculated the total charge of each chain [197]. For the crystal structure I, the total induced charges of individual chains are virtually zero, indicating that no charge transfer occurs. However, the induced charges on individual chains are not zero for II_α, II_β, II_γ, and II_δ, implying that the charge transfer occurs for the reduced structure II. Thus, the larger inter-chain interaction induces the charge transfer among different chains.

Table 4. P^ν values of four types of excitations α, β, γ, and δ for 4-4 PPV aggregates *I* and *II*.

ν	ω (eV)	P^ν	ν	ω (eV)	P^ν
I_α	2.51	0.0049	II_α	2.40	0.051
I_β	2.49	0.0036	II_β	2.41	0.037
I_γ	2.54	0.0026	II_γ	2.49	0.029
I_δ	2.72	0.0039	II_δ	2.64	0.040

To understand the energy shifts, Chen et al. decompose the excited-state energy into kinetic and Coulomb components and into further intra- and interchain components for kinetic parts [197]. The Coulomb-induced shifts are positive for I_δ and II_δ and negative for others. This is consistent with the H-aggregate picture. The interchain components of kinetic energy–induced shifts are all negative, which means that the interchain hoppings reduce the kinetic energies. These reductions are much larger for the reduced structures II as compared to those of the crystal structures I because the interchain interactions decay exponentially versus the distance and are thus much larger for the reduced structures. This results in larger red shifts for II_α, II_β, and II_γ, as both the kinetic energy and the Coulomb interaction induce the red shifts as well as little shifts for II_δ because the kinetic and Coulomb terms tend to cancel each other. This interplay between the interchain kinetic and Coulomb terms explains the spectra shifts of absorption and luminescence for CN- and MEH-PPV aggregates and solutions [193–195]. For type I aggregates, the interchain hoppings are much weaker, and thus, the Coulomb term dominates. This results in the blue- and red shifts for the absorption and luminescence spectra, respectively [203].

4.4.2. Light-Harvesting System 2 in Purple Bacteria

The basic energy source for virtually all organisms is photosynthesis, by which green plants and other organisms use the energy of light to convert carbon dioxide and water into the simple sugar glucose. To better capture sunlight, photosynthetic systems have developed various antenna systems that contain aggregates of chlorophylls, bacteriochlorophylls (BChls), or other chromophores. The structures of the light-harvesting apparatus in purple bacteria, such as *Rhodopseudomonas (Rps.) acidophila* [204] and *Rhodospirillum (Rs.) molischianum* [205], have been resolved recently by X-ray crystallography. The photosynthetic unit (PSU) in these purple bacteria is generally composed of light-harvesting aggregates of bacteriochlorophyll (LH1 and LH2), carotenoids, and a reaction center (RC). The LH1 (B875) aggregate encircles the reaction center, whereas the LH2 aggregate (B800 and B850) forms a peripheral network of pigment-proteon complexes located next to the LH1 aggregate. The carotenoid found in *Rs. molischianum* is Lycopene (Lyc), which plays an important role in structure stabilization and in preventing the formation of harmful singlet oxygen [206]. Sunlight is harvested by the LH2 and carotenoids, and the energy will be transferred to the LH1, and finally to the RC. This efficient energy transfer process has drawn much theoretical and experimental interest.

Excitation transfer can arise from two mechanisms in photosynthetic antenna systems, known as the Förster incoherent hopping (Markovian) [207, 208] and the coherent exciton migration [200]. In the former case, the excitation is localized, that is, the exciton resides on one or a few BChls-a, whereas in the latter case, the exciton is coherently delocalized over a large number of BChls-a or over the entire ring. Qualitatively speaking, the size of the excitonic coherence is determined by the ratio of the nearest-neighbor coupling constant to the energy disorder [209]. The energy disorder can either be static (spectral inhomogeneities) or dynamic (electron–phonon interactions) [210–212]. If the energy disorder is much larger than the exciton coupling constants between adjacent BChls-a, Förster incoherent hopping is dominant. On the contrary, strong intermolecular interactions between next-nearest neighbor (denoted as J) would result in more significant delocalization of the excitation, and transfer via coherent exciton migration is then dominant.

There are many experimental and theoretical studies for determining the exciton size in LH2. Various results in which the exciton size ranges from a few pigment molecules [213–218] to the entire ring [219] have been reported. In particular, pump-probe spectroscopy predicted a coherence length covering a few BChl molecules [220, 221], and the experiment studying the superradiance of the B850 ring at room temperature resulted in a coherence length of about three pigments [216]. Transient absorption study [219] showed that the exciton is delocalized in the entire B850 ring. Theoretical studies such as the Redfield theory and the path integral formulation estimated a delocalization length of two to four pigments [153, 217, 222]. The static energy disorder has been measured directly from the absorption line widths in hole-burning experiments. It was concluded that static energy disorder varies between 200 and 500 cm^{-1}. Dynamic disorder was estimated to be between 100 and 500 cm^{-1}.

The interchromophore coupling constants play an important role in the energy transfer process. Their values are difficult to measure experimentally, and therefore, they need to be evaluated by QM methods.

The LH2 complex of *Rs. molischianum* is built from $\alpha\beta$-heterodimers forming an eight-unit circular aggregate with C_8 symmetry. Each unit contains a pair of α and β polypeptides, three BChls-a and one carotenoid. The polypeptides bind to the BChls-a and the carotenoid noncovalently. The BChls-a form two rings, named according to their corresponding absorption maxima at 800 and 850 nm, as the B800 and B850 rings. The B850 ring consists of 16 tightly positioned BChls-a, and the B800 ring of eight loosely spaced BChls-a. Hence, the crystal structure of *Rs. molischianum* is an octamer. A projection of the B850 and B800 aggregates onto the ring-plane is shown in Fig. 16. By a measurement based on the central Mg atom in the porphin ring, the radius of the B850 ring is approximately 23 Å, and that of the B800 ring is 28 Å. The geometries of the BChls-a within an $\alpha\beta$-heterodimer unit are slightly different. The B800 ring contains eight units of BChls-a with about 22 Å between neighboring Mg atoms. For the B850 ring, the BChls-a bound to the α-apoprotein and β-apoprotein are labeled as α-BChl-a and β-BChl-a, respectively, as shown in Fig. 16a. The Mg-to-Mg distance is about 9.36 Å for the 1α-1β dimer, and about 8.78 Å for the 1β-2α dimer, which can be compared with the center-to-center values in Ref. [209]. Note that the Mg-to-Mg distances in the intra- and interdimers were found to vary for different crystal structure data. This can be attributed to the fact that protein forms different conformers on crystallization, and the reported distances in Ref. [205] are the average among the conformers. Hence, the crystalline Mg-to-Mg distances are also slightly different from those in *in situ* LH2. In the calculations, the crystal data are adopted without any modifications to generate the B850 and B800 rings according to C_8 symmetry and the known geometrical parameters [205].

Within the B850 ring, the BChls-a are closely packed and the inter-BChl-a is comparable to the chromophore size (9 Å). As the chromophore is mainly located on the porphin ring, the phytyl tail and some alkyl groups were eliminated during the calculations. Each BChl-a was truncated to 46 indexed atoms (cf. Fig. 16b). The total number of atoms for the B800 ring is 368, and for the B850 ring, 736. In this work the low-energy absorption Q band of the BChl-a is the main concern. The lowest two transitions for the BChl-a are the Q_y and

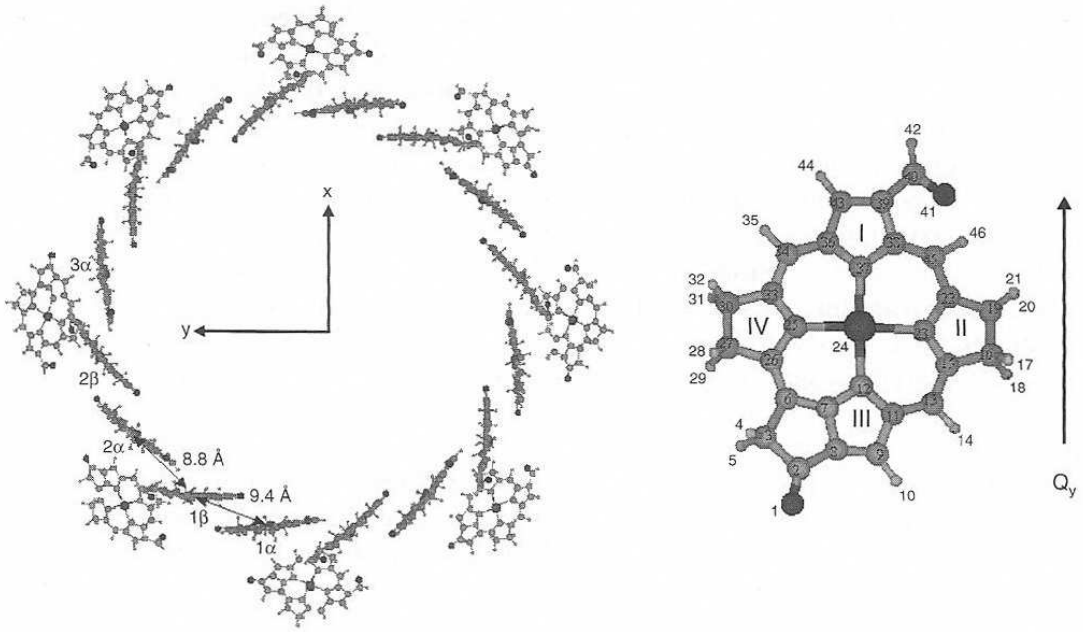

Figure 16. (a) The labeling scheme of LH2. Note that the Mg-to-Mg distances for 1α-1β dimer, 1β-2α dimer, 1α-2α dimer, 1β-2β dimer, 1α-2β dimer, and 1β-3α dimer are 9.4, 8.8, 17.4, 18.0, 26.0, and 25.5 Å, respectively. The outer ring is the B800 ring and the inner ring is the B850 ring. (b) The truncated bacteriochlorophyll-a (BChl-a), which contains 46 atoms. Reprinted with permission from [228], M. F. Ng et al., *J. Phys. Chem. B* 107, 9589 (2003). © 2003, American Chemical Society.

Q_x transitions. The corresponding transition dipole moments lie along the two perpendicular directions [223, 224] in the porphin ring, as shown in Fig. 16b. Several calculations were carried out for the LH2 from *Rs. molischianum*, and different calculated J values were reported. The collective-electronic-oscillator (CEO) method [225, 226] was applied to calculate the dimeric coupling constants for the LH2. It was determined that two coupling constants J_1 and J_2 are, respectively, 408 and 366 cm^{-1} (J_1 is denoted as the 1α-1β coupling constant, and J_2 as the 1β-2α coupling constant). Cory et al. [227] used a generalized Frenkel exciton model by including long-range dipolar interactions to describe the low-lying excitonic states. They carried out an INDO (intermediate neglect of differential overlap)/S (spectrum) calculation at the configuration-interaction-singles (CIS) level on the entire B850 ring. The resulting energy levels were employed to determine the parameters in their Frenkel exciton model. Computational feasibility limited their configuration-interaction (CI) expansion to 4096 configurations for each of the A and B representations of the C_8 symmetry group, and 790 and 369 cm^{-1} were reported for J_1 and J_2, respectively. The same method was used previously by Hu et al. [206], but with a CI expansion of 512 configurations for each symmetry class, and the authors reported 806 and 377 cm^{-1} for J_1 and J_2, respectively. Sundström et al. [209] used the point-dipole approximation (PDA) to calculate J_1 and J_2, which were found to be 339 and 336 cm^{-1}, respectively. All these studies were based on the crystal structure model [205] with C_8 symmetry, and no structural disorder was included.

The calculated values for J_1 and J_2 vary from 300 to 800 cm^{-1}, which implies that the energy transfer can either be via Förster hopping or via the exciton coherent migration. Most of these calculations were on monomers or dimers, except the calculation by Schulten, Zerner, and coworkers, which was on the entire B850 ring [206, 227]. Apparent discrepancies between the calculated results from dimers and from the entire B850 ring require further investigations. One possible cause is that long-range Coulombic interactions in the ring are absent in dimers. The long-range dipolar interactions may affect the exciton wave functions significantly. However, the truncation adopted in the INDO/S-CIS calculations [206, 227] introduced the uncertainties in the results and might lead an overestimation of J_1 and J_2. More accurate calculations on the entire B850 ring are thus desirable.

Ng et al. implemented the LDM at the INDO/S level and employed the resulting INDO/S-LDM method to calculate the low-lying excited-state energies of LH2 aggregates in *Rs. molischianum* [228]. The INDO/S method is well-suited for spectroscopy calculations on LH2. The INDO/S parameters used in these calculations are from Ref. [229] by Zerner et al. The geometry is based on the crystal structure of the *Rs. molischianum* complex [205], obtained from the Protein Data Bank (PDB) of the Research Collaboratory for Structural Bioinformatics (RCSB) with the PDB identification code 1LGH. Hydrogen atoms are added using the Insight II software, and their coordinates are optimized with the semiempirical PM3 [184] method. All other atoms were fixed at their crystal structure coordinates. The ZINDO method [230–232] is employed to generate the ground-state density matrices and Fock matrices. The INDO/S-LDM method is then employed to calculate the absorption spectra.

4.4.2.1. Absorption Spectrum and Dipole-Induced Excited States

4.4.2.1.1. Dimers and Protein/Carotenoid Environment Influence of the protein environment and energetics and dynamics of carotenoids in various species of purple bacteria attracted much experimental and theoretical interest [233–235]. Proteins in LH2 are generally believed to provide only structural support and do not significantly affect the electronic structures. Carotenoids absorb light at about 2.5 eV, and therefore do not intervene in the low-lying excitations. These issues are examined by the calculations. In Fig. 17a and 17b, the absorption spectra of isolated 1α-1β dimer, 1α-1β dimer with the protein moiety, 1α-1β dimer with the protein moiety, and carotenoid are compared. The corresponding structure is shown in Fig. 18. To facilitate truncations in the computation, the system will be divided into subsystems as follows: for dimers, each BChl-a represents one subsystem; for the proteins, each amino acid segment represents one subsystem; for the carotenoid, the whole chain is divided into two parts, and hence the part which is far away from the dimer contains 39 atoms whereas the part closer to the dimer contains 57 atoms. For the latter two calculations,

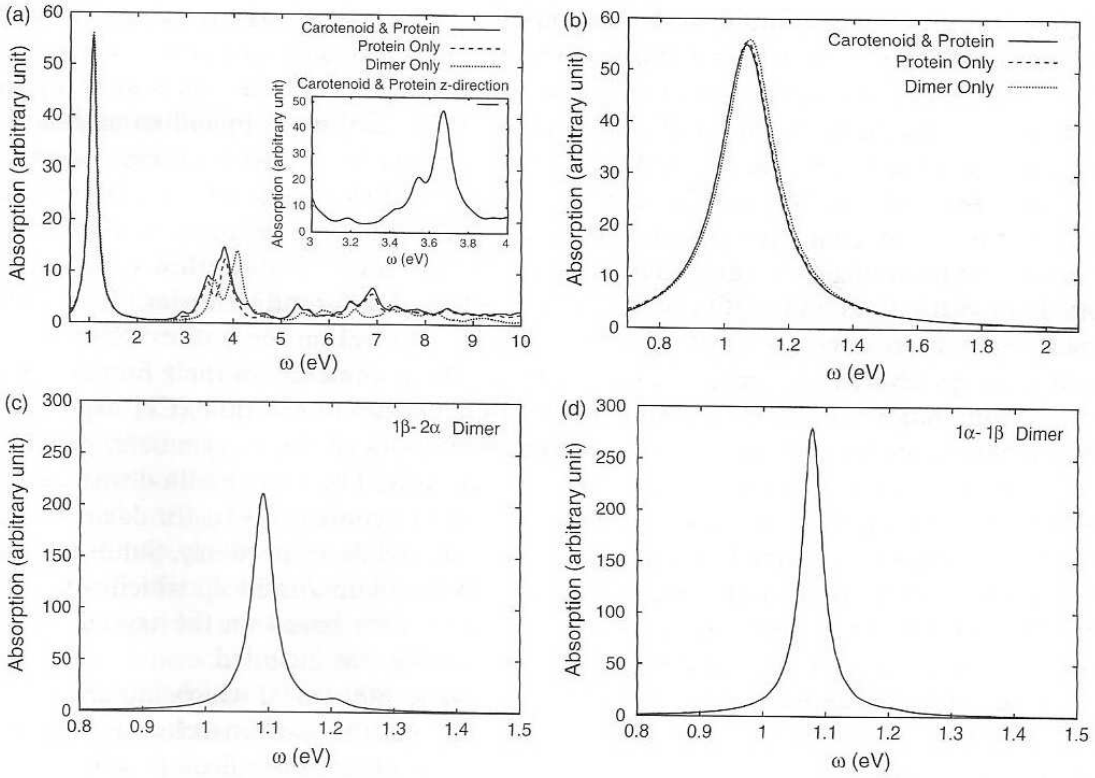

Figure 17. (a) and (b) compare three calculations on the 1α-1β dimer with and without a protein environment. (I) Dimer calculation with a protein environment and the carotenoid. (II) Dimer calculation with a protein environment only. (III) Dimer calculation only. Note that the Q_y excitation spectrum does not change significantly. The inset in (a) shows the absorption peak of carotenoid at about 3.6 eV. In (b), only an insignificant red shift of the Q_y transition is found with the protein environment included in the calculation. The absorption spectrum of (c) 1β-2α dimer, (d) 1α-1β dimer. The first Q_y transition splits into two levels with the Q_{y_1} peak carrying most of the oscillator strength. Reprinted with permission from [228], M. F. Ng et al., *J. Phys. Chem. B* 107, 9589 (2003). © 2003, American Chemical Society.

the α and β apoproteins were cut to retain a range of segments that are close to the dimer. Then, a cutoff length of 10 Å was applied in these two calculations so that each BChl-a would include another BChl-a and also some parts of the protein and the carotenoid in the calculation. It is found that the Q_{y_1} and Q_{y_2} transitions are red shifted insignificantly to nearly the same extent with the added protein environment (<0.01 eV), as shown in Fig. 17b. This implies that proteins and carotenoids can be neglected for the Q band calculation.

Figure 17c and 17d displays the absorption spectra of the 1β-2α and 1α-1β dimers, respectively. Because of their different Mg-to-Mg distances and inter-monomer angles, we obtain quite different absorption energies, Davydov splittings [200, 236], and intermonomer coupling energy. The absorption energies for Q_{y_1} and Q_{y_2} for 1α-1β (1β-2α) dimer are 1.08 eV and 1.21 eV (1.09 eV and 1.21 eV), respectively (cf. Table 5). It follows that the electronic splitting for 1α-1β (1β-2α) dimer is 0.13 eV (0.11 eV). These values are larger than those from Ref. [225] (0.10 eV and 0.09 eV for 1α-1β dimer and 1β-2α dimer, respectively). The discrepancies may be attributed to different BChls-a truncation sizes. Ng et al. take into account only 46 atoms for each BChl-a. Besides, the original INDO/S parameterization was based on a CI calculation with a truncated active space [237]. In the LDM method, the complete active space is considered and the calculated Q_y excitation in a BChl-a molecule using the original parameterization is blue-shifted to below 1 eV. The original parameterization may not reproduce the experimental spectral peaks well if a large active space is considered. Hence, Ng et al. adopted the parameters of Ref. [229], which can reproduce much better measured spectral peaks of Q_y and Q_x excitations in a BChl-a molecule. The main difference between these two sets of parameters is the bonding parameter (β), which is an empirical parameter (cf. Ref. [229] and Ref. [232]). Despite the discrepancies, the results agree with Ref. [225] on that the 1α-1β has a larger coupling constant as a result of their parallel arrangements despite of a longer Mg-to-Mg distance.

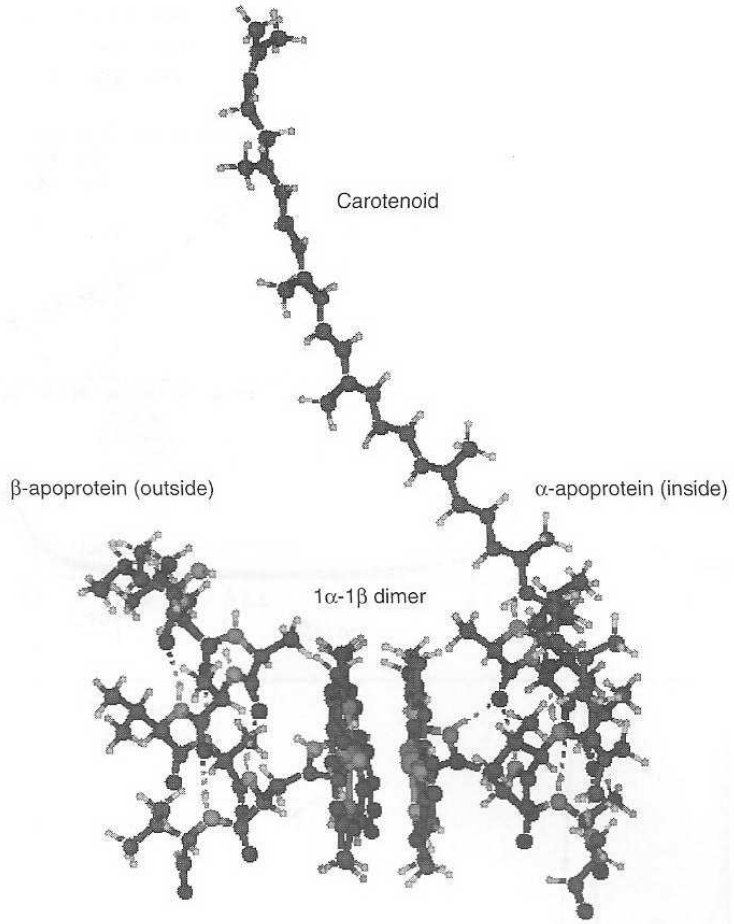

Figure 18. The structure of the 1α-1β dimer with surrounding proteins and the carotenoid. Parts of the proteins within 10 Å are included in the calculation. Reprinted with permission from [228], M. F. Ng et al., *J. Phys. Chem. B* 107, 9589 (2003). © 2003, American Chemical Society.

◇ *Trimer, Pentamer, and Cutoff Length*

To determine an appropriate cutoff length for calculations of the B800 and B850 rings, calculations were carried out on trimers and pentamers with and without the cutoffs. In both calculations, each BChl-a represents one subsystem. For the B800 ring, a cutoff length was chosen so that only the nearest-neighbors of BChls-a were included. As the Mg-to-Mg distance for the nearest BChl-a in the B800 ring is about 22 Å, a cutoff length of 30 Å is taken for the B800 ring. In contrast, for the B850 ring, the choice of the cutoff length has been examined by the trimer and pentamer calculations.

Figure 19 compares the absorption spectra of the trimer and the pentamer with and without cutoffs. The Q_y excitation energies are found to be the same for both the trimer and the pentamer with and without cutoffs (1.04 and 0.99 eV for the trimer and the pentamer, respectively; and the cutoff length is set to be 15 Å). Therefore, coherence between next-neighbor BChls-a is included in the density matrix, which is truncated by the 15-Å cutoff length.

Table 5. Q_y and Q_x excitation energies for the two different dimers in the B850 ring.

Dimer	Q_y(eV)	Q_x(eV)
1α-1β	1.08 Q_{y_1}	1.98 Q_{x_1}
	1.21 Q_{y_2}	2.15 Q_{x_2}
1β-2α	1.09 Q_{y_1}	1.91 Q_{x_1}
	1.21 Q_{y_2}	2.17 Q_{x_2}

Reprinted with permission from [228], M. F. Ng et al., *J. Phys. Chem. B* 107, 9589 (2003). © 2003, American Chemical Society.

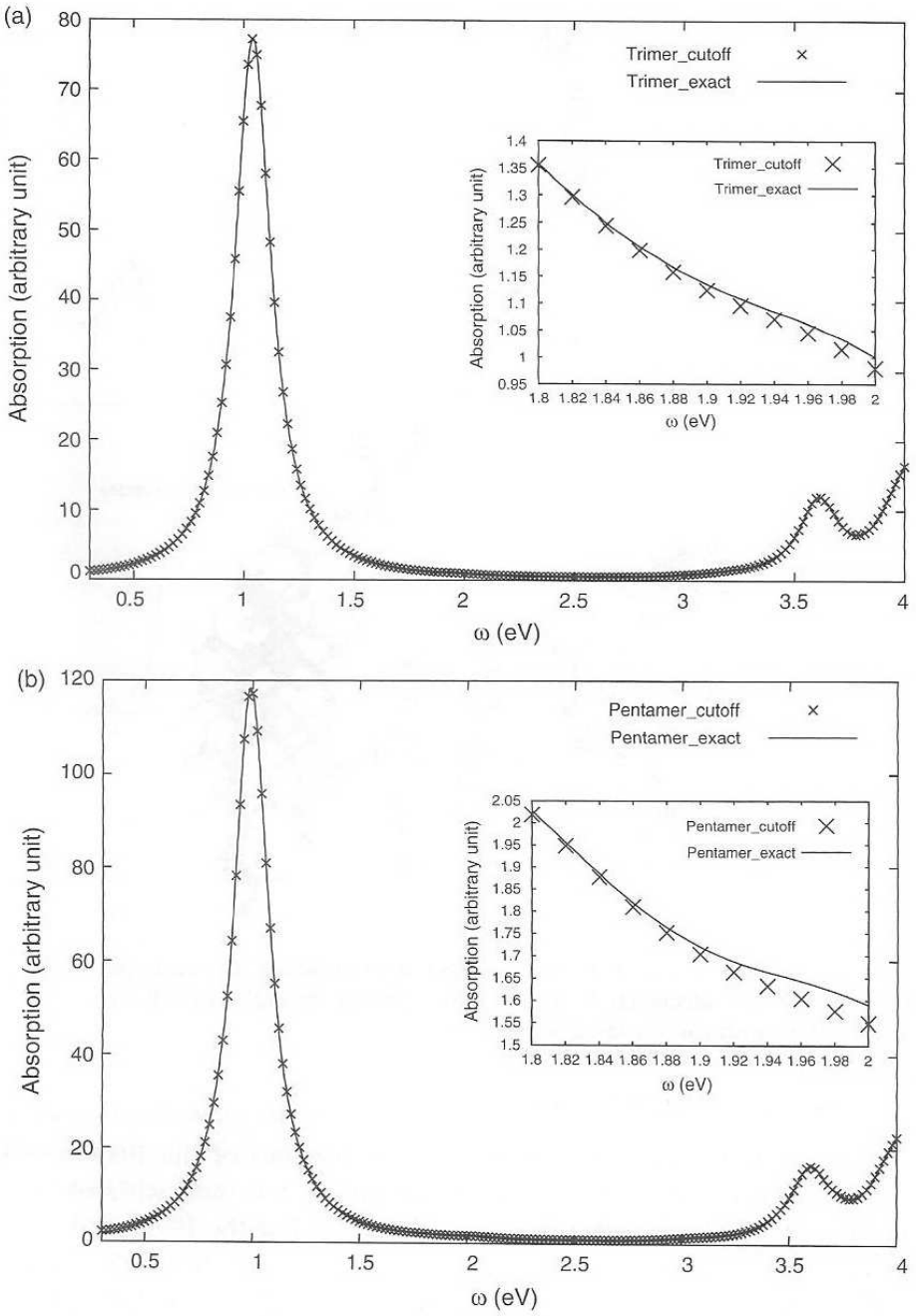

Figure 19. The absorption spectra of (a) a trimer calculation with and without density-matrix truncations (cutoff length = 15 Å). (b) A pentamer calculations with and without density-matrix truncations (cutoff length = 15 Å). The solid line is the exact calculation and the crosses are the results calculated with density-matrix truncations in both (a) and (b). Calculations with and without cutoffs yield nearly identical results. The inset in each plot shows the difference between calculations with and without cutoffs in higher energies. Reprinted with permission from [228], M. F. Ng et al., *J. Phys. Chem. B* 107, 9589 (2003). © 2003, American Chemical Society.

The absorption spectra from calculations with and without cutoffs are nearly identical. Small differences are found for Q_x transition, and peaks at higher energies. Therefore, it is concluded that the Q_y excitation is mainly confined to one to two BChls-a, and the cutoff length of 15 Å is adequate for calculating Q_y and Q_x transitions, and is thus used in the calculation of B850 rings. More important, this shows that the electron–hole distances of Q_y excitons are confined to, at most, two BChls-a.

4.4.2.1.2. The B800 and B850 Rings Figure 20a displays the absorption spectrum of the B800 ring with an applied external field along an in-plane direction. The Q_y and Q_x excitation energies that carry the strongest oscillator strength are 1.16 and 2.26 eV, respectively. If the external electric field is applied in z-direction (see the inset in Fig. 20a), a peak at 1.16 eV is found with small oscillator strength (the lowest-energy state for the B800 ring).

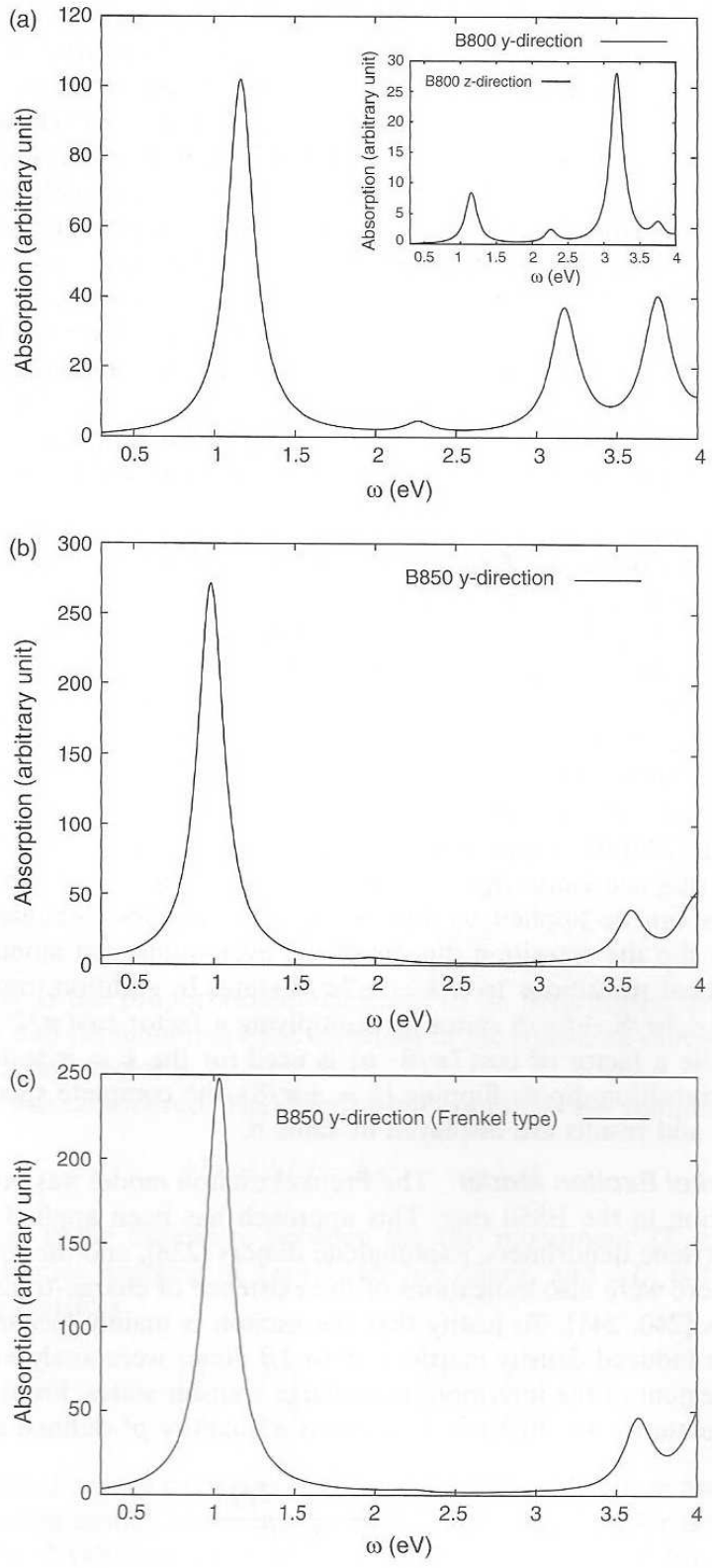

Figure 20. The absorption spectrum of (a) the B800 ring, (b) the B850 ring with a cutoff length of 15 Å, (c) the B850 ring with a cutoff length of 1 Å. The corresponding directions of transition dipole are depicted in Fig. 16. The inset in (a) shows the z-direction excitation of the B800 ring. Reprinted with permission from [228], M. F. Ng et al., *J. Phys. Chem. B* 107, 9589 (2003). © 2003, American Chemical Society.

This can be explained by the fact that the transition dipole for each BChl-a is not tangential to the B800 ring. A small component of y-direction dipole can be induced when the electric field is applied in z-direction. As compared with the B800 BChl-a monomer absorption spectrum, the energy of the Q_y transition is slightly red shifted by about 0.02 eV. This can be explained by large spatial separations between individual monomers in the B800 ring.

Figure 20b shows the absorption spectrum of the B850 ring with an applied external field lying in the plane of the B850 ring. The spectrum for the B850 ring does not depend on the direction of the in-plane applied field, as will be explained in the next section. The optically allowed Q_y excitation in the B850 ring is found at 0.98 eV. However, this optically allowed state is not the lowest-energy state in the B850 ring. The lowest-energy state, which is symmetry forbidden, is calculated to be at 0.93 eV, consistent with a trend of red shift as one goes from a monomer to a dimer, a trimer, and a pentamer (1.17, 1.08, 1.04, and 0.99 eV, respectively). Discussions of the selection rule will be given in the next section.

Figure 20c shows the absorption spectrum of the B850 ring calculated with the density matrices truncated to be within one single monomer. With the electron–hole pair confined within one monomer, the dipole-allowed Q_y excitation now has an energy of 1.03 eV, which is blue-shifted by about 0.05 eV from that in the spectrum of Fig. 20b. This implies that the electron–hole pair actually spreads to neighboring BChls-a. It was therefore concluded that the Frenkel exciton model for this system is reasonably good but may require some corrections.

4.4.2.2. The Dipole Forbidden Excited States The B850 ring made of 16 BChls-a is of C_8 symmetry, and there are a total of 16 energy levels. Because of the symmetry and the dimeric nature, the energy levels split into two bands; one band is of higher energy and the other is lower. Each band contains five energy levels, among which three of them are doubly degenerate. The doubly degenerate optically allowed energy states in the lower band have been resolved (cf. Fig. 20b). To investigate the rest of the 14 dipole forbidden energy levels, a fictitious external field is employed to calculate the dipole forbidden excited states. The details of the selection rules for all these energy states can be found in Ref. [228].

As shown in Ref. [228], the flipping of the transition dipoles of the eight monomers in the upper half of the ring can cause dipole-allowed transitions to $k = 0, \pm\pi/4, \pm\pi/2, \pm 3\pi/4$. Similar techniques can be applied to find out other symmetry forbidden transitions. For example, one may flip the transition dipoles of the even-numbered monomers in the B850 ring to obtain optical transitions to a $k = \pm 7\pi/8$ state. In addition, one may also obtain transitions to $k = \pm 3\pi/8, \pm 5\pi/8$ states by multiplying a factor $\cos(\pi/2 \cdot n)$ (where n runs from 1 to 16), while a factor of $\cos(7\pi/8 \cdot n)$ is used for the $k = \pi$ state. Combined with the case with no transition-dipole flipping ($k = \pm\pi/8$), the complete spectrum of the B850 ring was resolved, and results are displayed in Table 6.

4.4.2.3. The Frenkel Exciton Model The Frenkel exciton model was proposed to account for the Q_y excitation in the B850 ring. This approach has been applied for other systems such as phenylacetylene dendrimers, naphthalene dimers [238], and the *Rps. acidophila* LH2 complex [239]. There were also indications of the existence of charge-transfer states in light-harvesting systems [240, 241]. To justify that the exciton is mainly localized in one BChl-a molecule only, the induced density matrices of 1α-1β dimer were analyzed at its Q_y excited state to study the extent of the intermonomer charge transfer states. From the density matrices, Ng et al. calculate for the first two excitations a quantity p^ν defined as

$$p^\nu \equiv \frac{\sum_{ij}^{\text{intermonomer}} |\delta\rho_{ij}^\nu|^2}{\sum_{ij} |\delta\rho_{ij}^\nu|^2} \tag{143}$$

Table 6. Spectrum of the entire B850 ring calculated by the INDO/S-LDM method in an isolated state.

Lower band (cm^{-1})		Upper band (cm^{-1})	
$k = 0$	7468.87	$k = 4\pi/8$	9501.44
$k = \pm\pi/8$	7904.43	$k = \pm 5\pi/8$	9662.76
$k = \pm 2\pi/8$	8517.42	$k = \pm 6\pi/8$	9840.28
$k = \pm 3\pi/8$	8985.23	$k = \pm 7\pi/8$	9920.86
$k = -4\pi/8$	9259.47	$k = \pi$	9977.32

where $\delta\rho_{ij}$ is the field-induced perturbation of the reduced density matrix element (linking orbital i and j) away from its ground-state value $\rho_{ij}^{(0)}$. The sum in the numerator is over the intermonomer components, whereas the sum in the denominator is over all pairs of orbital i and j. The calculated values are presented in Table 7. The fact that p^{ν} is small implies that the excitation is predominantly a Frenkel exciton. From Table 7, for both Q_{y_1} and Q_{y_2} excitations, p^{ν} is 2%.

Schulten and coworkers [206, 227] proposed a more realistic Hamiltonian of the hexadecamer,

$$\hat{H} = \begin{pmatrix} \epsilon_1 & J_1 & W_{1,3} & W_{1,4} & \cdot & W_{1,2N-1} & J_2 \\ J_1 & \epsilon_2 & J_2 & W_{2,4} & \cdot & \cdot & W_{2,2N} \\ W_{3,1} & J_2 & \epsilon_1 & \cdot & \cdot & \cdot & \cdot \\ W_{4,1} & W_{4,2} & \cdot & \cdot & \cdot & \cdot & \cdot \\ \cdot & \cdot & \cdot & \cdot & \epsilon_2 & J_2 & W_{2N-2,2N} \\ \cdot & \cdot & \cdot & \cdot & J_2 & \epsilon_1 & J_1 \\ J_2 & \cdot & \cdot & \cdot & W_{2N,2N-2} & J_1 & \epsilon_2 \end{pmatrix} \tag{144}$$

where ϵ_1 and ϵ_2 are the excitation energies of the Q_y state of an individual BChl-a, J_1 and J_2 are the coupling constants between the nearest-neighbors of the entire ring, and N equals 8 as the system is of C_8 symmetry. In addition to the nearest-neighbor interactions J_1 and J_2, BChls-a, which are not nearest-neighbors, are coupled to each other via dipole–dipole interactions. The matrix $W_{i,j}$ in Eq. (144) is to add dipolar couplings to nonnearest neighbors:

$$W_{i,j} = C\left[\frac{\mathbf{d}_i \cdot \mathbf{d}_j}{|\mathbf{r}_{ij}|^3} - \frac{(\mathbf{d}_i \cdot \mathbf{r}_{ij})(\mathbf{d}_j \cdot \mathbf{r}_{ij})}{|\mathbf{r}_{ij}|^5}\right] \tag{145}$$

where the factor C is the proportionality constant to be determined, and $\mathbf{r}_{ij}$ is the vector connecting the ith and jth monomer. The direction of the transition dipole of the ith BChl-a is represented by a unit vector $\mathbf{d}_i$.

The dimer case was considered. The electronic J couplings are computed from

$$4J_i^2 = \Delta E_i^2 - \Delta\epsilon^2, \quad i = 1, 2 \tag{146}$$

where $\Delta\epsilon = \epsilon_1 - \epsilon_2$ is the difference between the two monomers' Q_y excitation energies, J_1 (J_2) is intermonomer coupling of 1α-1β (1β-2α) dimer, and ΔE_i is the splitting of the eigenvalues of the matrices

$$\begin{pmatrix} \epsilon_1 & J_1 \\ J_1 & \epsilon_2 \end{pmatrix} \quad \text{and} \quad \begin{pmatrix} \epsilon_2 & J_2 \\ J_2 & \epsilon_1 \end{pmatrix} \tag{147}$$

From Eq. (146), the J values calculated are shown in Table 8. These are the values based on the Frenkel exciton model, in which intermonomer charge transfer is not considered.

To determine the J values of the complete B850 ring, one can fit Eq. (144) by a Monte Carlo procedure. An initial guess of the parameters in Eq. (144) is made, and the 16×16 matrix is diagonalized, resulting in 16 eigenstates. As the system is dimerized, the capital K

Table 7. ρ^{ν} values for the first two excitations of the 1α-1β dimer.

1α-1β dimer	Excitation ν (eV)	ρ^{ν}
Q_{y_1}	1.08	0.024
Q_{y_2}	1.21	0.020

Reprinted with permission from [228], M. F. Ng et al., *J. Phys. Chem. B* 107, 9589 (2003). © 2003, American Chemical Society.

Table 8. Calculated J coupling constants (cm^{-1}) for the two dimers in the B850 ring.

	Methods				
J coupling constant	LDM dimer	LDM ring	CEO dimer	ZINDO ring	PDA dimer
1α-1β	528	594	408	790	339
1β-2α	455	491	366	369	336

Reprinted with permission from [228], M. F. Ng et al., *J. Phys. Chem. B* 107, 9589 (2003). © 2003, American Chemical Society.

(instead of k) is used to label the states here. The $K = 0$ and $K = \pi$ states are nondegenerate, and $K = \pm\pi/4$, $\pm 2\pi/4$, and $\pm 3\pi/4$ are doubly degenerate. The energy for each K state is compared with the corresponding energy from the INDO/S-LDM spectra, and the difference is used to calculate the root mean square error for that particular iteration step. The process is repeated until a desired precision is reached. The term ϵ_1 is assumed to be greater than ϵ_2, and they are constrained so that the sum of diagonal elements in Eq. (144) is equal to the sum of the calculated INDO/S-LDM energies, that is,

$$8(\epsilon_1 + \epsilon_2) = \sum_i E_i \tag{148}$$

where E_i is the energy of the ith INDO/S-LDM state. The result is given in Fig. 21(a). The total rms error is about 118 cm^{-1}. The final J_1, J_2, ϵ_1, ϵ_2, and C values are presented in Table 9.

Only two calculations of the entire B850 ring have been reported in the literature, and both used the INDO/S-CIS method [206, 227]. The spectra of the B850 ring calculated via INDO/S-LDM and those via INDO/S-CIS are compared in Fig. 21. In Fig. 21a, the LDM result is represented by crosses, and the fitting result by pluses. In Fig. 21b, the CIS result is shown by crosses and the fitting result by pluses. Note that the INDO/S-CIS method fitted the band edges, that is, the $K = 0$ and $K = \pm\pi$ states, whereas LDM fitted the complete 10 energy levels. The fitting result in Fig. 21a is better in the sense that smaller root mean square error (118 cm^{-1}) is achieved (compare with a root mean square of 258 cm^{-1} in INDO/S-CIS method).

From the B850 ring fitting (cf. Table 9), we note that both ϵ_1 and ϵ_2 become smaller, and their difference vanishes. The reason can be analyzed by calculating the ground-state dipolar field acting on a specific α-BChl-a or a β-BChl-a because of its non-nearest neighbors. To calculate the dipole fields

$$\mathbf{E}(\mathbf{x}) = \frac{3\mathbf{n}(\mathbf{p}\cdot\mathbf{n}) - \mathbf{p}}{|\mathbf{x} - \mathbf{x}_0|^3} \tag{149}$$

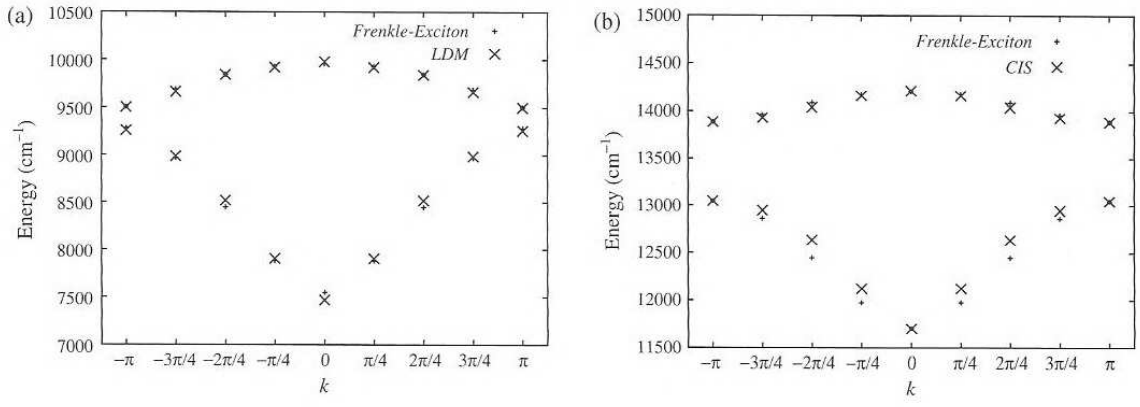

Figure 21. (a) Ten energy levels extracted from the absorption spectra (cross) and the correspondingly fitted 10 eigenvalues from a dimerized Hamiltonian with additional dipolar interactions between nonnearest BChl-a neighbors (plus); the fitting parameters are $J_1 = 593.9$ cm^{-1}, $J_2 = 490.6$ cm^{-1}, $\epsilon_1 = 9116.9$ cm^{-1}, $\epsilon_2 = 9116.7$ cm^{-1}, and $C = 640725$ $Å^3 cm^{-1}$. The x-axis is labeled by the crystal momenta of the exciton $p = \pm K\pi/4$. (b) Excitation energies calculated by the INDO/S-CIS method and their fittings. Reprinted with permission from [228], M. F. Ng et al., *J. Phys. Chem. B* 107, 9589 (2003). © 2003, American Chemical Society.

Table 9. Fitting parameters for the B850 ring (cm^{-1}).

	J_1	J_2	ϵ_1	ϵ_2	C/Å^3	rms
The B850 ring	593.9	490.6	9116.9	9116.7	640725	118

is employed, where **E** is the dipole field at a point **x** resulting from a ground-state dipole **p** at the point $\mathbf{x}_0$. A summation is carried out for the dipole effect acting on an α-BChl-a and β-BChl-a, respectively. The summations of dipoles acting on the α-BChl-a and β-BChl-a are estimated to be 8.0×10^{-4} Å^{-2} and 9.8×10^{-4} Å^{-2}, respectively. The energy E is calculated by

$$E = -\mathbf{E} \cdot \vec{\mathbf{d}} \tag{150}$$

where $\vec{d}$ is the transition dipole for that particular α and β BChls-a. As a result, the energies acting on the α and β BChls-a because of the ground-state dipole of the rest of BChls-a in the B850 ring except its nearest neighbor are $-194 cm^{-1}$ and $-153 cm^{-1}$, respectively. Ng et al. thus determined that the net effect of the field dipole of the rest of the BChls-a acting on the α-BChl-a is larger than that on the β-BChl-a. This helps to explain qualitatively why the ϵ_1 and ϵ_2 values of the B850 ring have a vanishing difference. The J_1 and J_2 values determined from the INDO/S-CIS calculations on the B850 ring [206, 227] are very different from those from the dimer calculations. The J_1 and J_2 values fitted from the INDO/S-LDM calculation of the B850 ring are similar to those from the INDO/S-LDM dimer calculation of dimers. The INDO/S-LDM calculations here thus resolve the long-existing discrepancy. The fact that the J_1 and J_2 values in Table 9 are larger than those in Refs. [225, 226] and [209] can be attributed to long-range dipolar interactions in the ring and the INDO/S parameterization.

To further justify the value of C, the transition dipole moment of the monomer Q_y state is calculated using the formula [225]

$$\mu^{\nu} = Tr(\delta\rho^{\nu}_{i,j} \cdot \mu_{i,j}) \tag{151}$$

where μ^{ν} is the transition dipole at excitation ν, $\mu_{i,j}$ is the dipole moment operator, and $\delta\rho^{\nu}_{i,j}$ is the induced density matrix at excitation ν obtained from a Fourier transform

$$\delta\rho(\omega) = \int dt \exp^{i\omega t} \delta\rho(t) \tag{152}$$

where ω is the excited-state frequency, $\delta\rho(\omega)$ and $\delta\rho(t)$ are the frequency-domain- and time-domain-induced density matrices when $|\mathbf{E}| = 1$ V/Å, respectively. The normalized frequency-domain-induced density matrix takes the form $\{\mathrm{Im}[\delta\rho(\omega)] + \mathrm{Im}[\delta\rho^{\mathrm{T}}(\omega)]\}/\mathrm{i}\sqrt{2}$, where $\delta\rho^{T}(\omega)$ is the transpose of $\delta\rho(\omega)$. The transition dipole moment was calculated to be 2.326 eÅ. Based on Eq. (145), a relation between the transition dipole moment and C value was established

$$\mu^2 \times 1.16 \times 10^5 = C \tag{153}$$

from which $C = 639765$ Å^3 cm^{-1} is obtained. This is consistent with the fitting result for the entire B850 ring (640725 Å^3 cm^{-1}).

5. CONCLUSION

Linear-scaling electronic structure methods are particularly suitable to simulate the electric, optical, and magnetic properties of nanomaterials. So far, these methods have not been applied extensively to study the physical properties of nanostructures. One major reason is that researchers in the field are often interested in the optical, transport, and magnetic properties of nanoscopic materials. These properties relate to the excited states of these complex systems, whereas most of the linear-scaling electronic structure methods are for

the electronic ground state only. There has been a proliferation of linear-scaling ground-state electronic structure methods that have been tested on the model molecular systems. However, application to nanomaterials has been rare [242, 243]. The LDM method has been the only linear-scaling quantum mechanical method that explicitly treats electron–electron interaction for excited states and that has been applied to nanoscopic systems, such as LH2 [228], PPV aggregates [197], carbon nanotubes [62, 142, 244], and nanowires [245]. With its successful combining with TDDFT [127, 128], the LDM method can be potentially applied to a much wider range of complex systems. The remaining challenge is to construct an accurate XC functional for TDDFT [246, 247]. The applications reviewed here are a few of many successful cases. We refer to Refs. [62, 142, 242–244, 248–252] for more successful applications of $O(N)$ methods to nanoscopic and biological systems.

Another important feature of all the linear-scaling methods is that they can be readily implemented for parallel computation [40, 253, 254], as the physical basis of linear-scaling computing is the locality of the density matrix. Implementation for parallel computing is expected to enhance drastically the efficiency of these methods. With the wide availability of computer clusters, linear-scaling electronic structure calculations are playing increasingly important roles in studying nanoscopic systems.

With all these exciting promises, problems do remain for linear-scaling electronic structure methods, such as a large prefactor and accuracy. Linear-scaling methods have been very successful for low-dimensional systems. For three-dimensional systems, there are usually too many atoms within the localization region. Several linear-scaling methods are based on empirical or semiempirical models and are thus not as accurate and cannot be applied to wide range of materials. Another challenge is to apply linear-scaling methods to open systems. All these problems of $O(N)$ method, however are technical, can be either solved by improving methodologies or will be rendered as unimportant when computers become even faster. With all intrinsic obstacles removed, linear-scaling electronic structure methods are deemed to become essential tools in the research and development of nanotechnology, materials design, and drug discovery.

ACKNOWLEDGMENTS

We thank Dr. Satoshi Yokojima, Dr. Yang Zhao, Dr. WanZhen Liang, Dr. Xiujun Wang, and Dr. ManFai Ng for help and discussion. Support from the Hong Kong Research Grant Council (RCG) and the Committee for Research and Conference Grants (CRCG) of the University of Hong Kong is gratefully acknowledged.

REFERENCES

1. M. Head-Gordon, *J. Phys. Chem.* 100, 13213 (1996).
2. W. Kohn and L. J. Sham, *Phys. Rev.* 140, A1133 (1965).
3. C. Møller and M. S. Plesset, *Phys. Rev.* 46, 618 (1934).
4. J. A. Pople, R. Krishnan, H. B. Schlegel, and J. S. Binkley, *Int. J. Quant. Chem.* 14, 545 (1978).
5. W. Yang, *Phys. Rev. Lett.* 66, 1438 (1991).
6. W. Yang and T. S. Lee, *J. Chem. Phys.* 103, 5674 (1995).
7. A. P. Cortona, *Phys. Rev. B* 44, 8454 (1991).
8. G. Galli and M. Parrinello, *Phys. Rev. Lett.* 69, 3547 (1992).
9. S. Baroni and P. Giannozzi, *Europhys. Lett.* 17, 547 (1992).
10. X.-P. Li, R. W. Nunes, and D. Vanderbilt, *Phys. Rev. B* 47, 10891 (1993).
11. M. S. Daw, *Phys. Rev. B* 47, 10895 (1993).
12. F. Mauri, G. Galli, and R. Car, *Phys. Rev. B* 47, 9973 (1993).
13. P. Ordejón, D. A. Drabold, M. P. Grumbach, and R. M. Martin, *Phys. Rev. B* 48, 14646 (1993).
14. W. Kohn, *Chem. Phys. Lett.* 208, 167 (1993).
15. D. A. Drabold and O. F. Sankey, *Phys. Rev. Lett.* 70, 3631 (1993).
16. W. Zhong, D. Tománek, and G. F. Bertsch, *Solid State Commun.* 86, 607 (1993).
17. A. Gibson, R. Haydock, and J. P. LaFemina, *Phys. Rev. B* 47, 9229 (1993).
18. M. Aoki, *Phys. Rev. Lett.* 71, 3842 (1993).
19. E. B. Stechel, A. P. Williams, and P. J. Feibelman, *Phys. Rev. B* 49, 10088 (1994).
20. S. Goedecker and L. Colombo, *Phys. Rev. Lett.* 73, 122 (1994); S. Goedecker and M. Teter, *Phys. Rev. B* 51, 9455 (1995).

21. S.-Y. Qiu, C. Z. Wang, K. M. Ho, and C. T. Chan, *J. Phys. Condens. Matter* 6, 9153 (1994).
22. J. J. P. Stewart, *Int. J. Quantum Chem.* 58, 133 (1995).
23. X. Chen, J.-M. Langlois, and W. A. Goddard III, *Phys. Rev. B* 52, 2348 (1995).
24. E. Hernandez and M. J. Gillan, *Phys. Rev. B* 51, 10157 (1995).
25. M. C. Strain, G. E. Scuseria, and M. J. Frisch, *Science* 271, 51 (1996).
26. S. L. Dixon and K. M. Merz, *J. Chem. Phys.* 104, 6643 (1996).
27. P. Ordejón, E. Artacho, and J. M. Soler, *Phys. Rev. B* 53, 10441 (1996).
28. E. Schwegler, M. Challacombe, and M. Head-Gordon, *J. Chem. Phys.* 106, 9708 (1997).
29. F. Merzel, *Int. J. Quantum Chem.* 96, 554 (2004).
30. X. S. Li, J. M. Millam, G. E. Scuseria, M. J. Frisch, and H. B. Schlegel, *J. Chem. Phys.* 119, 7651 (2003).
31. C. Saravanan, Y. Shao, R. Baer, P. N. Ross, and M. Head-Gordon, *J. Comp. Chem.* 24, 618 (2003).
32. P. D. Haynes and M. C. Payne, *Phys. Rev. B* 59, 12173 (1999).
33. D. SanchezPortal, P. Ordejon, E. Artacho, and J. M. Soler, Int. *J. Quan. Chem.* 65, 453 (1997).
34. E. Hernandez, M. J. Gillan, and C. M. Goringe, *Phys. Rev. B* 53, 7147 (1996).
35. M. Challacombe, *J. Chem. Phys.* 110, 2332 (1999).
36. R. Baer and M. Head-Gordon, *Phys. Rev. B* 58, 15296 (1998).
37. B. G. Janesko and D. Yaron, *J. Chem. Phys.* 119, 1320 (2003).
38. A. F. Voter, J. D. Kress, and R. N. Silver *Phys. Rev. B* 53, 12733 (1996).
39. For review, see S. Goedecker, *Rev. Mod. Phys.* 71, 1085 (1999).
40. D. R. Bowler, T. Miyazaki, and M. J. Gillan, *J. Phys.-Condens. Mat.* 14, 2781 (2002).
41. P. Ordejon, *Phys. Status Solidi B* 217, 335 (2000).
42. M. Schutz, *Phys. Chem. Chem. Phys.* 4, 3941 (2002).
43. S. H. Li, J. Ma, and Y. S. Jiang, *J. Comp. Chem.* 23, 237 (2002).
44. G. E. Scuseria and P. Y. Ayala, *J. Chem. Phys.* 111, 8330 (1999).
45. H. J. Werner, F. R. Manby, and P. J. Knowles, *J. Chem. Phys.* 118, 8149 (2003).
46. S. Saebo and P. Pulay, *J. Chem. Phys.* 115, 3975 (2001).
47. P. Y. Ayala and G. E. Scuseria, *J. Chem. Phys.* 110, 3660 (1999).
48. S. Manten and A. Luchow, *J. Chem. Phys.* 119, 1307 (2003).
49. A. J. Williamson, R. Q. Hood, and J. C. Grossman, *Phys. Rev. Lett.* 87, 246406 (2001).
50. S. R. Billeter, A. Curioni, and W. Andreoni, *Comp. Mater. Sci.* 27, 437 (2003).
51. S. R. Billeter, A. J. Turner, and W. Thiel, *Phys. Chem. Chem. Phys.* 2, 2177 (2000).
52. K. Nemeth, O. Coulaud, G. Monard, and J. G. Angyan, *J. Chem. Phys.* 113, 5598 (2000).
53. W. Kohn, *Phys. Rev. Lett.* 76, 3168 (1996).
54. T. Iitaka, S. Nomura, H. Hirayama, X. Zhao, Y. Aoyagi, and T. Sugano, *Phys. Rev. E* 56, 1222 (1997).
55. T. Nakayama and H. Shima, *Phys. Rev. E* 58, 3984 (1998).
56. R. W. Nunes and D. Vanderbilt, *Phys. Rev. Lett.* 73, 712 (1994).
57. A. Dal Corso and F. Mauri, *Phys. Rev. B* 50, 5756 (1994).
58. S. Yokojima and G. H. Chen, *Chem. Phys. Lett.* 292, 379 (1998).
59. S. Yokojima and G. H. Chen, *Phys. Rev. B* 59, 7259 (1999).
60. W. Z. Liang, S. Yokojima, and G. H. Chen, *J. Chem. Phys.* 110, 1844 (1999).
61. S. Yokojima, X. J. Wang, D. H. Zhou, and G. H. Chen, *J. Chem. Phys.* 111, 10444 (1999).
62. W. Z. Liang, S. Yokojima, D. H. Zhou, and G. H. Chen, *J. Phys. Chem. A* 104, 2445 (2000).
63. W. Z. Liang, S. Yokojima, and G. H. Chen, *J. Chem. Phys.* 113, 1403 (2000).
64. G. H. Chen and S. Mukamel, *J. Phys. Chem.* 100, 11080 (1996).
65. G. H. Chen and S. Mukamel, *J. Am. Chem. Soc.* 117, 4945 (1995).
66. W. Kohn, *Phys. Rev.* 115, 809 (1959).
67. W. Kohn, *Phys. Rev. B* 7, 4388 (1973).
68. Des Cloizeaux, *J. Phys. Rev.* 129, 554 (1963); Des Cloizeaux, *J. Phys. Rev. A* 135, 685 (1964); 135, 698 (1964).
69. P. E. Maslen, C. Ochsenfeld, C. A. White, M. S. Lee, and M. Head-Gordon, *J. Phys. Chem. A* 102, 2215 (1998).
70. S. Ismail-Beigi, T. A. Arias, *Phys. Rev. Lett.* 82, 2127 (1999).
71. R. McWeeny, *Rev. Mod. Phys.* 32, 335 (1960).
72. J. Kim, F. Mauri, and G. Galli, *Phys. Rev. B* 52, 1640 (1995).
73. U. Stephan and D. A. Drabold, *Phys. Rev. B* 57, 6391 (1998).
74. W. H. Press, B. P. Flannery, S. A. Teukolsky, and W. T. Vetterling, "Numerical Recipes in C." Cambridge Univ. Press, New York, 1988.
75. S. Goedecker, *J. Comput. Phys.* 118, 261 (1995).
76. W. Hierse and E. Stechel, *Phys. Rev. B* 50, 17811 (1994); E. Hernandez and M. Gilan, *Phys. Rev. B* 51, 10157 (1995).
77. R. Haydock, *Solid State Phys.* 35, 215 (1980).
78. A. Horsfield, A. Bratkovsky, D. Pettifor, and M. Aoki, *Phys. Rev. B* 53, 1656 (1996); A. Horsfield, A. Bratkovsky, M. Fearn, D. Pettifor, and M. Aoki, *Phys. Rev. B* 53, 12694 (1996).
79. D. Bowler, M. Aoki, C. Goringe, A. Horsfield, and D. Pettifor, *Modell. Simul. Mater. Sci. Eng.* 5, 199 (1997).
80. L.-W. Wang, *Phys. Rev. B* 49, 10154 (1994).
81. R. Silver and H. Roeder, *Phys. Rev. E* 56, 4822 (1997).
82. J. J. P. Stewart, P. Csaszar, and P. Pulay, *J. Comput. Chem.* 39, 4997 (1982).
83. Y. Wang, G. M. Stocks, W. A. Shelton, D. M. C. Nicholson, Z. Szotek, and W. M. Temmerman, *Phys. Rev. Lett.* 75, 2867 (1995).

84. W. Z. Liang, C. Saravanan, Y. H. Shao, R. Baer, A. T. Bell, and M. Head-Gordon, *J. Chem. Phys.* 119, 4117 (2003).
85. L. Greengard, *Science* 265, 909 (1994).
86. H. Q. Ding, N. Karasawa, and W. A. Goddard III, *Chem. Phys. Lett.* 196, 6 (1992).
87. H. Q. Ding, N. Karasawa, and W. A. Goddard III, *J. Chem. Phys.* 97, 4309 (1992).
88. C. A. White, B. G. Johnson, P. M. W. Gill, and M. Head-Gordon, *Chem. Phys. Lett.* 230, 8 (1994); C. A. White, B. G. Johnson, P. M. W. Gill, and M. Head-Gordon, *Chem. Phys. Lett.* 253, 268 (1996).
89. F. R. Manby and P. J. Knowles, *Phys. Rev. Lett.* 87, 163001 (2001).
90. L. Füsti-Molnár and P. Pulay, *J. Mol. Struc-Theochem.* 666, 25 (2003).
91. G. E. Scuseria, *J. Phys. Chem. A* 103, 4782 (1999).
92. R. E. Stratmann, G. E. Scuseria, and M. J. Frisch, *Chem. Phys. Lett.* 257, 213 (1996).
93. W. Z. Liang, Y. H. Shao, C. Ochsenfeld, A. T. Bell, and M. Head-Gordon, *Chem. Phys. Lett.* 358, 43 (2002).
94. E. Schwegler and M. Challacombe, *Theor. Chem. Acc.* 104, 344 (2000).
95. J. C. Burant, G. E. Scuseria, and M. J. Frisch, *J. Chem. Phys.* 105, 8969 (1996).
96. N. A. Anikin, V. L. Bugaenko, M. V. Frash, and J. Leszczynski, *J. Comp. Chem.* 24, 1132 (2003).
97. E. Anglada, J. M. Soler, J. Junquera, and E. Artacho, *Phys. Rev. B* 66, 205101 (2002).
98. G. Berghold, M. Parrinello, and J. Hutter, *J. Chem. Phys.* 116, 1800 (2002).
99. M. S. Lee and M. Head-Gordon, *J. Chem. Phys.* 107, 9085 (1997).
100. J. Junquera, O. Paz, D. Sanchez-Portal, and E. Artacho, *Phys. Rev. B* 64, 235111 (2001).
101. G. Berghold, C. J. Mundy, A. H. Romero, J. Hutter, and M. Parrinello, *Phys. Rev. B* 61 10040 (2000).
102. E. Hernandez, M. J. Gillan, and C. M. Goringe, *Phys. Rev. B* 55, 13485 (1997).
103. S. Goedecker and O. V. Ivanov, *Solid State Commun.* 105, 665 (1998).
104. R. H. Baughman, A. A. Zakhidov, and W. A. de Heer, *Science*, 297, 788 (2002).
105. J.-M. Bonard, K. A. Dean, B. F. Coll, and C. Klinke, *Phys. Rev. Lett.* 89, 197602 (2002).
106. J. W. Gadzuk and E. W. Plummer, *Rev. Mod. Phys.* 45, 487 (1973).
107. R. B. Sharma, V. N. Tondare, D. S. Joag, A. Govindaraj, and C. N. R. Rao, *Chem. Phys. Lett.* 344, 283 (2001).
108. P. G. Collins and A. Zettl, *Phys. Rev. B* 55, 9391 (1997).
109. J. Luo, L.-M. Peng, Z. Q. Xue, and J. L. Wu, *Phys. Rev. B* 66, 155407 (2002).
110. S. Han and M. H. Lee, J. Ihm, *Phys. Rev. B* 65, 085405 (2002).
111. G. Zhou, W. H. Duan, and B. L. Gu, *Phys. Rev. Lett.* 87, 095504 (2001).
112. N. D. Lang and W. Kohn, *Phys. Rev. B* 1, 4555 (1970).
113. A. Warshel and M. Levitt, *J. Mol. Biol.* 103, 227 (1976).
114. X. Zheng, G. H. Chen, Z. Li, S. Deng, and X. S. Xu, *Phys. Rev. Lett.* 92, 106803 (2004).
115. A. M. Rao, E. Richter, S. Bandow, B. Chase, P. C. Eklund, K. A. Williams, S. Fang, K. R. Subbaswamy, M. Menon, A. Thess, R. E. Smalley, G. Dresselhaus, and M. S. Dresselhaus, *Science* 275, 187 (1997).
116. (a) X. Blase, L. X. Benedict, E. Shirley, and S. G. Louie, *Phys. Rev. Lett.* 72, 1878 (1994);
(b) R. A. Jishi, J. Bragin, and L. Lou, *Phys. Rev. B* 59, 9862 (1999).
117. J. W. G. Wildoer, L. C. Venema, A. G. Rinzler, R. E. Smalley, and C. Dekker, *Nature* 391, 59 (1998).
118. M. J. S. Dewar and W. Thiel, *J. Am. Chem. Soc.* 99, 4899 (1977).
119. J. Zhao, J. Han, and J. P. Lu, *Phys. Rev. B* 65, 193401 (2002).
120. J. Cumings, A. Zettl, M. R. McCartney, and J. C. H. Spence, *Phys. Rev. Lett.* 88, 056804 (2002).
121. A. Modinos, "Field, Thermionic, and Secondary Electron Emission Spectroscopy." Plenum Press, New York, 1984.
122. P. Ring and P. Schuck, "The Nuclear Many-Body Problem." Springer, New York, 1980.
123. A. Takahashi and S. Mukamel, *J. Chem. Phys.* 100, 2366 (1994).
124. (a) P. Pariser and R. G. Parr, *J. Chem. Phys.* 21, 767 (1953);
(b) J. A. Pople, *Trans. Faraday Soc.* 49, 1375 (1953).
125. K. Ohno, Theoret. *Chem. Acta* 2, 219 (1964).
126. S. Yokojima, D. H. Zhou, and G. H. Chen, *Chem. Phys. Lett.* 302, 495 (1999).
127. C. Y. Yam, S. Yokojima, and G. H. Chen, *Phys. Rev. B*, 68, 153105 (2003).
128. C. Y. Yam, S. Yokojima, and G. H. Chen, *J. Chem. Phys.* 119, 8794 (2003).
129. J. M. Millam and G. E. Scuseria, *J. Chem. Phys.* 106, 5569 (1997).
130. S. M. Colwell, N. C. Handy, and A. M. Lee, *Phys. Rev. A* 53, 1316 (1996).
131. A. D. Becke, *J. Chem. Phys.* 88, 2547 (1988).
132. W. Kemp, "Organic Spectroscopy." Macmillan, London, 1991.
133. E. Deumens, A. Diz, R. Longo, and Y. Öhrn, *Rev. Mod. Phys.* 66, 917 (1994).
134. J. Morales, A. Diz, E. Deumens, and Y. Öhrn, *J. Chem. Phys.* 103, 9968 (1995).
135. J. Broeckhove, M. D. Coutinho-Neto, E. Deumens, and Y. Öhrn, *Phys. Rev. A* 56, 4996 (1997).
136. M. J. Field, *J. Chem. Phys.* 96, 4583 (1992).
137. (a) J. C. Tully and R. K. Preston, *J. Chem. Phys.* 55, 562 (1971);
(b) J. C. Tully, *J. Chem. Phys.* 93, 1061 (1990);
(c) D. Kohen, F. H. Stillinger, and J. C. Tully, *J. Chem. Phys.* 109, 4713 (1998).
138. (a) W. H. Miller and T. F. George, *J. Chem. Phys.* 56, 5637 (1972);
(b) W. H. Miller and C. W. McCurdy, *J. Chem. Phys.* 69, 5163 (1978);
(c) H.-D. Meyer and W. H. Miller, *J. Chem. Phys.* 70, 3214 (1979); 71, 2156 (1979).
139. G. Stock, *J. Chem. Phys.* 103, 1561 (1995); 103, 2888 (1995).

140. (a) P. A. M. Dirac, Proc. Cambridge, *Phil. Soc.* 26, 376 (1930);
(b) J. Frenkel, "Wave Mechanics." Oxford Univ. Press, Oxford, 1934.
141. J. Del Bene and H. H. Jaffé, *J. Chem. Phys.* 48, 1807 (1968); 48, 4050 (1968).
142. W. Z. Liang, X. J. Wang, S. Yokojima, and G. H. Chen, *J. Am. Chem. Soc.* 122, 11129 (2000).
143. Y. Zhao, S. Yokojima, and G. H. Chen, *J. Chem. Phys.* 113, 4016 (2000).
144. R. J. Glauber, *Phys. Rev.* 131, 2766 (1963).
145. E. J. Heller, *J. Chem. Phys.* 62, 1544 (1975); 65, 4979 (1976); 75, 2923 (1981).
146. J. R. Reimers and E. J. Heller, *J. Phys. Chem.* 92, 3225 (1988).
147. V. Chernyak and S. Mukamel, *J. Chem. Phys.* 105, 4565 (1996).
148. C. W. Gardiner, "Handbook of Stochastic Methods." Springer, Berlin, 1983.
149. S. Carusotto, *Phys. Rev. A* 11, 1397 (1975).
150. C. M. Savage and D. F. Walls, *Phys. Rev. A* 32, 2316 (1985).
151. Y. Zhao, D. W. Brown, and K. Lindenberg, *J. Chem. Phys.* 107, 3159 (1997); 107, 3179 (1997); 106, 2728 (1997); 106, 5622 (1997).
152. F. Bloch, *Phys. Rev.* 105, 1206 (1957).
153. A. G. Redfield, *Adv. Magn. Reson.* 1, 1 (1965).
154. A. Suárez, R. Silbey, and I. Oppenheim, *J. Chem. Phys.* 97, 5101 (1992).
155. W. T. Polland and R. A. Friesner, *J. Chem. Phys.* 100, 5054 (1994).
156. W. T. Pollard, A. K. Felts, and R. A. Friesner, *Adv. Chem. Phys.* 93, 77 (1996).
157. J. Cao, *J. Chem. Phys.* 107, 3204 (1997).
158. Y. J. Yan, F. Shuang, R. X. Xu, J. X. Cheng, X. Q. Li, C. Yang, and H. Y. Zhang, *J. Chem. Phys.* 113, 2068 (2000).
159. G. S. Agarwal, *Phys. Rev. A* 4, 739 (1971).
160. A. O. Caldeira and A. J. Leggett, *Physica A* 121, 587 (1983).
161. Y. Tanimura and R. Kubo, *J. Phys. Soc. Jpn.* 58, 101 (1989).
162. Y. Tanimura and P. G. Wolynes, *Phys. Rev. A* 43, 4131 (1991).
163. Y. Tanimura and S. Mukamel, *J. Chem. Phys.* 101, 3049 (1994).
164. Y. J. Yan and S. Mukamel, *J. Chem. Phys.* 89, 5160 (1988).
165. Y. J. Yan, *Phys. Rev. A* 58, 2721 (1998).
166. G. Lindblad, *Commun. Math. Phys.* 48, 119 (1976).
167. G. Lindblad, *Rep. Math. Phys.* 10, 393 (1976).
168. V. Gorini, A. Kossakowski, and E. C. G. Sudarshan, *J. Math. Phys.* 17, 821 (1976).
169. R. Alicki and K. Lendi, "Quantum Dynamical Semigroups and Applications: Lecture Notes in Physics 286." Springer, New York, 1987.
170. R. Xu and Y. J. Yan, *J. Chem. Phys.* 116, 9196 (2002).
171. H. M. Sevian and J. L. Skinner, *J. Chem. Phys.* 91, 1775 (1989).
172. J. S. Bader and B. J. Berne, *J. Chem. Phys.* 100, 8359 (1994).
173. P. Pechukas, *Phys. Rev. Lett.* 73, 1060 (1994).
174. W. T. Strunz, L. Diósi, and N. Gisin, *Phys. Rev. Lett.* 82, 1801 (1999).
175. H. Dekker, *Phys. Rep.* 80, 1 (1981).
176. A. J. Leggett, S. Chakravarty, A. T. Dorsey, M. P. A. Fisher, A. Garg, and W. Zwerger, *Rev. Mod. Phys.* 59, 1 (1987).
177. S. Mukamel, "Principles of Nonlinear Optical Spectroscopy." Oxford, New York, 1995.
178. D. Kohen, C. C. Marston, and D. J. Tannor, *J. Chem. Phys.* 107, 5236 (1997).
179. H. Y. Zhang, Y. J. Yan, S. Yokojima, and G. H. Chen, unpublished.
180. S. Yokojima and G. H. Chen, *Chem. Phys. Lett.* 355, 400 (2002).
181. (a) S. Yokojima, G. H. Chen, R. Xu, and Y. J. Yan, *Chem. Phys. Lett.* 369, 495 (2003); *J. Comp. Chem.* 24, 2083 (2003).
182. G. D. Mahan, "Many-Particle Physics." Plenum, New York, 1990.
183. C. Meier and D. J. Tannor, *J. Chem. Phys.* 111, 3365 (1999).
184. J. J. P. Stewart, *J. Comput. Chem.* 10, 209; 221 (1989).
185. C. H. Choi, M. Kertesz, S. Dobrin, and J. Michl, *Theor. Chem. Acc.* 102, 196 (1999).
186. C. Lee, W. Yang, and R. G. Parr, *Phys. Rev. B* 37, 785 (1988); A. D. Becke, *Phys. Rev. A* 38, 3098 (1988); B. Miehlich, A. Savin, H. Stoll, and H. Preuss, *Chem. Phys. Lett.* 157, 200 (1989).
187. D. L. Phillips, M. Z. Zgierski, and A. B. Myers, *J. Phys. Chem.* 97, 1800 (1993).
188. J. H. Burroughes, D. D. C. Bradley, A. R. Brown, R. N. Marks, K. Mackay, R. H. Friend, P. L. Burns, and A. B. Holmes, *Nature* 347, 539 (1990).
189. G. Gustafsson, Y. Cao, G. M. Treacy, F. Klavetter, N. Colaneri, and A. J. Heeger, *Nature* 357, 477 (1992).
190. R. J. O. M. Hoofman, M. P. de Haas, L. D. A. Siebbeles, and J. M. Warman, *Nature* 392, 54 (1998).
191. U. Rauscher, H. Bässler, D. D. C. Bradley, and M. Hennecke, *Phys. Rev. B* 42, 9830 (1990).
192. S. Webster and D. N. Batchelder, *Polymer* 37, 4961 (1996).
193. M. Yan, L. J. Rothberg, E. W. Kwock, and T. M. Miller, *Phys. Rev. Lett.* 75, 1992 (1995).
194. I. D. W. Samuel, G. Rumbles, and C. J. Collison, *Phys. Rev. B* 52, 11573 (1995).
195. I. D. W. Samuel, G. Rumbles, C. J. Collison, R. H. Friend, S. C. Moratti, and A. B. Holmes, *Synth. Met.* 84, 497 (1997).
196. B. Mollay, U. Lemmer, R. Kersting, R. F. Mahrt, H. Kurz, H. F. Kauffman, H. Bassler, *Phys. Rev. B* 50, 10769 (1994).

197. S. Yokojima, D. H. Zhou, and G. H. Chen, *Chem. Phys. Lett.* 333, 397 (2001).
198. P. Gomes da Costa, R. G. Dandrea, and E. M. Conwell, *Phys. Rev. B* 47, 1800 (1993).
199. G. R. Hayes, I. D. W. Samuel, and R. T. Phillips, *Phys. Rev. B* 54, 8301 (1996).
200. A. S. Davydov, "Theory of Molecular Excitons." Plenum Press, New York, 1962.
201. R. Jakubiak, C. J. Collison, W. C. Wan, L. J. Rothberg, and B. R. Hsieh, *J. Phys. Chem. A* 103, 2394 (1999).
202. S. Siddiqui and F. C. Spano, *Chem. Phys. Lett.* 308, 99 (1999).
203. J. Cornil, D. A. dos Santos, X. Crispin, R. Silbey, and J. L. Bredas, *J. Am. Chem. Soc.* 120, 1289 (1998).
204. G. McDermott, S. M. Prince, A. A. Freer, A. M. Hawthornthwaitelawless, M. Z. Papiz, R. J. Cogdell, and N. W. Isaacs, *Nature* 374, 517 (1995).
205. J. Koepke, X. Hu, C. Muenke, K. Schulten, and H. Michel, *Structure* 4, 581 (1996).
206. X. Hu, T. Ritz, A. Damjanovic, and K. Schulten, *J. Phys. Chem. B* 101, 3854 (1997).
207. Th. Förster, *Naturwissenschaften* 33, 166 (1946).
208. S. Hess, K. J. Visscher, T. Pullerits, and V. Sundström, *Biochemistry* 33, 8300 (1994).
209. V. Sundström, T. Pullerits, and R. van Grondelle, *J. Chem. Phys. B* 103, 2327 (1999).
210. T. Meier, Y. Zhao, V. Chernyak, and S. Mukamel, *J. Chem. Phys.* 107, 3876 (1997).
211. Y. Zhao, T. Meier, W. M. Zhang, V. Chernyak, and S. Mukamel, *J. Phys. Chem. B* 103, 3954 (1999).
212. M. Dahlbom, W. Beenken, V. Sundström, and T. Pullerits, *Chem. Phys. Lett.* 364, 556 (2002).
213. T. Meier, V. Chernyak, and S. Mukamel, *J. Phys. Chem. B* 101, 7332 (1997); W. M. Zhang, T. Meier, V. Chenyak, and S. Mukamel, *J. Chem. Phys.* 108, 7763 (1998).
214. J. A. Leegwater, *J. Chem. Phys.* 100, 14403 (1996).
215. T. Pullerits, M. Chachisvilis, and V. Sundström, *J. Chem. Phys.* 100, 10787 (1996).
216. R. Monshouwer, M. Abrahamsson, F. van Mourik, and R. van Grondelle, *J. Phys. Chem. B* 101, 7241 (1997).
217. J. Ray and N. Makri, *J. Phys. Chem. A* 103, 9417 (1999).
218. M. Dahlbom, T. Pullerits, S. Mukamel, and V. Sundström, *J. Phys. Chem. B* 105, 9418 (1999).
219. D. Leupold, H. Stiel, K. Teuchner, F. Nowak, W. Sandner, B. Ucker, and H. Scheer, *Phys. Rev. Lett.* 77, 4675 (1996).
220. M. Chacisvilis, O. Kühn, T. Pullerits, and V. Sundström, J. *Phys. Chem. B* 101, 7275 (1997).
221. V. Novoderezhkin, R. Monshouwer, and R. van Goundelle, *Biophys. J.* 77, 666 (1999).
222. O. Kühn, V. Sundström, and T. Pullerits, *Chem. Phys.* 275, 15 (2002).
223. M. Gouterman, *J. Mol. Spectrosc.* 6, 138 (1961).
224. C. Weiss, *J. Mol. Spectrosc.* 44, 37 (1972).
225. S. Tretiak, V. Chernyak, and S. Mukamel, *J. Phys. Chem. B* 104, 4519 (2000).
226. S. Tretiak, C. Middleton, V. Chernyak, and S. Mukamel, *J. Phys. Chem. B* 104, 9540 (2000).
227. M. G. Cory, M. C. Zerner, X. Hu, and K. Schulten, *J. Phys. Chem. B* 102, 7640 (1998).
228. M. F. Ng, Y. Zhao, and G. H. Chen, *J. Phys. Chem. B* 107, 9589 (2003).
229. A. D. Bacon and M. C. Zerner, *Theor. Chim. Acta* 53, 21 (1979).
230. J. A. Pople and G. A. Segal, *J. Chem. Phys.* 43, S136 (1965).
231. J. A. Pople, D. L. Beveridge, and P. Dobosh, *J. Chem. Phys.* 47, 2026 (1967).
232. J. Ridley and M. C. Zerner, *Theor. Chim. Acta* 32, 111 (1973).
233. L. M. P. Beekman, R. N. Frese, G. J. S. Fowler, R. Picorel, R. J. Cogdell, I. H. M. van Stokkum, C. N. Hunter, and R. van Grondelle, *J. Chem. Phys. B* 101, 7293 (1997).
234. T. Polívka, D. Zigmantas, J. L. Herek, Z. He, T. Pascher, T. Pullerits, R. J. Cogdell, H. A. Frank, and V. Sundstrom, *J. Chem. Phys. B* 106, 11016 (2002).
235. Z. He, V. Sundström, and T. Pullerits, *Chem. Phys. Lett.* 334, 159 (2001).
236. M. Kasha, H. R. Rawls, and M. Ashraf El-Bayoumi, *Pure Appl. Chem.* 11, 371 (1965).
237. A. Damjanović, H. M. Vaswani, P. Fromme, and G. R. Fleming, *J. Phys. Chem. B* 106, 10251 (2002).
238. E. Poliakov, V. Chernyak, S. Tretiak, and S. Mukamel, *J. Chem. Phys.* 110, 8161 (1999); T. Minami, S. Tretiak, V. Chernyak, and S. Mukamel, *J. Lumin.* 87-9, 115 (2000).
239. J. Linnanto, J. E. I. Korppe-Tommola, and V. M. Helenius, *J. Phys. Chem. B* 103, 8739 (1999).
240. R. G. Alden, E. Johnson, V. Nagarajan, W. W. Parson, C. J. Law, and R. G. Cogdell, *J. Chem. Phys. B* 101, 4667 (1997).
241. T. Polívka, T. Pullerits, J. L. Herek, and V. Sundström, *J. Chem. Phys. B* 104, 1088 (2000).
242. J. P. Lewis, C. W. Carter, J. Hermans, W. Pan, T. S. Lee, and W. T. Yang, *J. Am. Chem. Soc.* 120, 5407 (1998).
243. D. M. York, T. S. Lee, and W. T. Yang, *Phys. Rev. Lett.* 80, 5011 (1998).
244. W. Z. Liang, S. Yokojima, M. F. Ng, G. H. Chen, and G. Z. He, *J. Am. Chem. Soc.* 123, 9830 (2001).
245. M. F. Ng and R. Q. Zhang, *Phys. Rev. B* 69, 115417 (2004).
246. J. P. Perdew, K. Burke, and Y. Wang, *Phys. Rev. B* 54, 16533 (1996).
247. A. D. Becke, *J. Chem. Phys.* 98, 5648 (1993).
248. M. Elstner, T. Frauenheim, and S. Suhai, *J. Mol. Struct-Theochem.* 632, 29 (2003).
249. A. Van der Vaart, V. Gogonea, S. L. Dixon, and K. M. Merz, *J. Comp. Chem.* 21, 1494 (2000); N. Diaz, D. Suarez, T. L. Sordo, and K. M. Merz, *J. Phys. Chem. B* 105, 11302 (2001).
250. J. M. Cabrera-Trujillo and J. Robles, *Phys. Rev. B* 64, 165408 (2001).
251. J. P. Lewis, S. B. Liu, T. S. Lee, and W. T. Yang, *J. Comp. Phys.* 151, 242 (1999).
252. J. Khandogin, K. Musier-Forsyth, and D. M. York, *J. Mol. Biol.* 330, 993 (2003).
253. S. D. Shellman, J. P. Lewis, K. R. Glaesemann, K. Sikorski, and G. A. Voth, *J. Comp. Phys.* 188, 1 (2003).
254. C. M. Goringe, E. Hernandez, M. J. Gillan, I. J. Bush, *Comput. Phys. Commun.* 102, 1 (1997).